Programa de Doctorado en Neurociencias

INGENIO -

Imaging Noninvasively Grey&white matter to Elucidate Neurodegenerative and Inflammatory disOrders

Antonio Cerdán Cerdá

Director/a de la tesis

Dra. Dña. Silvia De Santis

Codirector/a de la tesis

Dr. D. Santiago Canals Gamoneda

Universidad Miguel Hernández de Elche

- 2025 -

La presente Tesis Doctoral, titulada *"INGENIO - Imaging Noninvasively Grey&white matter to Elucidate Neurodegenerative and Inflammatory disOrders"*, se presenta bajo la modalidad de tesis convencional. A continuación, se incluye la referencia completa de la publicación que constituye el indicio de calidad de este trabajo:

Cerdán Cerdá, A., Toschi, N., Treaba, C. A., Barletta, V., Herranz, E., Mehndiratta, A., Gomez-Sanchez, J. A., Mainero, C., & De Santis, S. (2024). A translational MRI approach to validate acute axonal damage detection as an early event in multiple sclerosis. *eLife*, 13, e79169.

PMID: 38192199

DOI: 10.7554/eLife.79169

La Dra. Dña. Silvia De Santis, directora, y el Dr. D. Santiago Canals Gamoneda, codirector/a de la tesis doctoral titulada *"INGENIO - Imaging Noninvasively Grey&white matter to Elucidate Neurodegenerative and Inflammatory disOrders"*

INFORMAN:

Que D. Antonio Cerdán Cerdá ha realizado bajo nuestra supervisión el trabajo titulado *"INGENIO - Imaging Noninvasively Grey&white matter to Elucidate Neurodegenerative and Inflammatory disOrders"* conforme a los términos y condiciones definidos en su Plan de Investigación y de acuerdo al Código de Buenas Prácticas de la Universidad Miguel Hernández de Elche, cumpliendo los objetivos previstos de forma satisfactoria para su defensa pública como tesis doctoral.

Lo que firmamos para los efectos oportunos, en Sant Joan d'Alacant, a 13 de Junio de 2025

Directora de la tesis	Codirector/a de la tesis
Dra. Dña. Silvia De Santis	Dr. D. Santiago Canals Gamoneda

Dra. Dña. Maria Cruz Morenilla Palao, Coordinadora del Programa de Doctorado en Neurociencias en el Instituto de Neurociencias de Alicante, centro mixto de la Universidad Miguel Hernandez (UMH) y el Consejo Superior de Investigaciones Científicas (CSIC),

INFORMA:

Que D. Antonio Cerdán Cerdá ha realizado bajo la supervisión de nuestro Programa de Doctorado el trabajo titulado "*INGENIO - Imaging Noninvasively Grey&white matter to Elucidate Neurodegenerative and Inflammatory disOrders*" conforme a los términos y condiciones definidos en su Plan de Investigación y de acuerdo al Código de Buenas Prácticas de la Universidad Miguel Hernández de Elche, cumpliendo los objetivos previstos de forma satisfactoria para su defensa pública como tesis doctoral.

Lo que firmo para los efectos oportunos, en Sant Joan d'Alacant a 14 de Junio de 2025.

Dra. Dña. Maria Cruz Morenilla Palao

Coordinadora del Programa de Doctorado en Neurociencias

La tesis doctoral aquí presentada, "INGENIO - Imaging Noninvasively Grey&white matter to Elucidate Neurodegenerative and Inflammatory disOrders", es el resultado de la investigación desarrollada por D. Antonio Cerdán Cerdá en el Instituto de Neurociencias de Alicante, centro adscrito tanto a la Universidad Miguel Hernández (UMH) como al Consejo Superior de Investigaciones Científicas (CSIC). La realización de este proyecto ha sido factible gracias al contrato de investigación predoctoral del que he sido beneficiario ACIF/2020/301, concedido en el marco del programa de Subvenciones de la Generalitat Valenciana.

ACKNOWLEDGEMENTS

Esta tesis no ha sido un camino en solitario. Aunque el trabajo es personal, el recorrido ha estado profundamente marcado por la presencia, el ejemplo y el apoyo de quienes me han acompañado en estos años. Esta dedicatoria es un intento —necesariamente incompleto— de agradecer sin nombrar, de dejar constancia sin señalar, de rendir homenaje sin explicitar. Tal vez, quien lea, se reconozca en estas líneas; si es así, que sepa que su huella está presente, y que esta tesis también es, en parte, suya.

Todavía recuerdo nuestra primera reunión. He rebuscado el email que envié. Qué patético. Me diste las claves, aunque sin subrayarlas, como quien lanza pistas al futuro. Aprendizaje con efecto diferido, como si la claridad viniera siempre una escena después. Libertad y oportunidad; hacer y conocer.

He estado rodeado de quienes sabían más que yo, y no por eso se sintieron menos cercanos. Me acompañaron con firmeza, con generosidad, y con ese afecto discreto que aparece sin anunciarse, justo cuando hace falta. Gracias a ellos comprendí qué significa pertenecer, formar parte de algo que, aunque temporal, deja huella.

Todavía me pregunto si, el habernos conocido antes, la buena suerte no olvida. Aún me fascina tu forma de pensar: lo incansable. La curiosidad llega disfrazada de conversación casual, de una frase suelta que se me queda grabada sin saber por qué. No podría haber tomado una mejor decisión, y sé que es ese pensamiento el que ahora me produce vértigo.

He aprendido tanto de la paciencia de quien espera sin exigir, como de la pasión de quien no puede esconder su entusiasmo. Me enseñaron que no hay error más grande que el de no intentar, y que el conocimiento crece cuando se comparte, incluso en medio del cansancio, la duda o el desencanto.

Tú fuiste la que me inculcó la curiosidad por conocer lo que nos ocurre aquí dentro. Desde entonces, no he podido dejar de cuestionarme —todo. Sé que no era esa la intención

original, o quizás sí. Lo cierto es que ya no puedo mirar sin intentar comprender, ni escuchar sin buscar el trasfondo. Puede llegar a ser una condena.

Y después, cuando la lógica se agota y los datos no bastan, está el refugio. Ese lugar donde el juicio cede ante el consuelo, donde uno no necesita explicarse porque ya es comprendido— no siempre. La tesis es posible gracias a ese espacio, donde el afecto sostiene cuando el sentido parece desdibujarse.

Y es que las ciencias, importándonos tanto y siendo indispensables para nuestra vida y nuestro pensamiento, nos son, en cierto sentido, más extrañas que la filosofía. Cumplen un fin más objetivo, es decir, más fuera de nosotros. Son, en el fondo, cosa de economía. Un nuevo descubrimiento científico, de los que llamamos teóricos, es como un descubrimiento mecánico, el de la máquina de vapor, el teléfono, el fonógrafo, el aeroplano, una cosa que sirve para algo. Así, el teléfono puede servirnos para comunicarnos a distancia con la mujer amada. Pero ésta, ¿para qué nos sirve? Toma uno el tranvía eléctrico para ir a oír una ópera, y se pregunta: «¿Cuál es en este caso más útil, el tranvía o la ópera?».

— Miguel de Unamuno

Del sentimiento trágico de la vida

INDEX

ACRONYMS

A

Aβ - amyloid-beta

AD - Alzheimer's Disease

ADC - apparent diffusion coefficient

ANOVA - analysis of variance

ANTs - advanced normalization tools

AP - anterior-posterior

AX - axonal diameter

B

BET - brain extraction tool

BIC - bayesian information criterion

BSA - bovine serum albumin

C

CBV - cell body volume

CHARMED - composite hindered and restricted model of diffusion

CNS - central nervous system

CSD - constrained spherical deconvolution

CSF - cerebrospinal fluid

CSF1R - colony stimulating factor 1 receptor

D

DALYs - disability-adjusted life-years

DAPI - 4′,6-diamidino-2-phenylindole

DIPY - diffusion imaging in python

DKI - diffusion kurtosis imaging

DNA - deoxyribonucleic acid

DTI - diffusion tensor imaging

DV - dorso-ventral

dw-MRI - diffusion-weighted magnetic resonance imaging

E

EDSS - expanded disability status scale

EM - electron microscopy

F

FA - fractional anisotropy

FDR - false discovery rate

FID - free induction decay

FLAIR - fluid-attenuation inversion recovery

fMRI - functional magnetic resonance imaging

fODF - fiber orientation distribution function

FOV - field-of-view

FSL - FMRIB (University of Oxford's Functional MRI of the Brain) software library

G

GFAP - glial fibrillary acidic protein

GRAPPA - generalized autocalibrating partially parallel acquisitions

H

HARDI - high angular resolution diffusion imaging

HC - healthy control

I

Iba1 - ionazed calcium binding adaptor molecule 1

IBO - Ibotenic acid

IHC - immunohistochemistry

IL-1β - interleukin-1β

IL-6 - interleukin-6

L

lD - diffusion length

LM - latero-desial

LPS - lipopolysaccharide

LYS- L-α-lysolecithin

M

MBP - myelin basic protein

MCM - multi-compartment model

MD - mean diffusvity

MPRAGE - mutiecho magnetization-prepared rapid gradient-echo

MRI - magnetic resonance imaging

MRS - magnetic resonance spectroscopy

MS - Multiple Sclerosis

MTI - magnetization transfer imaging

Mxy - transverse magnetization vector

Mz - longitudinal magnetization vector

N

NAWM - normal-appearing white matter

NDI - neurite density index

NeuN - neuronal-specific nuclear protein

NEXI - neurite exchange imaging

NIFTI - neuroimaging informatics technology initiative

NMDA - N-methyl D-aspartate

NODDI - neurite orientation dispersion and density imaging

O

ODI - neurite orientation despersion

OPC - oligodendrocyte precursor cell

P

PBS - phosphate-buffered saline

PD - Parkinson's diseases

PDen - process density

PDis - process dispersion

PDt - proton density

PET - positron emission tomography

PFA - paraphormaldehyde

PGSE - pulsed gradient spin echo

PPMS - primary progressive multiple sclerosis

Q

QSM - quantitative susceptibility mapping

R

RARE - rapid acquisition with relaxation enhancement

RD - radial diffusiviy

RESTORE- robust estimation of tensors by outlier rejection

RF - radiofrequency

ROI - region of interest

ROS - reactive oxygen species

RRMS - relapsing-remitting multiple sclerosis

S

SANDI - soma and neurite density imaging

SD - standard deviation

SDMT - symbol digit modalities test

SM - standard model

sMRI - structural magnetic resonance imaging

SNR - signal-to-noise ratio

SPMS - secondary progressive multiple sclerosis

STEAM - stimulated echo acquisition mode

STEM - scanning transmission electron microscopy

T

T_1 - longitudinal relaxation

T_2 - transverse relaxation

TBSS - tract-based spatial statistics

TE - echo time

TFCE - threshold-free cluster enhancement

TNF-α - tumor necrosis factor-α

TR - repetition time

TSPO - translocator protein

V

vin - intracellular volume fraction

W

WM - white matter

WMTI - white matter tract integrity

Δ - diffusion time

δ - pulse width

LIST OF FIGURES AND TABLES

ABSTRACT

Magnetic resonance imaging (MRI), and especially diffusion-weighted approaches, display exquisite sensitivity to brain microstructural alterations, but are notoriously lacking specificity to cellular sub-compartments, hampering the applicability of such technique as a non-invasive biopsy. This study establishes and validates an experimental–analytical framework for developing diffusion MRI (dw-MRI) biomarkers of brain microstructure of inflammation in grey matter, and axonal degeneration in white matter. In rat experimental preparations, focal neuroinflammation, acute axonal injury and demyelination were induced under controlled conditions and temporally separated, thanks to different cellular reactivity windows and pharmacological manipulations. Advanced multiparametric dw-MRI sequences combined with histology-inspired multicompartment modeling produced distinct imaging fingerpints, validated by immunohistochemistry and electron microscopy. In grey matter, our dw-MRI approach sensitively and specifically differentiated inflammation with or without neurodegeneration and was robust against other potential confounds like demyelination. In white matter, we confirmed and validated dw-MRI's sensitivity to detect acute axonal damage. Translation to humans revealed a diffuse increase in axonal diameter in normal-appearing white matter of early multiple sclerosis patients, supporting its potential as an early clinical biomarker.

RESUMEN

La resonancia magnética (RM), y en particular los métodos ponderados en difusión, ofrecen una sensibilidad excepcional a los cambios microestructurales del cerebro, pero adolecen de una falta de especificidad hacia subcompartimentos celulares, lo que limita su aplicación como una "biopsia" no invasiva. Este estudio establece y valida un marco experimental–analítico para desarrollar biomarcadores de RM de difusión (RM-DI) que reflejen la microestructura cerebral: inflamación en la sustancia gris y degeneración axonal

en la sustancia blanca. Mediante preparaciones experimentales en rata, se indujeron bajo condiciones controladas y de manera temporalmente separada la neuroinflamación focal, el daño axonal agudo y la desmielinización, aprovechando ventanas de reactividad celular diferenciadas y manipulaciones farmacológicas. La combinación de secuencias multiparamétricas avanzadas de RM-DI con modelos multicompartmentales inspirados en histología generó firmas imagenológicas distintas, validadas mediante inmunohistoquímica y microscopía electrónica. En sustancia gris, nuestro enfoque de RM-DI diferenció de forma sensible y específica la inflamación con o sin neurodegeneración y resultó robusto frente a posibles confusores como la desmielinización. En sustancia blanca, confirmamos y validamos la capacidad de la RM-DI para detectar daño axonal agudo. La traducción del protocolo a humanos reveló un aumento difuso del diámetro axonal en la sustancia blanca de apariencia normal de pacientes con esclerosis múltiple en fases iniciales, lo que respalda su potencial como biomarcador clínico temprano.

I. INTRODUCTION

The Burden of Brain Diseases

Brain diseases, including a wide range of neurological and neurodegenerative disorders, are among the leading causes of disability and mortality worldwide. These conditions—ranging from stroke, epilepsy, and Alzheimer's disease (AD) to Parkinson's disease and multiple sclerosis (MS)—account for a substantial portion of the global disease burden, both in terms of years lived with disability and years of life lost.

According to global burden of disease studies, neurological disorders are the second leading cause of death and the leading cause of disability-adjusted life years (DALYs) globally (Feigin et al., 2020). Globally, over 3.4 billion individuals were estimated to have a condition affecting the nervous system in 2021, corresponding to 43.1% of the world population. Furthermore, these conditions contributed to 443 million DALYs and were the top-ranked contributors to global disease burden. For instance, AD alone accounted for 36.3 million DALYs in 2021, emphasizing its significant impact (Figure 1.1; adapted from Steinmetz et al., 2024). Advancements in healthcare and reduced mortality from other diseases have further amplified this trend, stressing the urgent need to better understand and manage brain pathological disability (Niccoli & Partridge, 2012).

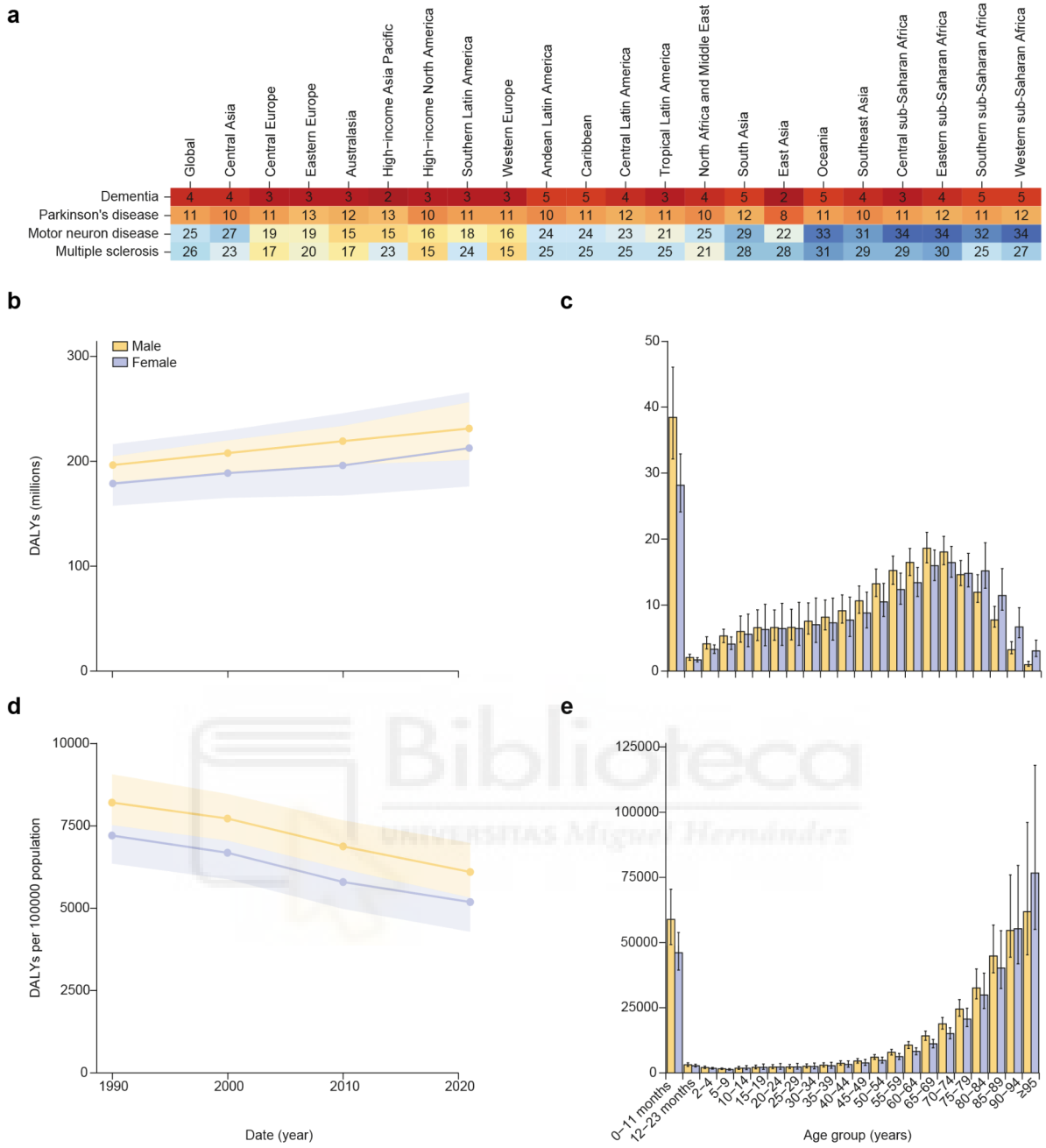

Figure 1.1. Global and Regional Patterns of Neurological Disorder Burden. a. Ranking of age-standardized DALY rates for dementia (including Alzheimer's disease and related dementias), Parkinson's disease, motor neuron disease, and multiple sclerosis with neurological health loss in 2021 across different regions. Temporal evolution of global DALY counts for all neurological conditions **b** and their distribution by age **c** in 2021. Age-standardized DALYs per 100,000 population over time **d** and the corresponding age-specific rates **e** for 2021. Shaded areas in Panels **a** and **d** and black bars in Panels **b**

and **e** represent 95% uncertainty intervals. DALYs denote disability-adjusted life years. Note: Rankings are based exclusively on disease DALYs attributed to neurological complications. Adapted from Steinmetz et al. (2024).

This growing societal burden places significant strain on healthcare systems worldwide, as a larger proportion of the population is developing brain disability conditions. Consequently, the development of biological markers - or biomarkers - to better characterize, monitor, and treat the underlying mechanisms of brain pathology have emerged as a priority. A biomarker is an objective indicator of a biological or pathological state capable of predicting disease progression or treatment response (Beard et al., 2016). However, traditional biomarkers often fail to elucidate the root cause of a condition. In contrast, process-specific biomarkers go further by identifying the exact biological processes or substances driving the disease, thereby enabling the development of targeted interventions.

Magnetic Resonance Imaging (MRI) has revolutionized neuroscience and neurology by enabling non-invasive assessments of the brain's structure and function (Strimbu & Tavel, 2010). MRI-based biomarkers play an increasingly vital role in diagnosing and understanding neurodegenerative diseases. However, challenges remain, including the lack of full interpretability in most of the biomarkers (De Santis et al., 2014; Agosta et al., 2017) and difficulties in translating advanced MRI techniques used in research into routine clinical applications. Developing bio-specific MRI biomarkers necessitates a translational approach that integrates findings from both human studies and animal models.

Animal models are indispensable for elucidating the underlying mechanisms of disease. MRI, being non-invasive, is particularly well-suited for these studies and allows for a high level of translatability and adaptation between animal and human research. In addition, by combining MRI with complementary data sources, such as genetic, biochemical, and cognitive information, we can construct a more comprehensive picture of neurodegenerative processes.

This thesis explores the potential of MRI-based process-specific biomarkers to enhance our understanding of two fundamental processes frequently implicated in brain diseases: neuroinflammation and neurodegeneration, particularly their manifestation in axonal damage. By applying advanced imaging techniques with a translational research perspective, this work aims to develop more precise and informative biomarkers, ultimately improving the characterization of these pathological manifestations and guiding the development of novel therapeutic strategies.

Neurobiological Processes and Challenges in Brain Health

This section delves into the critical neurobiological processes and challenges associated with brain health. It explores key concepts such as neuroinflammation, neurodegeneration, and demyelination, highlighting the complex interplay between these processes and their impact on various neurological disorders. Additionally, the processes involved in MS disease are considered, because of its relevance in this work.

Neuroinflammation

The term neuroinflammation describes the response of the brain's innate immune system, typically initiated in reaction to injury, infection, or chronic disease. This complex process involves various cellular players and molecular mediators that interact to protect the brain under acute conditions but can cause harm when inflammation becomes chronic. Microglia, the brain's resident immune cells, are among the first responders to brain pathology. These cells originate as primitive macrophages from the embryonic yolk sac, therefore they can acquire a macrophage-like profile. Upon activation, they release pro-inflammatory cytokines and phagocytose cellular debris, playing a dual role in initiating repair and exacerbating damage. Astrocytes, another key glial cell type, can undergo proliferation during neuroinflammation, secreting inflammatory mediators and contributing to the formation of a glial scar, which can limit repair and worsen neuronal dysfunction (Brites & Fernandes, 2015; Hennessy et al., 2015; Subhramanyam et al., 2019). Peripheral immune cells, particularly

macrophages and CD8-positive T lymphocytes, also play pivotal roles in neuroinflammation, especially in conditions involving blood-brain barrier disruption. Macrophages infiltrating the central nervous system amplify inflammatory signaling, complementing the activity of reactive microglia and engaging in debris clearance (Mammana et al., 2018). They contribute to both the amplification of inflammation and phagocytosis, bridging innate and adaptive immune responses (Galea et al., 2008). In contrast, CD8-positive T lymphocytes, which target infected or damaged neurons, often aggravate neuronal damage and intensify inflammation (Johnson et al., 2012). T cells attack compromised neuronal populations and perpetuate the inflammatory environment, a phenomenon particularly evident in multiple sclerosis (Tallantyre et al., 2009; Ifergan et al., 2011; Karussis, 2014).

At the molecular level, cytokines such as interleukin-1β (IL-1β), tumor necrosis factor-α (TNF-α), and interleukin-6 (IL-6) mediate the inflammatory cascade. While these molecules support immune defense and tissue repair in acute settings, their chronic overproduction disrupts neuronal homeostasis and accelerates disease progression (Ye et al., 2013). Persistent immune activation and cytokine dysregulation are key drivers of neurodegeneration (Matousek et al., 2012). Chronic neuroinflammation is closely linked to neurodegenerative diseases, aging-related cognitive decline, and multiple sclerosis (Kaur et al., 2019).

Aging, in particular, introduces a phenomenon termed "inflammaging," characterized by low-grade neuroinflammation that correlates with cognitive decline and increased susceptibility to neurodegenerative diseases (Franceschi et al., 2018). In Alzheimer’s and Parkinson’s diseases (PD), sustained activation of glial cells, macrophages, and T lymphocytes accelerates neuronal loss (W.-Y. Wang et al., 2015). Meanwhile, in multiple sclerosis, immune cell infiltration leads to demyelination and axonal injury, emphasizing the complex interplay between neuroinflammation and systemic immune dysregulation (Rossi et al., 2014).

Neurodegeneration

Neurodegeneration refers to the progressive loss of structure or function of neurons, ultimately leading to neuronal death. This process often involves synaptic dysfunction, mitochondrial impairment, oxidative stress, and the accumulation of misfolded or aggregated proteins. Cellular mechanisms such as impaired protein homeostasis, autophagy dysfunction, and chronic activation of apoptotic pathways contribute significantly to the neuronal damage seen in neurodegenerative disorders. Aggregates of misfolded proteins, including amyloid-beta (Aβ) plaques and tau neurofibrillary tangles in AD or alpha-synuclein inclusions (Lewy bodies) in PD, are hallmark features of neurodegeneration that interfere with cellular homeostasis and synaptic transmission (Selkoe & Hardy, 2016).

Mitochondrial dysfunction and increased oxidative stress are critical drivers of neurodegenerative mechanisms. In AD and PD, the accumulation of reactive oxygen species (ROS) exacerbates neuronal damage by causing lipid peroxidation, DNA damage, and protein oxidation, creating a vicious cycle that perpetuates neuronal loss (Lin & Beal, 2006). Disrupted calcium homeostasis and impaired energy metabolism further destabilize neuronal function, especially in highly energy-dependent regions such as the hippocampus and substantia nigra (Choi, 1988).

Axonal degeneration is a fundamental pathological process in numerous neurodegenerative disorders, typically preceding neuronal death and significantly contributing to the decline of neural connectivity and function. The foundational understanding of this phenomenon dates back to the pioneering work of August Waller, who, in the mid-19th century, systematically described the degeneration of nerve fibers following transection (Waller, 1850). His investigations led to the characterization of what is now referred to as Wallerian degeneration, an orchestrated sequence of pathological events observed following axonal injury. This process unfolds in three main phases: an initial latency phase during which the severed distal axon remains structurally intact for approximately 36 hours; a subsequent acute phase marked by cytoskeletal disruption and axonal fragmentation, often

accompanied by glial cell activation *in vivo*; and finally, a terminal phase involving axonal disintegration, degradation of the myelin sheath, and clearance of debris via infiltrating macrophages (Coleman, 2005; Court & Coleman, 2012).

Demyelination

Demyelination refers to the pathological loss or damage of myelin sheaths that insulate axons, disrupting the rapid transmission of electrical signals in the nervous system. This process is a hallmark of MS but is also observed in other conditions such as neuromyelitis optica and certain leukodystrophies. Demyelination impairs saltatory conduction along axons, leading to slower signal transmission, conduction block, and eventual axonal degeneration (Nave & Trapp, 2008). At the cellular level, one prevalent outside-in model proposes that demyelination is driven by immune-mediated damage, in which infiltrating T cells, B cells, and macrophages attack myelin and oligodendrocytes. However, an alternative inside-out hypothesis suggests that primary oligodendrocyte dysfunction precedes—and triggers—immune infiltration (Stys et al., 2012; ’t Hart et al., 2021). (Stys et al., 2012; ’t Hart et al., 2021). Chronic activation of microglia further contributes to the inflammatory environment, exacerbating myelin and axonal damage (Dong & Yong, 2019; Veroni et al., 2020). Oxidative stress and mitochondrial dysfunction play additional roles in the degeneration of both myelin and axons, particularly in progressive forms of MS (Mahad et al., 2009).

Imaging techniques like diffusion tensor imaging (DTI) and magnetization transfer imaging (MTI) have provided insights into the microstructural changes associated with demyelination, making it possible to study lesion burden and remyelination potential *in vivo* (Schmierer et al., 2004, 2007). Importantly, remyelination—the repair of damaged myelin—is mediated by oligodendrocyte precursor cells (OPCs), which proliferate and differentiate to replace lost myelin. However, this process is often incomplete in chronic conditions due to the inhibitory microenvironment and cellular senescence (Franklin & ffrench-Constant, 2008). In addition,

Human OPCs showed less proliferative and remyelinating activity compared to mouse OPCs (Bribián et al., 2020).

Irreversible demyelination is central to the pathophysiology of MS, where it correlates with disease progression and disability. Loss of myelin compromises axonal integrity, resulting in irreversible damage that contributes to neurodegeneration in later stages of the disease (Trapp & Nave, 2008). Understanding the mechanisms of demyelination is crucial for developing therapeutic strategies to promote remyelination and neuroprotection. For instance, treatments aimed at enhancing OPC recruitment and differentiation hold promise for repairing damaged myelin (Goldschmidt et al., 2009). Moreover, experimental studies have revealed potential targets for mitigating demyelination, such as modulating microglial activity to reduce inflammation or targeting mitochondrial pathways to preserve axonal function (Lassmann & van Horssen, 2011). These insights underscore the importance of addressing both the demyelination itself and its downstream effects to slow disease progression and improve outcomes.

Multiple Sclerosis

MS deserves special attention in this work since this thesis focuses on developing and probing new non-invasive MRI biomarkers that will help the understanding of this complex and devastating disease. Multiple sclerosis is a chronic neuroinflammatory disorder characterized by an aberrant immune response that targets myelin sheaths, leading to demyelination, axonal damage, and progressive neurodegeneration. The hallmark pathological features include inflammatory lesions, remyelination failure, and chronic neurodegeneration in both lesions and normal-appearing white matter (NAWM).

This neurodegeneration in NAWM, often overlooked in early disease stages, contributes to irreversible damage and long-term disability (Filippi et al., 2013). Axonal damage is the main pathological substrate of irreversible neurological disability. It can either be direct or secondary to demyelination, glial activation, or exposure to excitatory amino acids and

cytokines (Haines et al., 2011). Luchicchi et al. (2021) have provided insights into the subtle yet progressive nature of NAWM degeneration in MS, positing that axonal blistering represents an early pathological feature of this disease. Their work highlights how microstructural changes in ostensibly normal brain tissue, detectable via advanced microscopic imaging techniques, correlate with inflammatory and neurodegenerative processes. Chronic activation of microglia and infiltration of peripheral immune cells are central to the disease mechanism, driving both focal lesion formation and diffuse neurodegeneration. Demyelination disrupts axonal conduction, while oxidative stress and mitochondrial dysfunction exacerbate neuronal loss and synaptic failure (Lassmann, 2018).

MS manifests in a variety of clinical phenotypes, ranging from relapsing-remitting MS (RRMS) to secondary progressive MS (SPMS) and primary progressive MS (PPMS), each associated with varying degrees of disability. The transition to progressive MS occurs when an axonal loss threshold is reached, and the brain compensatory capacity is surpassed (Criste et al., 2014). This progressive accumulation of axonal damage leads to motor, sensory, and cognitive impairments, significantly reducing patients' quality of life (Compston & Coles, 2008). Cognitive decline, fatigue, and depression further exacerbate the disease burden, with substantial socioeconomic implications (Trapp & Nave, 2008).

MRI as a tool to characterize brain parenchyma

MRI plays a pivotal role in neuroscience research by offering a non-invasive means to investigate brain structure, function, and microarchitecture. Its versatility allows researchers to study diverse conditions, from neurodegenerative diseases like Alzheimer's and Parkinson's to inflammatory conditions such as MS. MRI's ability to provide both macroscopic views of brain anatomy and detailed microstructural insights has revolutionized diagnostics and monitoring. For instance, structural MRI (sMRI) reveals cortical thickness and brain atrophy patterns, while functional MRI (fMRI) captures neuronal activity and

connectivity. These modalities have become indispensable for understanding both healthy and diseased brains (Grover et al., 2015; Noor et al., 2020).

The fundamentals of Magnetic Resonance Imaging

The underlying mechanism of MRI involves the application of strong magnetic fields and radiofrequency (RF) pulses to probe the behavior of protons (^{1}H) prevalent in biological tissues, particularly within water and lipids. Protons possess an intrinsic quantum property termed spin, analogous to angular momentum, which imparts a magnetic moment, effectively rendering each proton a minute magnet (Figure 1.2a). When subjected to an external magnetic field, these protons experience torque, causing alignment or anti-alignment with the field, corresponding to distinct energy states. Due to their angular momentum, protons precess around the magnetic field axis at the Larmor frequency, determined by the gyromagnetic ratio and the magnetic field strength (Figure 1.2b).

In the presence of an external magnetic field, the aggregate behavior of proton spins generates a macroscopic magnetization vector, decomposable into longitudinal (Mz) and transverse (Mxy) components. At equilibrium, Mz aligns with the external field, while Mxy averages to zero due to random phase distribution among individual spins. To elicit a measurable signal, an RF pulse at the Larmor frequency is applied, perturbing the system by tipping the net magnetization away from alignment with the external field. This excitation induces coherence among spins, producing a non-zero Mxy component, detectable as the MR signal. Following the cessation of the RF pulse, the system undergoes relaxation processes to return to equilibrium. Longitudinal relaxation (T_1) describes the recovery of Mz, influenced by tissue-specific molecular interactions; tissues with higher water content typically exhibit prolonged T_1 values. Transverse relaxation (T_2) refers to the decay of Mxy, governed by spin-spin interactions and local environmental factors, with shorter T_2 times observed in tissues containing macromolecules or restricted water diffusion (Figure 1.2c).

Variations in T_1 and T_2 relaxation times among different tissues underpin the contrast observed in MRI, enabling the differentiation of structures such as white matter, gray matter, and cerebrospinal fluid. Spatial encoding of the MR signal is achieved through the application of magnetic field gradients along orthogonal axes, modulating the Larmor frequency as a function of spatial position. This technique permits selective excitation and localization of signals, facilitating the reconstruction of detailed anatomical images.

The detected MR signal, induced in a receiver coil tuned to the Larmor frequency, undergoes a series of processing steps, including analog-to-digital conversion, k-space sampling, Fourier transformation, and image reconstruction. These processes culminate in the generation of high-resolution images, providing critical insights into the biochemical and structural properties of neural tissues. For a more comprehensive understanding, refer to the works of Friedman (1989), Stern (2008), Jenkinson & Chappell (2018), and Wolbarst & Yanasak (2019).

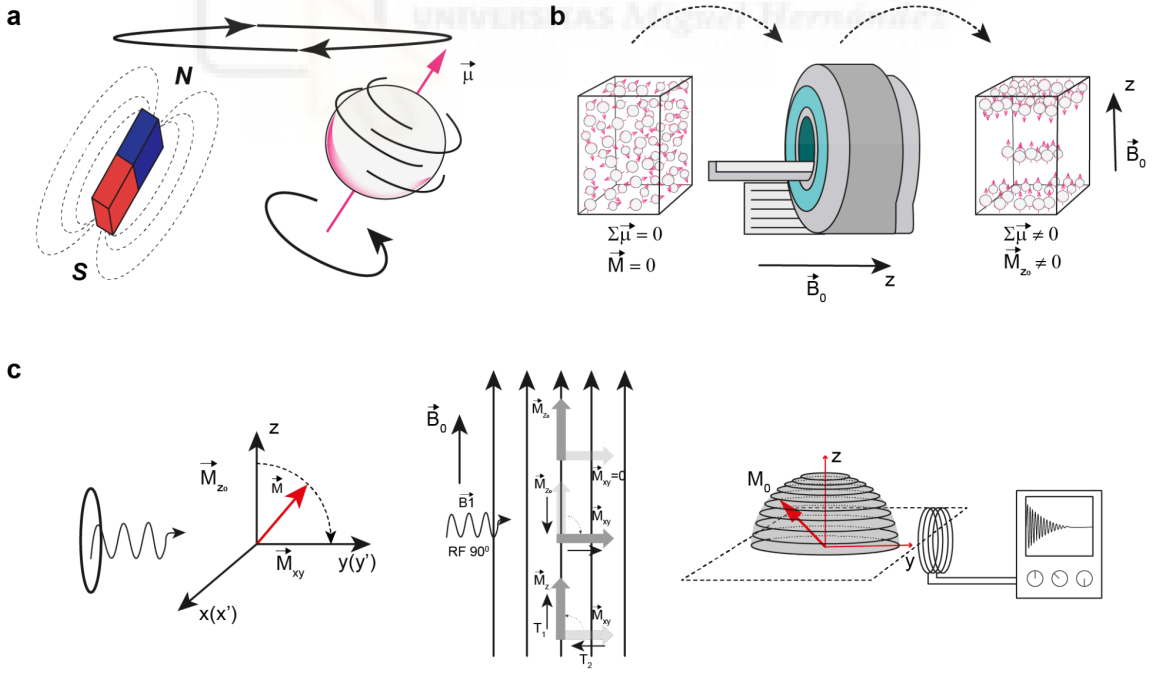

Figure 1.2. Principles of MR. a. Magnetic moment (μ) produced by a spinning charged particle. **b.** Schematic representation of how an applied magnetic field B_0 influences proton spin orientations. Initially (left), spins are randomly oriented, resulting in no net magnetization

(M=0). When B_0 is applied (center, right), a slight majority of spins align parallel (spin-up) rather than antiparallel (spin-down), producing a small net magnetization along B_0. Note that the protons themselves do not physically move to new locations; instead, their magnetic moments reorient, giving rise to the observed net magnetization. **c.** When placed in a strong external magnetic field (B_0), the net magnetization M_0 of the sample aligns along the z-axis (parallel to B_0). An applied radiofrequency (RF) pulse at the Larmor frequency excites the spin system, tilting M_0 away from the z-axis and into the transverse (xy) plane. Once in the transverse plane, the net magnetization precesses around B_0, inducing a detectable voltage in the nearby receiver coil (shown at right). This time-dependent signal, known as the MR signal or free induction decay (FID), is then recorded and processed to form the basis of MRI. Over time, the magnetization recovers along the z-axis (T_1 relaxation) and dephases in the transverse plane (T_2 relaxation), which affects the amplitude and duration of the detected signal.. Adapted from Kastler & Anstett (2011).

Relaxometry: Macroscale MRI techniques for brain tissue characterization

Structural MRI leverages the intrinsic relaxation properties of water molecules, particularly T_1 and T_2 relaxation times, to generate tissue contrast. Different tissues exhibit distinct T_1 and T_2 values, enabling differentiation between various anatomical structures. Sequences whose contrast mostly reflect T_1 and T_2 relaxation are termed T_1-weighted (T_{1w}) and T_2-weighted (T_{2w}) images, respectively (Figure 1.3).

In T_{1w} imaging, white matter appears with higher signal intensity compared to gray matter due to the shorter T_1 relaxation times of lipids within myelin. This contrast effectively delineates white matter anatomy and identifies structural lesions, such as multiple sclerosis plaques. Conversely, T_{2w} imaging renders white matter with lower signal intensity, as it exhibits shorter T_2 relaxation times compared to gray matter. This modality is particularly sensitive to changes in water content associated with edema, inflammation, and demyelination, or axonal loss (Stevenson et al., 2000; Knight et al., 2016).

Fluid-Attenuated Inversion Recovery (FLAIR) sequences suppress cerebrospinal fluid (CSF) signals, enhancing the contrast between lesions and adjacent tissues. FLAIR imaging is instrumental in detecting white matter hyperintensities indicative of pathologies such as vascular disease, inflammation, and demyelination (Bakshi et al., 2001).

Proton Density (PDt) imaging reflects the concentration of hydrogen protons, providing excellent anatomical detail. However, subtle white matter pathologies may be less conspicuous on PDt images compared to T_{2w} or FLAIR images (Just & Thelen, 1988).

Conventional MRI is essential for diagnosing and monitoring demyelinating disorders like MS. T_{2w} and FLAIR sequences visualize and characterize white matter lesions associated with MS and track changes in lesion burden over time (Traboulsee et al., 2005; Schiffmann & van der Knaap, 2009; Filippi et al., 2019).

Structural contrasts such as T_{1w} and T_{2w} imaging are well-suited for mapping brain anatomy and are widely used in clinical investigations to extract key information, including cortical thickness and the volume of different anatomical structures. Cortical thickness measures the width of the gray matter and can be calculated from T_{1w} magnetic resonance images (Tahedl, 2020). These measurements are crucial for assessing neurodegenerative disease and developmental abnormalities. Similarly, volumetric analyses of anatomical structures provide essential data for diagnosing and monitoring various neurological conditions.

Despite its utility, structural MRI lacks specificity in distinguishing the precise nature of white and gray matter pathologies, being only sensitive to mesoscopic structure.

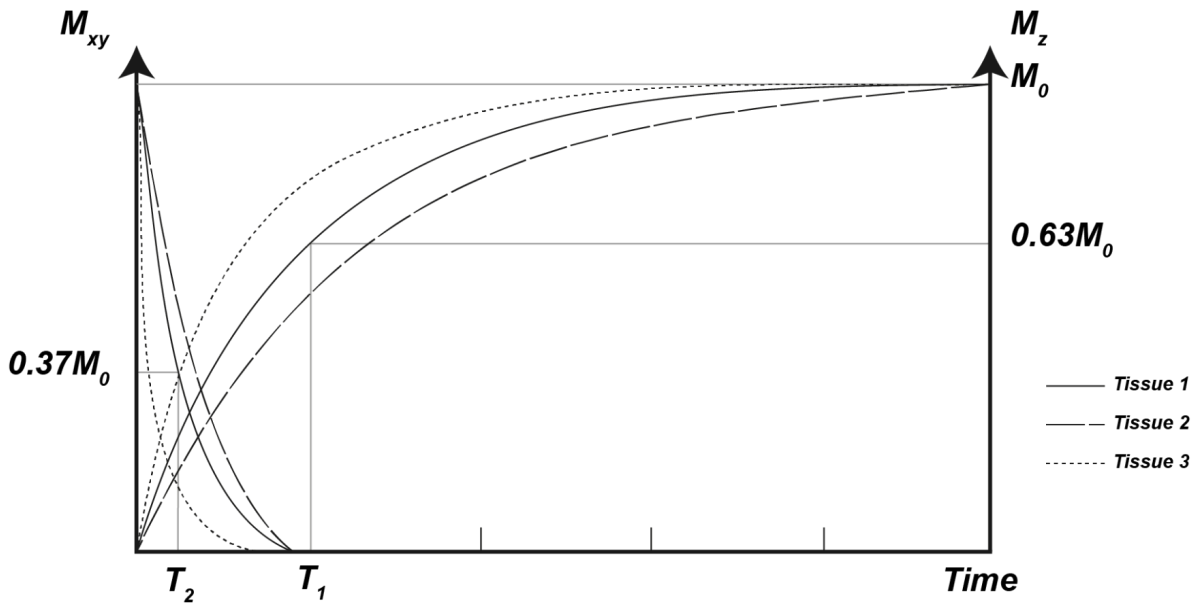

Figure 1.3. Relaxation Times. Depicted are the longitudinal (T_1) and transverse (T_2) relaxation times across a theoretical set of three tissues, each characterized by a unique proton composition that influences its relaxation properties. Fat, dominated by lipid protons, exhibits short T1 and short T2 values, leading to high signal intensity on T1-weighted and low signal on T2-weighted images. White matter also shows relatively short T1 and T2 values due to its myelin content, appearing bright on T1w and dark on T2w. In contrast, fluids such as cerebrospinal fluid (CSF) display long T1 and long T2 times, resulting in low intensity on T1w and very bright signal on T2w images. Grey matter lies in between, with intermediate T1 and T2 values. These differences in relaxation underlie the tissue contrasts in conventional structural MRI.

Diffusion-weighted MRI: A window into brain microstructure

Water molecules are in perpetual motion above absolute zero due to inherent thermal energy, a phenomenon termed Brownian motion. This random translational movement, first observed by botanist Robert Brown in 1827, mathematically characterized by Albert Einstein in 1905, is described as a “random walk” because the trajectories are entirely stochastic. In a two-dimensional unrestricted medium, the mean displacement of water molecules is zero, while the variance of displacement is expressed as:

$$\langle r^2 \rangle = 2nD\Delta \quad \textit{Eq. (1)}$$

Where $\langle r^2 \rangle$ denotes the main-squared displacement, *n* refers to the number of dimensions, *D* represents the diffusion coefficient, and Δ signifies the diffusion time (Figure 1.5a). In isotropic environments, this motion exhibits equal variance in all directions. However, within biological tissues, such as the brain, water molecule displacement is influenced by the architecture of structures like axons, cell bodies, and glial cells. In CSF-filled regions, such as the ventricular system, water diffusion approximates that in free media, resulting in isotropic diffusion direction, leading to low diffusion anisotropy. Conversely, in white matter, diffusion is facilitated along the longitudinal axis of neural fibers, rendering it an anisotropic structure.

Diffusion-weighted MRI (dw-MRI) is a pivotal technique for microscale characterization of brain tissue, capitalizing on the random motion of water molecules to infer microstructural properties. By probing the influence that biological structures cause on water molecules displacement, dw-MRI provides insights into the underlying microstructure of the brain (Jones, 2011; Emsell et al., 2016).

A foundational method for achieving diffusion sensitivity in MRI is the pulsed gradient spin echo (PGSE; Figure 1.4) sequence, introduced by Stejskal & Tanner (1965). This sequence employs two symmetric gradient pulses flanking a 180° refocusing radiofrequency (RF) pulse, enabling the measurement of molecular diffusion. The first gradient pulse induces a spatially dependent phase shift in the spins of hydrogen nuclei, while the second pulse, applied after the refocusing RF pulse, reverses this phase shift for static spins. However, spins undergoing diffusion during the interval between pulses experience incomplete rephasing, resulting in signal attenuation proportional to their displacement (Bihan et al., 1986). The degree of attenuation reflects the mobility of water molecules, quantified by the diffusion coefficient (D), and is modeled by the relationship (Figure 1.5):

$$S = S_0 e^{(-bD)} \quad \textit{Eq. (2)}$$

Here, S denotes the measured signal with diffusion weighting, S_0 is the signal without diffusion gradients, and the b-value encapsulates the magnitude of diffusion weighting. The b-value is crucially determined by the sequence parameters in the equation:

$$b = \gamma^2 G^2 \delta^2 (\Delta - \frac{\delta}{3}) \quad \textit{Eq. (3)}$$

where γ is the gyromagnetic ratio (42.58 MHz/T for protons), G is the gradient strength (mT/m), δ is the gradient pulse duration (ms), and Δ is the diffusion time (ms) between the leading edges of the two gradients. It should be noted that Eq. (3) strictly applies to rectangular diffusion gradients. For trapezoidal gradients, as those typically used in practice (see Figure 1.4), additional terms such as ramp time must be included in the calculation of the b-value.

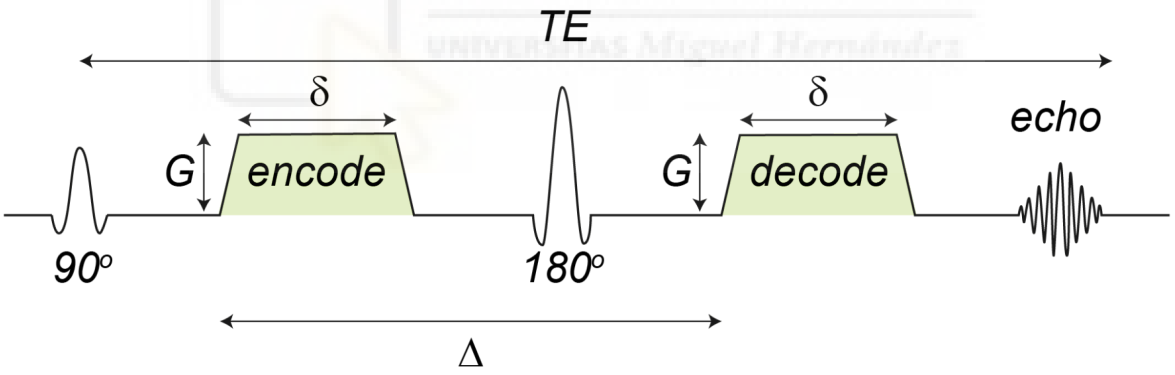

Figure 1.4. Pulsed Gradient Spin Echo (PGSE) Sequence. This illustration shows the PGSE sequence, which includes an excitation pulse (90°), a refocusing pulse (180°), and two gradient pulses (displayed as green trapezoids). In this diagram, G signifies the gradient strength, δ stands for the gradient duration, Δ represents the diffusion time (the interval from the onset of the first gradient pulse to the start of the second), and TE denotes the echo time (Source: Eed et al., 2020).

Modulating these parameters allows precise control over the b-value, thereby tuning the sensitivity of the MRI signal to specific regimes of water diffusion.

Although an imaging voxel in typical dw-MRI acquisitions is in the order of millimeters, the technique is sensitive to cellular-scale structures (micrometers) because the diffusion process is characterized by a much shorter displacement length within the available observation time. For instance, increasing gradient strength (G) or pulse duration (δ) amplifies the b-value quadratically, enhancing sensitivity to restricted diffusion in microstructurally dense tissues (e.g., tumors). Conversely, extending the diffusion time (Δ) permits detection of slower diffusion processes over larger spatial scales, such as intracellular motion (Le Bihan, 2003). By strategically adjusting G, δ, and Δ, the b-value can be optimized to highlight microstructural variations—such as differences in cell density, membrane integrity, or axonal fiber orientation—that are imperceptible in conventional MRI (Jones et al., 2018).

Water molecules at body temperature typically exhibit a diffusion coefficient of about 0.7 - 3 μm²/ms. In dw-MRI experiments, diffusion-sensitizing gradients are applied for Δ ranging from tens to a few hundred milliseconds. Over such diffusion times (e.g., 50–100 ms), the root-mean-square displacement of water molecules is on the order of 5–20 μm—closely matching the dimensions of cells and cellular processes. Therefore, even though the voxel itself averages over a large tissue volume, the measured signal carries statistical information about the hindrance and restrictions imposed by microstructural features such as cell membranes, axonal boundaries, and dendritic structures (Figure 1.5).

The physical basis for this sensitivity can be understood through the concept of “diffusion time” and the “diffusion length” (lD), where:

$$lD = \sqrt{2Dt} \quad \text{Eq. (4)}$$

with *D* being the diffusion coefficient and *t* the effective diffusion time. Hence, for *D* ~ 1 μm²/ms and t ~ 100 ms, lD is on the order of 14 μm. This means that during the measurement time, water molecules sample structural barriers at the micrometer scale, allowing dw-MRI to be sensitive to microscopic changes (Lee et al., 2020; Kiselev, 2021). Moreover, the diffusion-weighted signal depends nonlinearly on the b-value. At high b-values, the signal decay deviates from a simple mono-exponential form because the restriction effects from microstructural boundaries (e.g., cell membranes) become pronounced (Figure 1.5). The time-dependent behavior of the apparent diffusivity, often following a power-law (with an exponent close to ½), has been attributed to the distribution of restrictions along neuronal processes (Lee et al., 2020). Such behavior confirms that even with voxel sizes much larger than individual cells, the diffusion signal is indirectly sensitive to cellular geometry and density. This interplay between the temporal diffusion scale and the structural size of cells and their processes enables dw-MRI to provide valuable insights into brain microstructure.

However, in order to optimize a dw-MRI experiment it requires balancing competing demands. Higher b-values improve diffusion weighting and specificity to tissue microstructure but inherently reduce the signal-to-noise ratio (SNR) due to exponential signal decay (Le Bihan et al., 2001, 2006). Conversely, lower b-values preserve SNR but introduce confounding T_{2w} signal contributions, obscuring true diffusion effects (Schaefer et al., 2000). Thus, selecting an appropriate b-value is crucial. Advances in multi-b-value acquisitions and parametric modeling (e.g., diffusion kurtosis imaging) further refine microstructural insights, underscoring the importance of b-value optimization in modern diffusion MRI (Jones, 2011; Jones et al., 2018).

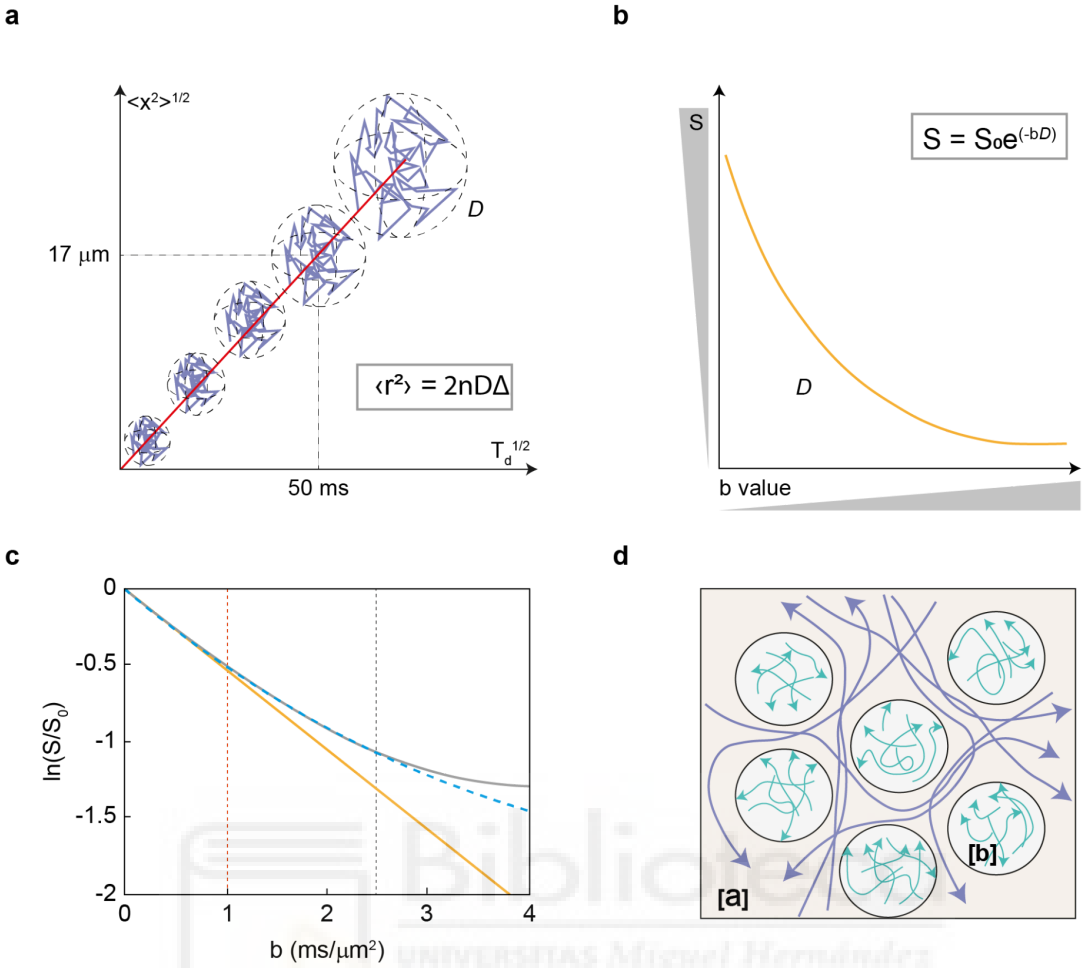

Figure 1.5. Fundamental Concepts of Diffusion and Diffusion-Weighted MRI. a. The random displacements of molecules resulting from thermal agitation (Brownian motion) obey a statistical law established by Einstein in 1905. Along *n* dimensions in space, $< x^2 >= 2nDT_d$, where T_d is the time for molecules to diffuse (Δ), *D* is the diffusion coefficient, and $< x^2 >$ is the variance of the molecular displacement along that dimension. With a very large number of molecules, the size of the 'cloud' representing average molecular excursion (root-meansquare of $< x^2 >$) increases linearly with the square root of T_d. For water at brain temperature, 68% of molecules have moved within a sphere of 17 μm diameter in 50 ms. **b.** Different degrees of diffusion-weighted images can be obtained using different values for the b value. The larger the b value, the more the signal intensity (*S*) becomes attenuated in the image. This attenuation is modulated by the diffusion coefficient

(*D)*. The signal in structures with fast diffusion (for example, water-filled ventricular cavities) decays rapidly with increasing *b*, whereas the signal in tissues with low diffusion (for example, gray and white matter) decreases more slowly. By fitting the signal decay as a function of *b*, one obtains the apparent diffusion coefficient (*D*) for each elementary volume (voxel) of the image. Calculated diffusion images (*D* maps) that depend solely on the diffusion coefficient can then be generated and displayed using a gray (or color) scale. **c.** In brain tissue, the diffusion-weighted MRI signal (dashed blue line) can be approximated as Gaussian (orange solid line, DTI) only up to a low b-value (~1 $ms/\mu m^2$ or 1000 s/mm^2, orange dashed vertical line), after which it deviates from a linear pattern and can be described by a quadratic function (gray solid line, DKI) up to moderate b-value (~2.5 $ms/\mu m^2$ or 2500 s/mm^2, gray dashed vertical line). **d.** In biological tissues, obstacles modulate the free diffusion process. Diffusion of molecules can be hindered by obstacles that result in tortuous pathways **[a]**. Diffusion might also be restricted in closed spaces **[b]**, such as cells. Figures adapted from Le Bihan (2003) and Jelescu & Fieremans (2023).

Conventional dw-MRI models

Diffusion Tensor Imaging (DTI), the most used dw-MRI technique, models water diffusion within each voxel using a diffusion tensor—a 3x3 matrix that encapsulates diffusion characteristics in three dimensions (Basser et al., 1994). During a typical diffusion experiment, multiple diffusion-weighted images are acquired along various non-collinear, non-coplanar directions, accompanied by one or more non-diffusion-weighted images serving as references. Due to tensor symmetry, a minimum of six of those independent measurements along distinct orientations, plus one non-diffusion-weighted measurement, are necessary to compute the diffusion tensor, though additional measurement can enhance the signal-to-noise ratio (Jones & Basser, 2004). Eigen-decomposition of the tensor yields several scalar indices, notably mean diffusivity (MD) and fractional anisotropy (FA).

MD represents the average diffusivity, expressed in square meters per second (m^2/s), within a voxel and is calculated as:

$$MD = \frac{(\lambda_1+\lambda_2+\lambda_3)}{3} \quad \textit{Eq. (5)}$$

where λ_1, λ_2, and λ_3 are the eigenvalues corresponding to the principal diffusion directions. FA quantifies the degree of diffusion anisotropy, with values ranging from 0 (isotropic diffusion) to 1 (anisotropic diffusion), and is defined as:

$$FA = \sqrt{\frac{(\lambda_1-\lambda_2)^2+(\lambda_2-\lambda_3)^2+(\lambda_3-\lambda_1)^2}{2(\lambda_1^2+\lambda_2^2+\lambda_3^2)}} \quad \textit{Eq. (6)}$$

where MD is the mean of the eigenvalues. These indices are orientationally invariant, making them effective quantitative biomarkers for assessing brain microstructure and diagnosing various pathologies. For instance, reduced FA is often interpreted as indicative of compromised white matter integrity (Beaulieu, 2002; Jones et al., 2013).

Additional metrics include axial diffusivity (ADt), defined as the principal eigenvalue (λ_1), representing diffusion along the primary axis, and radial diffusivity (RD), the average of the second and third eigenvalues, reflecting diffusion perpendicular to the primary axis:

$$ADt = \lambda_1 \quad \textit{Eq. (7)}$$

$$RD = \frac{(\lambda_2+\lambda_3)}{2} \quad \textit{Eq. (8)}$$

These metrics, alongside MD and FA, are extensively utilized in medical imaging to quantify brain microstructure, offering valuable insights for diagnosing a range of neurological conditions (Budde et al., 2009; Winklewski et al., 2018; Weston et al., 2020; Baijot et al., 2022; Zanon Zotin et al., 2023; Spotorno, Strandberg, Stomrud, et al., 2023; Spotorno, Strandberg, Vis, et al., 2023).

Complementary techniques, such as tractography, are derived from dw-MRI data manipulation. Tractography is a non-invasive image technique that reconstructs the brain's white matter pathways by analyzing the principal diffusion directions of water molecules. In white matter, water diffusion is anisotropic, favoring movement along the direction of axonal fibers. This characteristic enables the inference of fiber orientations by identifying the direction(s) of maximum diffusivity. By integrating these orientations of major axonal bundles, facilitating virtual dissection of neural pathways. However, in voxels where multiple fiber populations coexist (e.g., two fiber bundles crossing at 90°), the apparent diffusion coefficient (ADC) may peak at an intermediate orientation (e.g., 45°), which can confound the estimation of true fiber directions (Basser et al., 2000; Johansen-Berg & Behrens, 2009).

Tractography algorithms are primarily categorized into deterministic and probabilistic methods. Deterministic tractography follows a single, most likely pathway from each seed point, producing a specific trajectory based on the principal diffusion direction. In contrast, probabilistic tractography accounts for uncertainty in fiber orientations by generating multiple potential pathways from each seed point, resulting in a distribution of possible trajectories that reflect the probability of connection through a given voxel. This probabilistic approach is particularly advantageous in regions with complex fiber configurations, such as crossing fibers, where deterministic methods may be less accurate (Tsolaki et al., 2024).

While DTI provides valuable insights into white matter architecture, it has limitations in resolving complex fiber orientations within a single voxel. To address this, advanced techniques like High Angular Resolution Diffusion Imaging (HARDI) have been developed. HARDI acquires diffusion data along numerous directions, enabling more precise modeling of intricate fiber structures. Methods such as constrained spherical deconvolution (CSD) further enhance this capability by estimating the fiber orientation distribution function (fODF), allowing for the resolution of multiple fiber populations within a voxel (Dell'Acqua & Tournier, 2019).

Beyond research applications, tractography holds significant clinical potential, particularly in neurosurgical planning. By delineating critical white matter tracts, tractography assists surgeons in avoiding vital pathways during procedures such as tumor resection or deep brain stimulation, thereby reducing the risk of postoperative neurological deficits. Identifying the spatial relationship between lesions and white matter tracts informs surgical decision-making and enhances patients' outcomes (Kamagata et al., 2024).

Biophysical dw-MRI modelling

In the DTI framework, each voxel represents a single tensor characterized by a Gaussian diffusion profile. Given the disparity between the microscopic scale of neuronal cells and their axons (measured in micrometers) and the macroscopic dimensions of typical MRI voxels (measured in millimeters), numerous factors influence the resulting fractional anisotropy (FA) value. These factors include myelin content, axonal density, axonal diameter, and fiber orientation. A single diffusion tensor essentially reflects the averaged signal from tens of thousands of cells and/or axons, making it challenging to correlate a specific tissue configuration or biological state with observed FA changes. Due to this limitation, DTI lacks the ability to differentiate between distinct cellular and subcellular processes, such as structural degradation, inflammation, or neural remodeling. Consequently, it provides a restricted and inherently ambiguous representation of the underlying tissue compartments and neuroanatomy (De Santis et al., 2014).

As a consequence, more advanced dw-MRI acquisition techniques and reconstruction methods have been developed to overcome the limitations of DTI. "Biophysical modeling" offers tools to translate the complexities of water diffusion into detailed insights about brain tissue properties (figure 1.6) and their potential alterations caused by disease or development. Biophysical models of dw-MRI aim to bridge the gap between the diffusion signal and underlying tissue properties, and can be broadly categorized based on the target cell compartments of which they yield microstructural information. While numerous

formulations are nowadays available, a non-exhaustive list of the most representative ones is reported below:

- **The Ball-and-Stick Model:** The Ball-and-Stick model is a multi-compartmental framework designed to interpret dwMRI signals, particularly in complex neural architectures such as white matter. The "stick" represents highly anisotropic diffusion aligned with intracellular axons, while the "ball" represents isotropic diffusion typically found in extracellular spaces. This model effectively resolves crossing fibers, a significant limitation of simpler models like DTI, by accounting for multiple fiber orientations within a single voxel (Behrens et al., 2003).
- **The Composite Hindered and Restricted Model of Diffusion (CHARMED):** CHARMED partitions the diffusion signal into two compartments: restricted diffusion within the intracellular space and hindered diffusion within the extracellular space. This enables the mapping of detailed axonal properties, such as density and structure (Assaf & Basser, 2005).
- **Neurite Orientation Dispersion and Density Imaging (NODDI):** Building on CHARMED, NODDI introduces a third compartment for CSF, improving its ability to separate isotropic diffusion from tissue components. It provides advanced metrics such as the neurite orientation dispersion index (ODI) and intracellular volume fraction (vin), offering deeper insights into microstructural complexity (Zhang et al., 2012).
- **Soma and Neurite Density Imaging (SANDI):** SANDI model provides a significant leap by explicitly incorporating soma compartments alongside neurites. Unlike prior models that merge soma signal with extracellular compartments, SANDI distinguishes soma and neurite contributions. It uses advanced dw-MRI techniques at high diffusion-weighting (b-values), mapping apparent soma size and density. This separation enables improved characterization of brain cytoarchitecture, revealing

distinct soma and neurite contributions, as validated by simulations and experimental studies (Palombo et al., 2020).

- **AxCaliber:** The AxCaliber model, a natural extension of CHARMED, is a powerful framework for estimating axon diameter distributions within a voxel using dw-MRI. This approach models white matter as a bi-compartmental system, differentiating between restricted diffusion in intra-axonal spaces and hindered diffusion in extra-axonal spaces. By leveraging high-angular resolution and advanced acquisition protocols, AxCaliber provides critical insights into axonal health, enabling the detection of remodeling after injury or in pathological conditions (Assaf et al., 2008).
- **ActiveAx:** This is a sophisticated model for dw-MRI that characterizes white matter by incorporating realistic representations of axon properties, such as varying orientations, diameters, and myelin content. This approach provides critical insights into white matter structure and pathology by estimating metrics like mean axon diameter and axonal density. The model achieves this through high-angular resolution imaging and advanced multi-compartment analysis, which improves specificity compared to traditional diffusion models (Alexander et al., 2010).
- **White Matter Tract Integrity (WMTI):** This model, proposed by Fieremans et al. (2011), is a dw-MRI framework designed to analyze the microstructural organization of white matter. By modeling water diffusion within and around axons, WMTI quantifies compartment-specific diffusivities, including axon diameter distribution, intra-axonal diffusivity, and extra-axonal radial and axial diffusivities. This detailed characterization is instrumental in understanding white matter changes associated with development, neurodegeneration, and injury.
- **Standard Model (SM):** The SM represents brain tissue as a complex ensemble of microstructural components, including cells, axons, and dendrites. By accurately modeling water diffusion across these intricate environments, SM provides a detailed understanding of diffusion dynamics in both white and gray matter. This approach is particularly valuable for investigating complex neurological conditions and improving

diagnostic precision, especially in cortical gray matter, where traditional models often fall short (Novikov et al., 2019).

Biophysical models extract valuable insights from dw-MRI data, enabling fiber orientation mapping and quantification of critical parameters such as axonal density, diameter, and indirect markers of myelination. These parameters serve as sensitive biomarkers for various neurological and psychiatric conditions and allow for the detection of subtle tissue changes, facilitating investigations into disease progression and treatment effects. Despite their promise, biophysical models face significant challenges. Model validation remains an ongoing difficulty, as direct comparisons with actual tissue are limited. Additionally, many models are computationally demanding, hindering their clinical translation and application in large-scale studies. Advanced models often require specialized MRI sequences, increasing scan times and complexity, which restricts their use to research settings. For an elegant yet comprehensive overview of microstructural modeling of brain tissue using dw-MRI, refer to the work of Alexander et al. (2019).

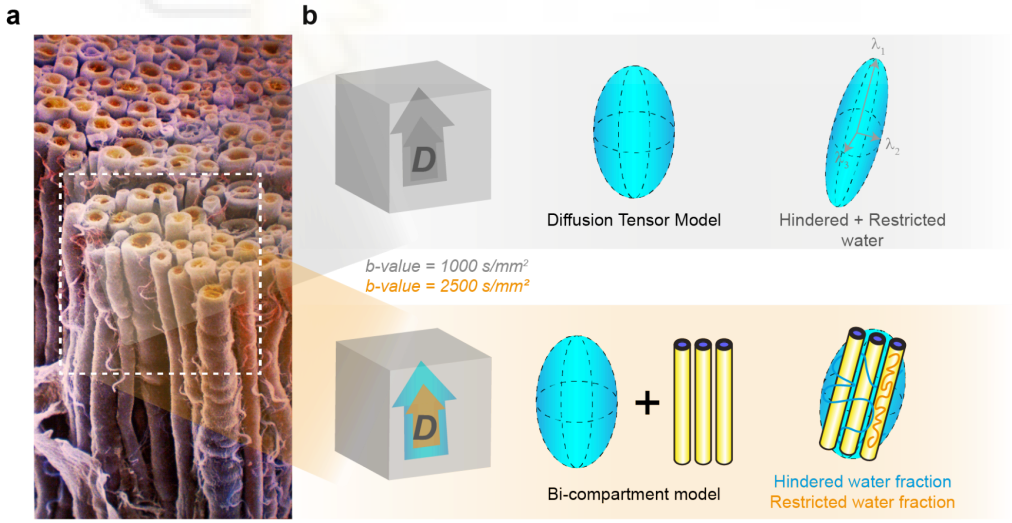

Figure 1.6. Advanced dw-MRI for enhanced underlying tissue characterization. This figure illustrates how variations in the dw-MRI acquisition protocol and biophysical modeling influence the estimation white matter microstructure. **a.** The biological ground-truth white matter tract that serves as the basis for the model. **b.** Each panel depicts a voxel

(represented as a cube) extracted from the tract in **a**. An upward arrow in each cube indicates the dominant water diffusion direction. In the top subpanel, diffusion is modeled using a tensor derived from a DTI acquisition with a b-value of 1000 s/mm², which is the sum of the signals arising from the restricted and hindered water molecules. In the bottom subpanel, the additional diffusion information acquired at a higher b-value (b = 2500 s/mm²) is represented by a small orange arrow. Here, a two-compartment biophysical model is employed to distinguish between hindered diffusion (illustrated by the tensor and blue line) and restricted diffusion (illustrated by multiple cylinders and the orange line), thereby providing a more comprehensive characterization of white matter microstructure.

Linking MRI Markers to Cellular-Level Processes

The validity of MRI as a non-invasive tool for exploring the brain microstructure relies on its ability to accurately reflect underlying biological processes. This ability to connect macro-, mesoscopic imaging findings to microscopic biological mechanisms not only validates MRI as a diagnostic tool but also enables precise monitoring of disease progression and therapeutic efficacy. This fidelity is achieved through rigorous validation of imaging markers using complementary techniques, such as histology, immunohistochemistry, and molecular assays. These methods bridge the gap between imaging findings and tissue-level changes, ensuring that observed markers truly represent the physiological and pseudo-, pathological phenomena they aim to characterize, providing a direct link between imaging parameters and underlying tissue pathology (Dyrby et al., 2018; Morawski et al., 2018; Jonkman et al., 2019; Lazari & Lipp, 2020).

In neuroinflammation, MRS provides insight with elevated myo-inositol levels serving as a reliable marker of astrocyte activity, confirmed through immunohistochemical validation (Chang et al., 2013; Ligneul et al., 2019). Diffusion-weighted imaging metrics such as increased orientation dispersion index, extra-axonal restricted diffusion, and MD have been shown to correlate with astrocytic proliferation and microglial reactivity, as verified by glial

fibrillary acidic protein (GFAP) and ionized calcium-binding adapter molecule 1 (Iba-1) staining in preclinical models (Taquet et al., 2019; Yi et al., 2019). Work by Yi et al. (2019) has linked changes in multicomparment dw-MRI metrics–specifically, an increase in the Orientation Dispersion Index–with microglia repopulation in *ex vivo* studies. Conversely, Noristani et al. (2017) did not identify correlations between *ex vivo* dw-MRI longitudinal ADC metric and microglia/monocytes density/morphology in a mice model of spinal cord injury.

In neurodegeneration, QSM has been validated as a sensitive marker for iron deposition, with direct histological correlations demonstrating its relevance in diseases like Parkinson's and Alzheimer's or normal aging (Poynton et al., 2014; Ravanfar et al., 2021). Similarly, decreased FA and increased MD observed in dw-MRI have been associated with neuronal loss and synaptic dysfunction, aligning with histological evidence of cortical thinning and axonal degeneration (Liu et al., 2017; Preziosa et al., 2019). Regarding axonal size estimation, previous studies reported correlations between the axonal diameter measured with MRI and axonal caliber estimated using electron microscopy in healthy tissue (Barazany et al., 2009), but with a reduced sample size. Additionally, in the context of MS AxCaliber has revealed a higher axonal diameter proxy in the NAWM of the corpus callosum of MS patients compared to healthy controls, which was interpreted as a sign of axonal damage (Huang et al., 2016). However, from a pathophysiological point of view, measuring a higher estimated MRI axonal diameter proxy in MS does not, per se, represent conclusive evidence of axonal damage, especially in the light of the known bias toward larger axons of MRI-based axonal diameter quantification (Horowitz, Barazany, Tavor, Bernstein, et al., 2015; Horowitz, Barazany, Tavor, Yovel, et al., 2015).

In demyelination, DTI metrics such as FA and RD have been extensively validated against histological measures of myelin integrity. Yano et al. (2017) used a cuprizone mouse model to explore the relationship between DTI metrics (FA, MD, RD) and myelin content. It found that FA decreases and RD increases during demyelination and recovers during remyelination, validated through histological analyses. RD was identified as a particularly

sensitive marker of myelin integrity. Similarly, Atkinson et al. (2019) demonstrated that FA and RD changes in a cuprizone model of demyelination align with histological evidence of myelin loss and remyelination. Specifically, RD was decreased and FA increased after estrogen receptor β ligand-induced remyelination, confirming the potential of these DTI metrics for monitoring therapeutic remyelination. Finally, in multiple sclerosis, the integration of imaging biomarkers has shed light on both focal and diffuse neurodegenerative processes. T_1 hypointense lesions observed in MRI strongly correlate with histopathological findings of axonal loss and severe tissue destruction in multiple sclerosis. Importantly, these findings extend to diffuse abnormalities in NAWM, providing histological validation for MRI markers as tools to assess neurodegeneration beyond focal lesions (Walderveen et al., 1998). Additionally, histological validation of advanced imaging techniques like NODDI has provided new perspectives on the microstructural changes occurring in NAWM, offering a more nuanced understanding of disease progression (Preziosa et al., 2019).

Although informative, none of the above works unravel the cell-specific events undergoing on inflammation, neurodegeneration and demyelination brain challenges, neither disentangle the complex and mutually dependent relationship between them. In addition, most of the works employ an extremely low sample size. Finally, most of the positive associations found are not causally established, since the influence of other possible confounding factors or covariates is not ruled out. In the context of multicompartment models for diffusion signals, comparing imaging results with underlying pseudo-, pathological evidence is fundamental to validating the model, as multicompartment models make numerous assumptions and simplifications (to cite a few: fixed diffusivities [Alexander et al., 2010], no exchange [Lasič et al., 2011], indirect account of the volume occupied by myelin [Assaf et al., 2008]). Achieving specificity is of key importance as those challenges manifest through different mechanisms, involving specific cell populations, all playing potentially different roles in disease causation and progression. In this thesis, we argue that by combining advanced dw-MRI sequences with mathematical models based on neurobiological knowledge of brain parenchyma

morphology, together with an experimental design that allows for measuring well-characterized parenchymal challenges, the diffusion characteristics within specific tissue compartments, and even cell types, could be measured, therefore filling an important gap of knowledge.

II. AIMS AND OBJECTIVES

The present study aims to enhance the utility of diffusion MRI in detecting and characterizing pathological events useful in the context of neurological disorders, facilitating the development of sensitive biomarkers for disease detection, progression, and potential therapeutic monitoring.

In this regard, the main objective is to advance the development, validation, and application of advanced diffusion MRI techniques for non-invasive characterization of microstructural and cellular changes in the brain, bridging findings from preclinical models to human neurological conditions. To achieve this, our work plan included the following objectives:

1. **To establish a framework to validate advanced dw-MRI biomarkers' sensitivity and specificity to measuring cellular and microstructural changes in neurological conditions.**
    1.1. Develop and validate an experimental paradigm capable of distinguishing microglia, astrocytes, neurons, and extracellular space contributions during neuroinflammation.
    1.2. Validate an experimental paradigm for generating controlled acute axonal damage.

2. **To develop and validate in animal experimental paradigms biomarkers of early pathological changes in neurodegenerative or inflammatory brain diseases.**
    2.1. Investigate microglial and astrocyte reactivity in response to neuroinflammation using animal models, characterizing their behavior across time and conditions with MRI and histological analyses.

2.2. Establish a rodent model of axonal damage to validate MRI-based axonal diameter mapping, linking imaging findings with histological and electron microscopy evidence.

3. To characterize neurodegeneration, inflammation and axonal damage in humans.

3.1. Map microstructural features in humans *in vivo*, particularly those associated with glia reactivity, by using dw-MRI.

3.2. Apply MRI protocols to human MS patients to detect axonal integrity alterations in NAWM, particularly in early disease stages, and assess correlations with clinical features.

III. MATERIALS AND METHODS

In this section, we will first introduce the cell-specific tissue challenges implemented in rats and describe the human cohorts included in this thesis. Then, we will describe the imaging experimental setup in both animals and humans and the data analysis pipeline followed.

Implementing cell-specific tissue challenges in rats

In this subsection, we will describe the implemented cell-specific tissue challenges used to generate focal inflammation and axonal damage in rats in a controlled fashion.

Experimental subjects

A total of 62 Male Wistar rats, weighing between 250-300 g, were employed for the preclinical procedures. All the experiments received ethical approval from the Instituto de Neurociencias (Alicante, Spain) and its Animal Care and Use Committee, in compliance with Spanish law 32/2007 and European regulations (EU directive 86/609, EU decree 2001-486, and EU recommendation 2007/526/EC). Rats were housed in groups of 3-4, with 12-hour/12-hour light/dark cycle, lights on at 8:00, at room temperature (23 ± 2°C) and food and water *ad libitum*.

Animal preparation

All animals underwent stereotaxically intracerebral injections targeting both dorsal hippocampi. Unless otherwise specified, the right dorsal hippocampus was injected with the active compound, while the left dorsal hippocampus received an equivalent volume of saline. Stereotaxic surgeries were performed following standard procedures as described in the literature (Espinosa-Oliva et al., 2013; Geiger et al., 2008). The injection coordinates for rat dorsal hippocampi relative to the bregma-lambda axis were as follows: anterior-posterior (AP) -3.8 mm, latero-medial (LM) ±2.0 mm, dorso-ventral (DV) -3 mm.

Experimental design

Specific experimental group designs, involving active compound injections and targeted brain cell reaction times, were developed to address the research objectives outlined above. The dorsal hippocampus was chosen as region of interest (ROI) because its well-defined axonal tracts restrict drug spread to the target area—radiolabeled tracers confirm confinement along the dorso-ventral axis (Rossato et al., 2018)—and its bilateral symmetry allows one hemisphere to receive the drug while the other, injected with saline, acts as an internal control (Amaral et al., 2007), strengthening within-animal comparisons. Broadly, the experimental group can be casted into two general models based on the injected compound and the resulting physiological response: (1) neuroinflammation paradigm, and (2) axonal damage paradigm. After variable post-injection intervals (depending on the time needed to develop the condition of interest), the rats underwent MRI scans, followed by immediate perfusion and subsequent immunohistochemical analysis. Group sample sizes were determined through power calculation based on the expected effect size, derived from changes in mean diffusivity reported in rat gray matter in a previous study on inflammation (De Santis et al., 2020). The organization of the experimental groups is illustrated in Figure 2.1 and is defined as follows:

1. Neuroinflammation paradigm:

- Group 1.1 - Isolated microglia reactivity paradigm:

To investigate the reactive microglia independently of any concurrent astrogliosis. A post-injection time window of 7 - 9 hours was employed, utilizing a cohort of 6 rats.

- Group 1.2 - Microglia and astrocytes reactivity paradigm:

To examine the simultaneous microglia and astrocyte reactivity. A post-injection time window of 24 hours was employed, utilizing a cohort of 11 rats.

- Group 1.3a - Isolated astrocyte reactivity paradigm:

To investigate astrogliosis independently of microglia, rats were treated with the CSF1R inhibitor PLX5622 (Plexxikon Inc., California, USA), which depletes ~90% of microglia (Han et al., 2017). PLX5622 was administered simultaneously via two methods: (1) as a dietary supplement (1200 ppm, Research Diets) and (2) by daily intraperitoneal injection (50 mg/kg, 10 mL/kg) for seven days. On the final day, all rats received intracerebral LPS injections. A post-injection time window of 24 hours was employed, utilizing a cohort of 7 rats.

- Group 1.3b - Sham control for Isolated astrocyte reactivity paradigm:

A CSF1R inhibitor PLX5622 sham group, receiving control food and vehicle injections, was included. A post-injection time window of 24 hours was employed, utilizing a cohort of 4 rats. This group, in which both microglia and astrocytes were made reactive, was histologically similar to Group 2 and therefore was combined with it.

- Group 1.4 - Return to homeostatic state microglia and astrocytes paradigm:

To investigate both microglia and astrocytes returning to their homeostatic state. A post-injection time window of 15 days was employed, utilizing a cohort of 5 rats.

The above-mentioned paradigms (Groups from 1.1 to 1.4) were established by injection 2 μl of lipopolysaccharide (LPS) derived from Escherichia coli (Sigma-Aldrich ref.L2880, Madrid, Spain), as described by Espinosa-Oliva et al., (2013), at 2.5 $\mu g/\mu l$ concentration. LPS, a

component of Gram-negative bacteria cell walls (Herrera et al., 2000), induces inflammation by releasing cytokines and nitric oxide, among others (Chao et al., 1992; Giulian, 1993), while preserving neuronal viability and morphology. This approach leveraged the specific time-window of microglia–immediate–and astrocyte reactivity–delayed by 24 hours–to the compound. In addition, in a group of animals we implemented pharmacological pre-treatments to depleted microglia. Therefore, by focusing the analysis on the following specific combinations of waiting times and treatments, we ensured that the measured metrics accurately reflected the isolated contributions of these cell types (Jeong et al., 2010).

- Group 1.5a - Neurotoxic lesion paradigm with high neuroinflammatory response:

To study the concomitant hippocampal inflammatory response under neural loss paradigm. A post-injection time window of 14 days was employed, utilizing a cohort of 3 rats.

- Group 1.5b - Isolated neurotoxic lesion paradigm with low neuroinflammatory response:

To isolate neurodegeneration from the accompanying neuroinflammatory response and test dose-dependent response in our analysis, we introduced an additional group of animals that received an ibotenic acid injection alongside a treatment regimen of minocycline hydrochloride (Sigma-Aldrich, Madrid, Spain). This broad-spectrum tetracycline antibiotic is known to reduce microglial and astrocyte reactivity (Cheng et al., 2015), thereby selectively targeting neuronal cells. Minocycline was administered intraperitoneally at a dose of 45 mg/kg for five consecutive days, commencing on the day preceding the ibotenic acid stereotaxic injection. A cohort of 6 additional rats was used.

To induce neurodegeneration with concomitant inflammation, groups 1.5a and 1.5b were injected with 1 μl of ibotenic acid (IBO) at 2.5 $\mu g/\mu l$ concentration was performed, following Drouin-Ouellet et al. (2011) procedure. This neurotoxic aminoacid (Cayman Chemical Company ref. 14584, Michigan, USA), derived from *Amanita* mushrooms, is known to

selectively lesion neural population by overexciting NMDA receptor (Zinkand et al., 1992). This excitotoxic insult triggers a cascade of events, including neuroinflammation, particularly within regions rich in NMDA receptors, such as the dentate gyrus (Abe et al., 1992). By utilizing this model, we aimed to define a fingerprint in the MRI signal capable of disentangling inflammation with and without neuronal loss, therefore demonstrating the utility of our approaches to investigate both neurodegenerative and neuroinflammatory processes.

- Group 1.6 - Inflammation with demyelination paradigm:

To investigate the inflammation response in the context of demyelination. A post-injection time window from 14 to 21 days was employed, utilizing a cohort of 5 rats.

To induce inflammation with demyelination, a 1 μl injection of 1% L-α-lysolecithin (Sigma-Aldrich ref.L1381, Madrid, Spain; LYS) diluted in saline was administered, following the protocol of Woodruff & Franklin (1999). Lysolecithin, a known membrane-disrupting agent, exhibits selective toxicity towards myelinated cells, resulting in disruption of myelin sheath (Ou et al., 2016).

2. Axonal damage paradigm:
    - Group 2.1 - Axonal damage paradigm:

To investigate the Wallerian-like axonal degeneration process (Conforti et al., 2014) within the fimbria tract, a major axonal output bundle of the hippocampus. The same experimental procedure as group 1.5a was used, utilizing a cohort of 19 rats (partial overlapped with 1.5a).

- Group 2.2 - Shrinkage measure paradigm

To quantify the shrinkage during tissue processing, an additional group of 3 rats was used to measure volumetric changes from the *in vivo* state to the post-perfusion, post-fixation, and post-embedding stages.

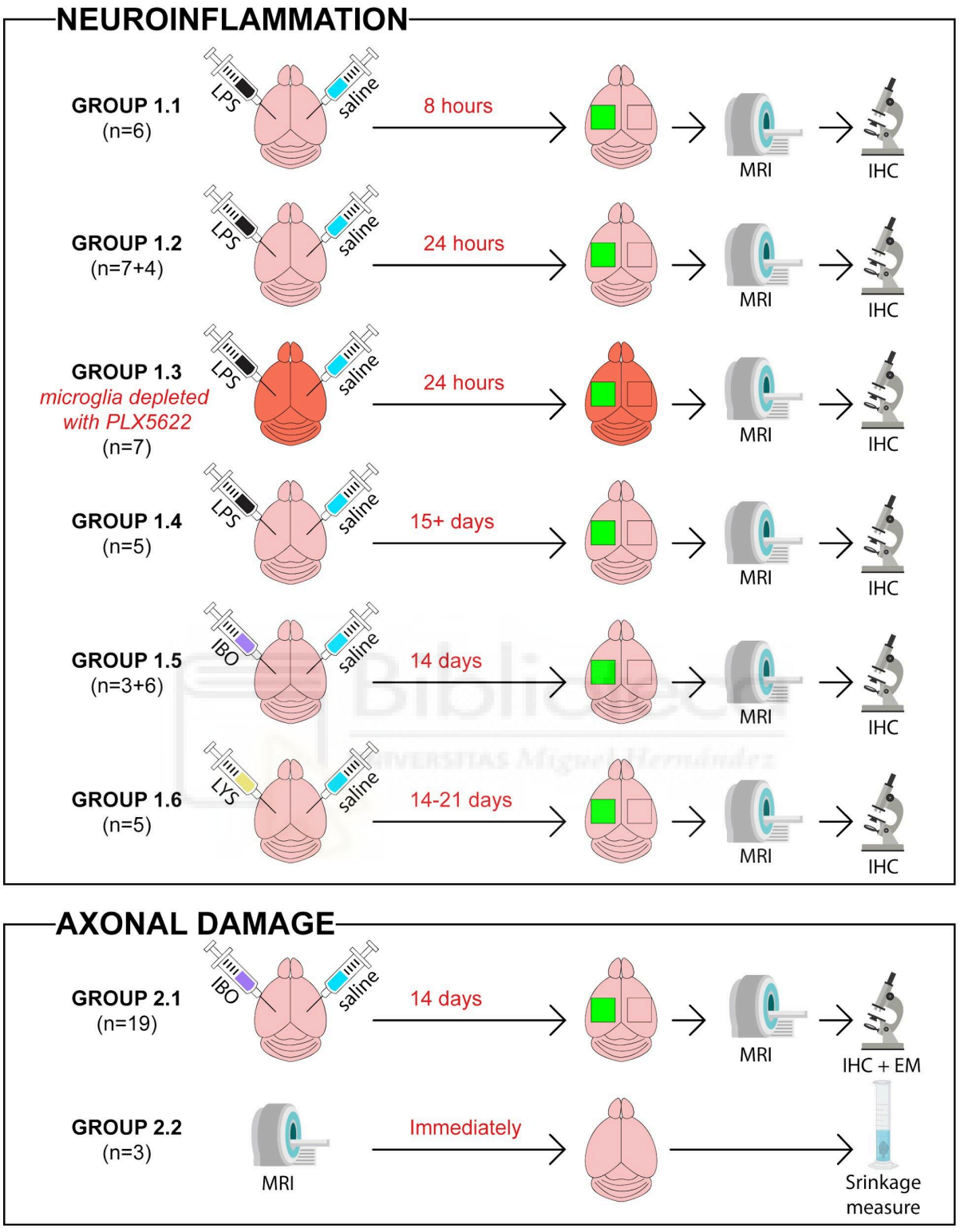

Figure 2.1. Experimental design. Schematic representation of the experimental setup, illustrating the bilateral stereotaxic injection of the different compounds, the corresponding sample sizes, the time intervals used to develop animal paradigms for addressing each

scientific question and the techniques employed throughout the process. *MRI = Magnetic Resonance Imaging; IHC = Immunohistochemistry; EM = Electron microscopy.*

MRI acquisition

MRI preclinical experiments were conducted using a 7-Tesla scanner (Bruker, BioSpect 70/30, Ettlingen, Germany) with a maximum gradient strength of 700 mT/m. This system was equipped with a receive-only phased-array coil incorporating an integrated combiner and preamplifier, paired with an actively detuned transmit-only resonator.

Diffusion-weighted MRI data were acquired using stimulated echo acquisition mode (STEAM) sequences. A total of 30 uniformly distributed gradient directions were employed, with b-values of 0 (between 3 or 4), 2000 (15) and 4000 (15) s/mm². Diffusion times (Δ) were set at 15, 25, 40, and 60 ms, with a diffusion pulse width (δ) of 5 ms, a repetition time (TR) of 7000 ms, and an echo time (TE) of 25 ms. This specific combination of b-values and diffusion times yielded 132 unique volumes per subject. Fourteen horizontal slices were acquired with a field of view (FOV) of 25 mm^2, a matrix size of 110 × 110, an in-plane resolution of 0.225 mm^2, and slice thickness of 0.6 mm. To investigate the Wallerian-like axonal degeneration process within the fimbria tract, the FOV was centered on this white matter track (group 2.1). For the remaining experiments involving diffusion MRI data acquisition, the FOV was centered on the hippocampal regions.

Additional sequences were acquired: A T_{1w} sequence with TR of 300 ms, TE = 12.6 ms, and 2 averages; a T_{2w} sequence with TR of 3000 ms, TE of 7.7 ms, and 4 averages were acquired. An additional T_{2w} high-resolution MRI protocol covering the entire brain was obtained with TR of 8000 ms, TE of 14 ms, 4 averages, FOV = 25 mm^2, matrix size = 200 × 200, in-plane resolution of 0.125 mm^2, and 56 slices with a thickness of 0.5 mm. In addition, three relaxometry sequences were acquired with the same geometry as the dw-MRI data: a gradient echo sequence with TR of 1500 ms, 30 equally spaced TE ranging from 3.3 to 83.4 ms, and 3 averages.

A subset of 9 animals from Group 2.1 underwent a similar protocol, employing lower b-values of 1000 and 2500 s/mm² to explore a protocol with lower b-values and thus enhanced clinical feasibility.

To quantify tissue shrinkage during processing, group 2.2 underwent a high-resolution T_{2w} MRI scan of the entire brain. This scan utilized a Rapid Acquisition with Relaxation Enhancement (RARE) sequence with the following parameters: TR = 6253 ms, TE = 11 ms, and 4 averages. The acquisition covered 56 slices with a FOV of 25 mm^2, a matrix size of 200 x 200, an in-plane resolution of 0.125 mm^2, and a slice thickness of 0.5 mm.

The total scan time, including animal preparation, was approximately two hours.

Data analysis

Diffusion-weighted multi-compartment inflammation model

The proposed dw-MRI multi-compartment inflammation model was developed by extending previous multi-delta, multi-b-value dw-MRI approaches described in earlier works. Specifically, it builds on concepts introduced in the AxCaliber model (Assaf et al., 2008), which enables the estimation of axonal caliber distributions in white matter, and on advanced gray-matter methodologies sensitive to neurites, such as Watson-dispersed sticks (Hansen et al., 2013). Our aim was to design a framework capable of capturing cell-specific contributions from microglia and astrocytes, while also accounting for neuronal and myelin fractions. The approach leverages the distinct diffusion regimes, geometries, and size scales of these cellular populations to extract biologically interpretable biomarkers.

Accordingly, the diffusion-weighted signal was fitted to the following multi-compartment representation:

$$S = f_{IC} \times S_{IC}(\kappa) + f_{SS} \times S_{SS}(R_{SS}) + f_{LS} \times S_{LS}(R_{LS}) + f_{EC} \times S_{EC} + (1 - f_T) \times S_{FW}$$

In this mathematical model, the different parameters among tissue and cell compartments are as follows and can be schematically visualized in figure 2.2:

- f_{IC} represents the fraction of restricted diffusion in cylinders ("sticks"), associated with microglial processes and axons. The corresponding signal term (S_{IC}) is modeled as cylinders with negligible radius and Watson-distributed orientations (Assaf et al., 2008; Hansen et al., 2013), with the Watson dispersion parameter (κ) accounting for the orientation distribution of the processes. Given the relatively short TE used in our acquisitions (25 ms), it is possible that a minor contribution from myelin water is also captured within this compartment.
- f_{SS} and f_{LS} represent the fractions of restricted diffusion in small and large spheres, corresponding to microglial somata and astrocytes, respectively. Their signal terms (S_{SS}, S_{LS}) are modeled as restricted diffusion in spheres according to Neuman's solution (Neuman, 1974), as implemented in soma-and-neurite imaging approaches (Zhang et al., 2012; Palombo et al., 2020).
- f_{EC} denotes the fraction of water undergoing hindered diffusion in the extracellular space. The signal term (S_{EC}) is modeled as a cylindrically symmetric diffusion tensor aligned with the mean stick orientation, in line with NODDI-like formulations (Zhang et al., 2012).
- $(1 - f_T)$ corresponds to the free water fraction, modeled as an unrestricted Gaussian compartment (Pasternak et al., 2009).

The fitting parameters for this model are f_{IC} , f_{SS} , f_{LS} , κ , R_{SS}, R_{LS}, the diffusivities of the extracellular tensor, and f_T. Restricted water diffusivity inside the restriction is assumed to be $1\,x\,10^{-9} mm^2 s^{-1}$ as indicated by Zhang et al. (2012). A slow-exchange regime between compartments was assumed (Lee et al., 2020). Two non-overlapping initialization ranges were defined for the sphere radii (4 and 8 μm, respectively) to ensure convergence and separation of the microglial and astrocytic contributions.

Preprocessed dw-MRI data were input into a custom MATLAB pipeline (R2018a, The MathWorks). Model fitting was performed by nonlinear least-squares optimization (*lsqnonlin*)

with physiologically constrained parameter bounds, convergence criteria of 10,000 iterations, and tolerances of 10^{-6}. The average fitting speed was 5.9 seconds per voxel.

This formulation therefore explicitly states the assumptions and approximations underlying each compartment: Watson-dispersed sticks for processes, Neuman-based spheres for somata, a radially symmetric hindered tensor for extracellular water, and a Gaussian free-water term. Together, these choices provide a tractable yet biologically grounded model of gray-matter inflammation (García-Hernández et al., 2022).

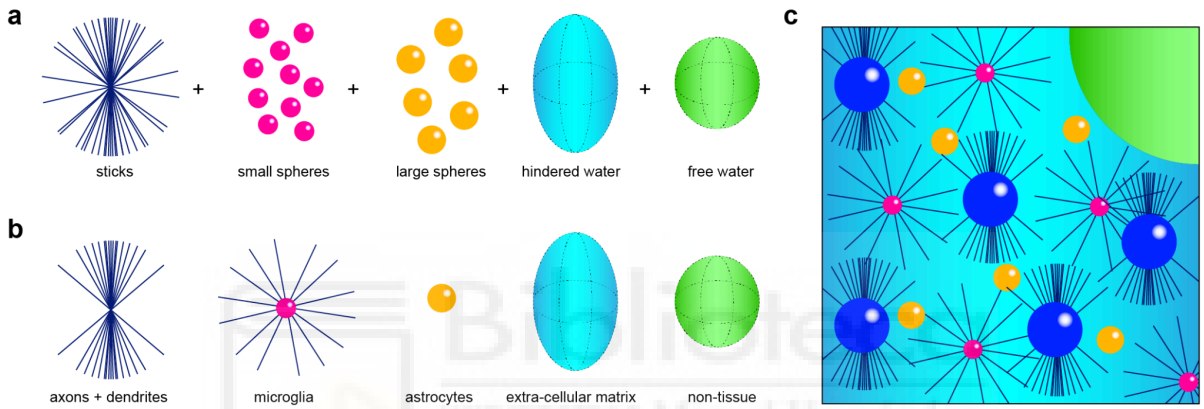

Figure 2.2. Diffusion-weighted multi-compartment inflammation model. Multi-compartment model elements **a** and what they represent in the biological tissue b**:** sticks (axons + dendrites), sticks and small spheres (microglia), large spheres (astrocytes), hindered water (extracellular matrix), and free water (non-tissue, accounting for neurons). **c.** Grey matter visual representation constituting the parenchyma in the model: microglia, astrocytes, neurons, extracellular space. Source: Garcia-Hernandez et al. (2022).

AxCaliber model

To estimate the average axonal diameter proxy, dw-MRI data were utilized to fit the AxCaliber model in both rats and humans. AxCaliber interprets the diffusion signal by considering two distinct compartments: one that reflects hindered diffusion (denoted as (·)h) and another that captures restricted diffusion (denoted as (·)r). The hindered component is

analyzed using the conventional DTI framework, where D_h represents the diffusion tensor. In contrast, the restricted compartment models the white matter microstructure as a collection of cylindrical elements with radial symmetry, implying negligible diffusion in the radial direction. The signal from this compartment is broken down into components aligned with and orthogonal to the cylinder axis. Assuming the cylinders are significantly longer than the typical diffusion path length, the parallel signal component can be expressed as a simple one-dimensional exponential decay governed by the longitudinal diffusion coefficient $D_{||}$. However, the perpendicular component is more complex due to its dependence on the cylinder radius, R; the detailed formulation for this component is not presented here but is available in Vangelderen et al. (1994). A distinctive feature of AxCaliber is its accommodation of axonal radius variability. Although the initial model relied on a gamma distribution to represent this variability, the challenges involved in accurately estimating both its shape and scale parameters prompted a shift toward using a Poisson distribution (De Santis et al., 2016). This alternative approach simplifies modeling by requiring only the estimation of the mean, λ, which serves as both the mean and variance of the distribution, offering a practical approach for implementing the method; therefore, achieving a clearer biological interpretability.

Therefore, the overall model for the diffusion signal is expressed as:

$$S(b,\ g)\ = f_h \cdot S_h(b,g)\ + f_r \sum_{i=0}^{n} \omega(R_i) S_r(b,g,R_i),$$

where f_h, f_r are the fractions of the restricted and hindered components, S_h, S_r are the diffusion signals of those compartments, b is the diffusion weighting factor, g is the gradient orientation and $\omega(R_i)$ are the normalized weights from the Poisson distribution.

The theoretical framework originally outlined by (De Santis et al., 2019b) was adapted to account for the dependence of the extra-axonal signal on diffusion time. This modification

introduced a linear term, expressed as $\lambda\perp_{(\Delta min)} + Slope * (D - D_{(min)})$. Although this representation simplifies the dependency proposed by Burcaw et al. (2015), it is considered a parsimonious approach, justified by the relatively narrow range of values examined compared to prior studies on time dependency (De Santis et al., 2016; Fieremans et al., 2016). Additionally, a comparison of linear and non-linear models using the Bayesian Information Criterion (BIC) consistently favored the linear model, with 100% preference across subjects.

The fitting process was implemented using a cascade model, as described in Harms et al., (2017). Initially, the CHARMED model (Assaf & Basser, 2005) was fitted to data acquired at shorter Δ to initialize volume fractions. The intra-axonal axial diffusivity and primary fiber orientations, estimated during this CHARMED fit, were fixed during the AxCaliber fitting. The radial diffusivity of the extra-axonal compartment at the shortest Δ was first modeled using the tortuosity approximation (Zhang et al., 2012). Subsequently, this constraint was relaxed in a final iteration, where all model parameters except the radial diffusivity and noise factor were fixed. The fitted parameters included the restricted main orientations and volume fractions, intra-axonal axial diffusivity, extra-axonal radial diffusivity, the slope of radial diffusivity decay with increasing Δ, the axonal diameter, and the Rician noise term. For STEAM data, an additional T_1 decay term was incorporated, with the BIC indicating a preference for a mono-exponential T_1 decay over a bi-exponential model in 98% of the evaluated voxels.

MRI processing

Raw MRI data were converted from Paravision V6.0 to nifti (The Neuroimaging Informatics Technology Initiative) format. Raw MRI data was processed using in-house Matlab (MATLAB R2023a) scripts combining tools from FSL V5.0 (https://fsl.fmrib.ox.ac.uk), DIPY (Garyfallidis et al., 2014), and ANTs (Advanced Normalization Tools) (Avants et al., 2014) as follows. First, FSL *bet* (brain extraction tool) was used to remove the skull from the T_{2w} and dw-MRI

data, separately for each contrast. The skull removal was performed in three steps: first, the *bet* function was run for each map, then each individual mask was manually corrected using the *FSLeyes* tool, and finally the skull was removed by applying the corrected mask. Raw dw-MRI unweighted b-value 0 volumes were nonlinearly registered to the T_{2w} scan to correct for echo-planar imaging distortions using ANTs *anstsRegistration* function. Output transformation files were applied to the rest of the volumes using ANTs *antsApplyTransforms* function. Correction for movement artifacts and eddy currents was implemented using the FSL *eddy* tool.

Subsequently, pre-processed dw-MRI data with b-values of 1000 s/mm² and the shorter diffusion time were processed using a robust model fitting approach RESTORE (Chang et al., 2005) implemented in the ExploreDTI toolbox (Leemans & Jones, 2009) to generate DTI metrics. Pre-processed multi-shell, multi-diffusion times dw-MRI data with b-values of 2000 and 4000 s/mm² were utilized to fit both the AxCaliber model (Assaf et al., 2008) and our MCM using an in-house MATLAB script (The Mathworks Inc., Natick, MA). For the axonal degeneration model, the fimbria was reconstructed bilaterally using the DTI-based tractography algorithm in the software ExploreDTI (Leemans et al., 2009). Injection sites were aligned and defined as the origin for the analyzed tract portions.

For the neuroinflammation paradigm groups, Mean diffusivity (MD) and fractional anisotropy (FA) maps from the DTI model; Axonal Diameter (AX) maps from the AxCaliber model (only group 1.5a); Stick fraction, Stick dispersion, Small sphere radius, Large sphere radius, and Tissue fraction maps were extracted from our MCM for each subject. T_{1w}-, T_{2w} MR sequences were used to compute T_1/T_2 maps. T_2* maps were calculated by fitting an exponential decay to the T_2*-weighted MR sequences acquired at different echo times. Finally, for the axonal damage paradigm group 2.1, mean AX values along the fimbria tracts were obtained for each animal in both hemispheres.

Tissue processing

- Immunohistochemistry

Immediately following MRI acquisition, animals were euthanized with an intraperitoneal injection of sodium pentobarbital (46 mg/kg, Dolethal, E.V.S.A. laboratories, Madrid, Spain). Subsequently, transcardial perfusion was performed with 100 ml of 0.9% warm phosphate-buffered saline (PBS), followed by 100 ml of ice-cold 4% paraphormaldehyde (PFA; BDH, Prolabo, VWR International, Lovaina, Belgium). Brains were carefully extracted and post-fixed in 4% PFA for one hour at room temperature with gentle agitation. The brains were then embedded in 3% agarose/PBS (Sigma-Aldrich, Madrid, Spain) and sectioned into 50 μm-thick coronal slices using a vibratome (VT 1000S, Leica, Wetzlar, Germany).

To prepare the tissue for immunohistochemistry, sections were rinsed three times in 0.5% Triton X-100 in PBS for 10 minutes each. Subsequently, they were blocked with a solution containing 4% bovine serum albumin (BSA) and 2% goat serum in 0.5% Triton X-100 BS for two hours at room temperature. Sections were then incubated overnight at 4ºC with primary antibodies against the following targets: Iba-1 (1:1000, Wako Chimicals, Osaka, Japan) for microglia, GFAP (1:1000, SigmaAldrich, Madrid, Spain) for astrocytes, myelin basic protein (1:250, Abcan, Cambridge, UK) for axons and dendrites , and NeuN (1:250, Merck Milipore, Madrid, Spain) for neurons.

Prior to antibody incubation, sections for myelin basic protein staining underwent an antigen retrieval step involving a 15-minute incubation in 1% citrate buffer (pH 6) with 0.05% Tween-20 at 80ºC.

Following primary antibody incubation, sections were incubated with secondary antibodies conjugated to fluorescent dyes (1:500, Thermo Fisher Scientific, Waltham, USA) for two hours at room temperature. Subsequently, sections were counterstained with DAPI (15 μM, Sigma-Aldrich, Madrid, Spain) for 15 minutes at room temperature. Finally, sections were mounted on slides using a custom-made anti-fade mounting medium composed of 1:10

propyl gallate:Mowiol (Sigma-Aldrich, MAdrid, Spain; Merck Milipore, Massachusetts, USA) to minimize autofluorescence and preserve fluorophore signal over time.

- ❖ Electron microscopy

A subgroup of 6 rats from Group 2.1 underwent tissue processing for electron microscopy acquisition. Rats were euthanized with an intraperitoneal injection of sodium pentobarbital (46 mg/kg, Dolethal, E.V.S.A. laboratories, Madrid, Spain). Subsequently, transcardial perfusion was performed with 100 ml of 0.9% phosphate-buffered saline (PBS), followed by 100 ml of fixative solution containing 2% paraformaldehyde and 2.5% glutaraldehyde in 0.1 M cacodylate buffer (pH 7.3). Brains were extracted and post-fixed overnight in the same fixative solution at 4 ºC.

The following day, brains were washed in 0.1 M cacodylate buffer and sectioned into 250 μm -thick horizontal slices using a vibratome (Leica VT1000S, Germany). Sections containing the fimbria were selected, washed three times in 0.1 M cacodylate buffer, and post-fixed in 1% osmium tetroxide in 0.1 M cacodylate buffer for 1.5 hours at 4 ºC. After washing in distilled water, the tissue was dehydrated in a graded ethanol series, followed by propylene oxide.

The tissue was then infiltrated with a mixture of propylene oxide and Agar 100 embedding resin for two hours at room temperature, followed by overnight incubation in fresh resin. The samples were transferred to fresh resin and polymerized for 20 hours at 60 ºC. Ultrathin sections (90 nm) were cut using an ultramicrotome (Leica UC7) and placed on formvar-coated copper slot grids. The sections were stained with lead citrate and imaged using scanning transmission electron microscopy (STEM) on a scanning electron microscope (Zeiss GeminiSEM 460, Germany).

❖ Volume measure

To assess post-mortem volume changes, *ex vivo* measurements were obtained at four time points: immediately post-perfusion, and at 4-, 7-, and 10-days post-perfusion in rats from group 2.2.

In vivo volumes were calculated by counting the number of voxels corresponding to brain tissue in the T_{2w} images and multiplying this number by the voxel volume. *Ex vivo* volumes were measured using the Archimedes' principle. Briefly, the fixed brain was submerged in a known volume of fixative solution, and the resulting volume displacement was measured.

Microscopy image processing

For immunofluorescence analysis, tissue sections were examined using a Leica DM4000 fluorescence microscope (Leica, Wetzlar, Germany) equipped with a QICAM Qimaging camera 22577 (Biocompare, San Francisco, USA) and Neurolucida morphometric software (MBF, Biosciences, VT, USA). Microglia and astrocytes were visualized and reconstructed using 20x and 40x objectives, respectively. Only cells with intact and clear processes were included in the analysis. Cells were manually traced throughout the entire section thickness using a ¨live¨ tracing method, adjusting the microscope focus as needed. The resulting 2D diagrams and 3D reconstructions were saved for subsequent analysis.

Morphometric analysis of the complete cellular structures was performed using Neurolucida Explorer software (MBF Bioscience, VT, USA). A total of 820 cells (410 microglia and 410 astrocytes) were randomly selected from the dentate gyrus of each hemisphere. We focus on the parameters for which analogous quantity was extracted from the dw-MRI analysis to be able to compare the two quantifications. Hence, for reconstructed microglia (figure 2.3b left), we extracted the following parameters: (1) cell body volume (CBV; figure 2.3c), quantifying the volumetric extent of the microglial cell body (approximated as a sphere for our multi-delta multi-b-value dw-MRI protocol); (2) process density (PDen; figure 2.3d), a measure of the density of neurites emanating from the cell body; (3) process dispersion

(PDis; figure 2.3e), characterizing the spatial distribution of neurites around the cell body. PDis was assessed through the construction and analysis of polar plots, where lower values indicate a more uniform distribution of neurites, suggesting a more isotropic distribution of processes, potentially influencing the diffusion of water molecules in the surrounding tissue.

To estimate astrocyte volume, we employed 3D convex analysis, a method that approximates the cell as a convex hull. This approach was necessary due to the limitations of GFAP immunostaining, which can underestimate astrocyte morphology. GFAP staining and reconstruction (figure 2.3b right) often fail to capture the full extent of astrocytic processes, which are enveloped by an actin membrane. By applying convex hull analysis, we were able to account for the unstained portions of the astrocyte, providing a more accurate estimate of its total volume. This method, originally described by Rodieck (1973) and further refined by SheikhBahaei et al. (2018), requires detailed 3D reconstruction of GFAP-positive processes, as illustrated in figure 2.3f.

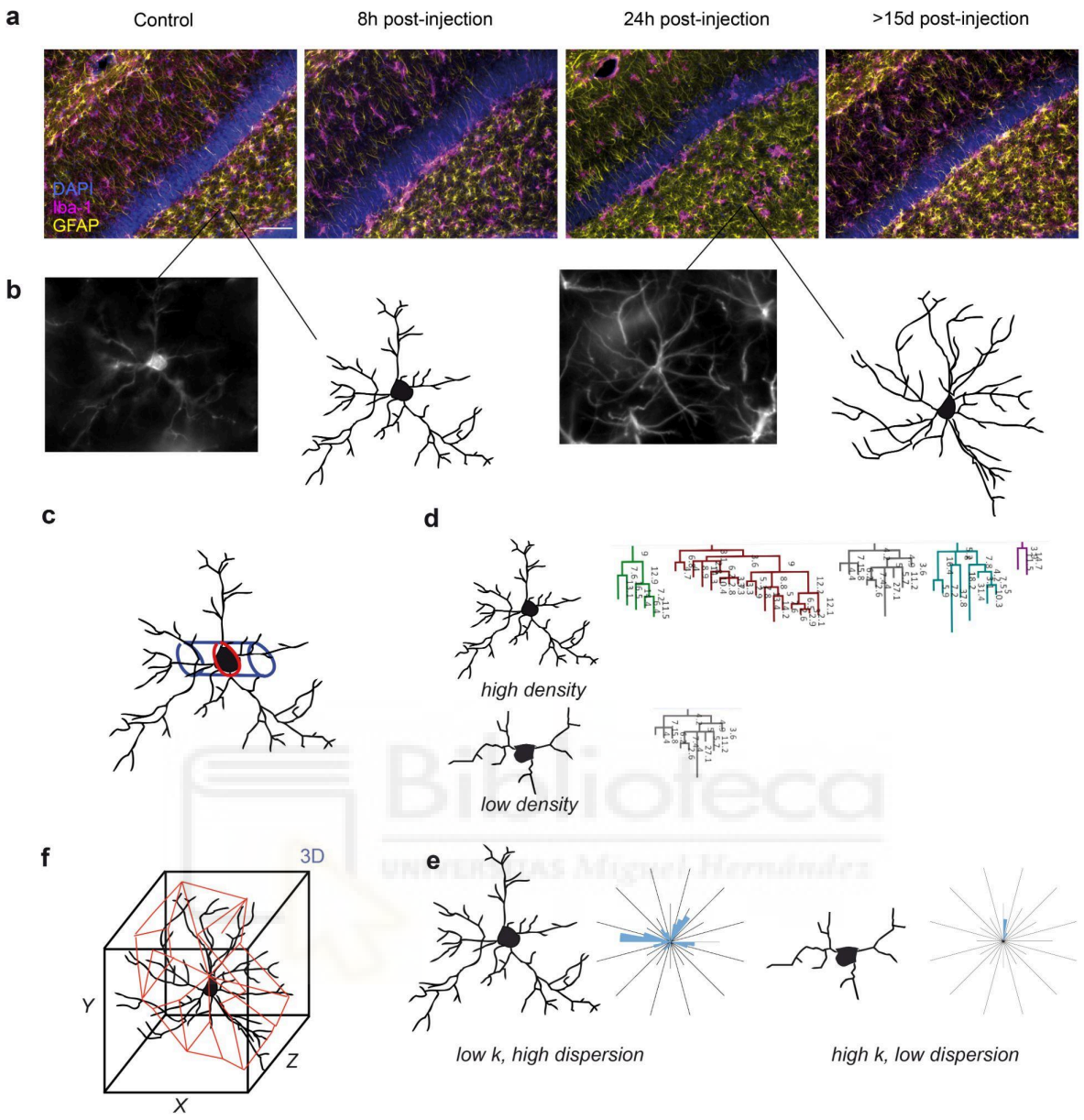

Figure 2.3. Histology main methods and morphometric features obtained. a. Representative microphotographs of the histological labeling at the different time-points. Green = Iba1 (microglia), red = GFAP (astrocytes), blue = DAPI (cell nuclei). Scale bar = 100 µm. **b.** Zoom in of a microglia and astrocyte and their 3D reconstruction for morphometric analysis. **c.** Microglia cell size extraction by cross-sectional area determination. **d.** Microglia's fiber density extraction, showing two representative cases of high and low densities. **e.** Microglia polar plots for fiber orientation analysis, showing two representative cases of low Watson dispersion parameter κ (indicating high fiber dispersion along the main orientation)

and high κ (indicating low fiber dispersion). **f.** Astrocyte convex hull extraction. Source: Garcia-Hernandez et al. (2022).

Microglia and astrocyte cell density analysis was performed as follows: images of the dentate gyrus were acquired in 12-bit grayscale using the above-mentioned microscope and manually delineated according to the Franklin and Paxinos rat brain atlas (Paxinos & Franklin, 2019). Semi-automated quantification was conducted using the spot detector tool in Icy software (Icy Software, Paris, France).

A threshold for detecting positive nuclei was established for each experimental condition based on the average nuclear size (converted to pixel size) and a signal-to-noise ratio exceeding 23% of the cell body intensity relative to the background level. This threshold was determined based on the Rayleigh criterion for resolution, which defines the minimum distance between two distinguishable points (Rayleigh, 1903). The signal-to-noise ratio was calculated by measuring fluorescence intensity along a line intersection of both the cell body and the background. This process was repeated for multiple microglia and astrocytes to assess staining quality across experimental batches. Data were collected from both control and treated hemispheres in at least five slices per animal.

To assess the integrity of myelin sheaths, neuronal ramifications, and neuronal loss, we quantified the intensity of immunofluorescence staining for myelin basic protein (MBP), neurofilament, and NeuN, respectively. Images were acquired in 12-bit grayscale and analyzed using Icy software. Two square ROIs measuring 100 μm^2 were placed in the dentate gyrus. For MBP and neurofilament analysis, ROIs were positioned in the hilus, as previously described (Long et al., 2021). For NeuN analysis, ROIs were placed in the granule cell layer, where neuronal cell bodies are predominantly located (Morris et al., 2024). Data were collected from both hemispheres in at least five slices per animal.

Finally, to analyze axonal morphology, the images were binarized, and axon quantification was performed semi-automatically by operators who were blinded to animal identities and

experimental conditions. The inner area of each cell was detected automatically using the MATLAB function *bwconncomp*, while non-axonal structures were excluded through manual visual inspection. Six images per condition per animal were analyzed, resulting in a total of 12,272 segmented axons.

Table 1 provides a comprehensive summary of the correspondences between the measurements derived from the MCMs and those obtained through histological analysis.

Table 1. Dw-MRI and histological measurement equivalencies.

	Dw-MRI model measurement	Histological markers	Histological measurement
Microglia	Small spheres Stick fraction Stick dispersion	IBA-1	Cell body volume Process ramifications Dispersion
Astrocytes	Big spheres	GFAP	Convex hull volume
Myelin	Stick fraction	MBP	Staining MBP density
Neuronal cell body	Tissue fraction	NeuN	Staining NeuN density
Neuronal axon	Alpha parameter	Osmium Neurofilament	Axonal swelling

Note. IBA-1 = Ionized Calcium-Binding Adapter Molecule 1; GFAP = Glial Fibrillary Acidic Protein; MBP = Myelin Basic Protein; NeuN = Neuronal Nuclei.

Statistics

For statistical analysis and visualization of the primary results, we employed RStudio (RStudio 2025 Inc., Boston, MA, USA) and GraphPad Prism 7 software (GraphPad Software Inc., La Jolla, CA, USA).

After assessing the normality of data distribution, paired t-tests were conducted between the control and injected hemispheres for each condition, encompassing both dw-MRI and

histological results. Pearson correlation was used for linear regression analyses, with significance determined via Fisher's (1925) test (Edwards, 2005). For MRI data, repeated-measures analysis of variance (ANOVA) was performed to evaluate the effects on injection and group, followed by post hoc t-test to compare the injected and control hemispheres, with corrections applied for multiple comparisons.

For data representation, the analysis aimed at emphasizing relative changes rather than absolute values. Accordingly, all data presented in the results section, including both MRI and histological findings, are expressed as ratios of change calculated using the following formula:

$$Change = \frac{Treated - Control}{Control}$$

For the axonal degeneration model, paired t-tests were conducted to evaluate differences in histological measurements and axonal diameters between the injected and contralateral fimbria. To assess the effect of ibotenic acid injection, repeated-measures ANOVA were performed, with tract location, treatment (IBO vs. saline), and their interaction (tract location*treatment) included as factors. When the assumption of sphericity was violated, p-values were adjusted using the Greenhouse-Geisser correction. Post hoc comparisons between treatments at each tract location were corrected for multiple comparisons using the false discovery rate (FDR) method.

Human cohort

In this subsection, we aimed to translate advanced dw-MRI techniques, originally developed in preclinical models, into human research. Specifically, our objectives were twofold: first, to demonstrate the feasibility of mapping inflammatory processes in the gray matter of healthy individuals using the novel multi-delta multi-b-value protocol; and second, to characterize axonal pathology in patients with MS via a Wallerian-like axonal degeneration biomarker. These investigations are designed to bridge the gap between preclinical findings and clinical

application, ultimately enhancing our understanding of neuroinflammatory and neurodegenerative processes in the human brain.

Humans Acquisition

For the human experiments, we collected data through collaborations with the Cardiff University Brain Research Imaging Centre (CUBRIC), Wales, UK, to evaluate the translatability of our MRI protocol and with the MGH/HST Athinoula A. Martinos Center for Biomedical Imaging in Boston, Massachusetts, USA, to assess the translatability of the dw-MRI axonal degeneration biomarker in MS patients. Both centers provided access to a Siemens 3T Connectom scanner with the required specifications to seamlessly transfer protocols developed in rat models to human studies (Jones et al., 2018). Specifically, their equipment supports the application of a wide range of b-values, enabling the use of varying degrees of diffusion weighting through gradient intensities comparable to those used in preclinical animal scanners. Additionally, it facilitates the implementation of longer diffusion times without incurring excessive signal loss.

To assess the translatability of our multi-delta multi-b-value dw-MRI model to humans, six healthy participants underwent imaging five times each in the context of a reproducibility study, resulting in a total of 30 acquisitions. The study was approved by the Institutional Review Board of Cardiff University.

To assess the translatability of the dw-MRI axonal degeneration biomarker, eleven patients with MS (age range: 26-57 years; 6 males) and ten healthy controls (age range: 23-53 years; 4 males) participated in this study. The minimum sample size required to detect the effect was determined based on prior research (Huang et al., 2016). Participants were matched for age and sex across groups. Eligibility criteria for MS patients included a confirmed diagnosis of relapsing-remitting MS (Polman et al., 2011), stable use of disease-modifying treatments or no treatment for at least three months, and no corticosteroid use within one month of the study. Physical disability was assessed by a neurologist using the Expanded Disability Status Scale (EDSS) (Kurtzke, 1983), and cognitive performance was evaluated using the

Symbol Digit Modalities Test (SDMT) (A. Smith, 2016). The study was approved by the local Institutional Review Board, and all participants provided written informed consent. Demographic and clinical data are presented in Table 2.

Table 2. Demographic characteristics of the studied cohort.

	HC (n=10)	MS (n=11)	*p*-value
Age, years (Mean ± SD)	35 ±11	43 ±12	0.27
Sex, n (Male)	6	4	0.13
DD, years (Mean ± SD)		6.40 ±5.47	
DD < 5 years		4	
EDSS (Median, Min-Max)		2 1-4.5	
SDMT (Mean z-score ± SD)		–0.70 ±1.47	
Medication		1 avonex; 1 plegridy; 2 tecfidera; 1 gilenya; 3 ocrelizumab; 2 copaxone; 1 Rituximab	

Note. SD = Standard Deviation; DD = Disease Duration; EDSS = Expanded Disability Status Scale; SDMT = Symbol Digit Modalities Test. The reported p-value is the outcome of the Chi-square test comparing Multiple Sclerosis and Healthy Controls for categorical variables, or independent samples t-test for continuous variables.

MRI acquisition

All participants were scanned using a Siemens 3T Connectom scanner, a customized version of the 3T MAGNETOM Skyra system (Siemens Healthcare, Erlangen, Germany). This scanner is equipped with gradient coils capable of producing a maximum gradient strength of 300 mT/m. A 64-channel brain array coil (Keil et al., 2013) was utilized for data acquisition.

For the multi-delta multi-b-value dw-MRI model translational study, dw-MRI data were acquired using an echo-planar imaging diffusion sequence with the following parameters: TE, 80 ms; TR, 3.9 s; Δ , 17.3, 30, 42, and 55 ms; and b-values of 2000 and 4000 s/mm^2, with 30 and 60 uniformly oriented gradient directions, respectively. Six B0 images were acquired for each diffusion time, yielding a total of 384 images per acquisition. Additional acquisition parameters included a flip angle of 90º, slice thickness of 2 mm, in-plane voxel size of 22 mm, FOV of 220 mm^2, and matrix size of 110 x 110. The total scan duration was approximately 40 minutes per participant.

Dw-MRI participant data on the axonal degeneration biomarker study were acquired using a spin-echo echo-planar imaging diffusion sequence with 273 uniformly distributed gradient directions. Imaging parameters included b-values of 0 (1), 2000 (30), and 4000 (60) s/mm²; Δ of 17, 35, and 61 ms; and a diffusion pulse width of 7 ms. Additional imaging parameters were TR of 5000 ms, TE of 89 ms, FOV of 220 mm², matrix size of 110 × 110, in-plane resolution of 2 mm², slice thickness of 2 mm, partial Fourier factor of 7/8, and a GRAPPA acceleration factor of 2. Eighty-two slices were acquired to cover the whole brain, along with four non-diffusion-weighted images. Anatomical images were also obtained using 3D sequences with a 1.0 mm isotropic voxel size. T_{1w} multiecho magnetization-prepared rapid gradient-echo (MPRAGE) images (van der Kouwe et al., 2008) were acquired for all participants, while fluid-attenuation inversion recovery (FLAIR) images were acquired in MS patients to facilitate white matter lesion segmentation. The total acquisition time per participant was approximately 1 hour.

Data analysis

MRI processing

The preprocessing of human dw-MRI data was conducted using a combination of software tools, including FreeSurfer V5.3.0 (https://surfer.nmr.mgh.harvard.edu) and FSL V5.0 (https://fsl.fmrib.ox.ac.uk). Preprocessing steps encompassed gradient nonlinearity

correction (Glasser et al., 2013), motion correction, and eddy current correction with corresponding b-matrix reorientation (Andersson & Sotiropoulos, 2016). Additional corrections were applied for signal drift (Vos et al., 2017) and Gibbs ringing artifacts (Kellner et al., 2016). Further details regarding these preprocessing methods can be found at http://www.humanconnectome.org/.

In the multi-delta multi-b-value dw-MRI model human study, diffusion data were subsequently registered to a skull-stripped structural T_{1w} image using the *epireg* algorithm (Andersson & Sotiropoulos, 2016). Nonlinear registration of B0 scans to a high-resolution human brain template was performed using advanced normalization techniques (Klein et al., 2009), and the resulting inverse transformations were employed to map the Desikan GM parcellation into single-subject space (Desikan et al., 2006). To minimize contamination from adjacent white matter, masks were eroded by one voxel using the FSL *fslmaths* command. B0 scans were used to segment gray and white matter regions, retaining only voxels with minimal white matter contamination (<5%) for subsequent analyses. Intra- and intersubject coefficients of variation were calculated for each MRI measure. The Desikan parcellation scheme was employed to compute the mean and standard deviation (SD) of stick fraction and dispersion parameters within eight regions of interest (ROIs): hippocampus, cerebellum, substantia nigra, basal ganglia, thalamus, motor cortex, frontal cortex, and occipital cortex. These measures were correlated with postmortem histological staining for microglia, as reported by Mittelbronn et al. (2001). For all multiple sclerosis patients, lesion masks were segmented on FLAIR images using a semiautomated method implemented in 3D Slicer v4.2.0 (https://www.slicer.org).

For the groupwise analysis of NAWM, we utilized a previously established method (De Santis et al., 2019a). In brief, FA maps, calculated using the lowest Δ and b-value, were used to initialize the initial steps of an enhanced version of tract-based spatial statistics (TBSS) (Smith et al., 2006). This modified TBSS approach incorporates highly precise coregistration techniques (Klein et al., 2009). During the warping procedure, lesion masks

were excluded from the similar metric calculation to ensure accurate registration. Statistical analysis was conducted using a permutation-based, nonparametric inference framework for general linear modeling (Winkler et al., 2014). The model included group and disease duration as regressors to evaluate their association with NAWM microstructural changes. Lesion masks were excluded from statistical testing, and corrections for multiple comparisons across clusters were implemented using threshold-free cluster enhancement (TFCE). Additionally, we performed voxel-wise analyses to explore associations between axonal diameter and clinical measures, specifically the Expanded Disability Status Scale (EDSS) and the Symbol Digit Modalities Test (SDMT), in MS patients. To further investigate disease progression, we computed the mean MRI-derived axonal diameter proxy for each participant across the entire white matter, excluding lesion regions in MS patients. The mean values were compared across three groups: healthy controls, MS patients with a disease duration of less than five years, and MS patients with a disease duration of five years or more.

IV. RESULTS

In this section, we briefly summarize the main results on which this thesis is based. We first present the findings of García-Hernández et al. (2022), where controlled, cell-specific challenges were implemented in rats to isolate inflammatory, neurodegenerative, and demyelinating components, thereby enabling the derivation of diffusion-MRI signatures with cellular specificity. The translational potential of this framework was then explored in healthy human cohorts, establishing the reproducibility of microglia- and astrocyte-sensitive diffusion-MRI markers across brain regions.

We then describe the results from Cerdán Cerdá et al. (2024). In the preclinical arm of this study, we validated diffusion-MRI–based axonal diameter mapping in a rat model of selective axonal damage induced by ibotenic acid, combining in vivo MRI, immunohistochemistry, and electron microscopy to confirm axonal caliber enlargement in the absence of demyelination

and considerable axonal loss. In the translational human arm, we applied the same framework to patients with multiple sclerosis, revealing diffuse axonal swelling in normal-appearing white matter, particularly in individuals with shorter disease duration.

Together, these studies establish a cross-scale experimental framework in which advanced diffusion MRI readouts can be interpreted in light of controlled manipulations and histological validation in animals, and subsequently leveraged to interrogate early microstructural alterations in the human brain. For detailed descriptions of all results, the reader is referred to the corresponding published articles.

Mapping microglia and astrocyte activation in vivo using diffusion MRI

In the preclinical arm, we established a set of cell-specific perturbations to generate, in a controlled and temporally segregated manner, focal neuroinflammation, neuronal loss–driven neurodegeneration, and demyelination. This design enabled within-animal hemispheric comparisons to increase sensitivity and reduce inter-subject variance. Advanced multiparametric dw-MRI acquisitions were paired with a histology-informed multi-compartment representation to capture soma- and process-level features and to disentangle restricted from hindered diffusion. Immunohistochemistry provided orthogonal validation of imaging-derived interpretations.

Microglia activation characterized using Iba-1 staining and MRI

Following lipopolysaccharide administration, microglial reactivity emerged rapidly. At 8 h post-injection, Iba-1 staining demonstrated process retraction and soma hypertrophy in the absence of proliferation, a morphological phenotype mirrored by the dw-MRI readout: the “stick fraction,” sensitive to elongated, ramified processes, decreased, while the apparent radius of the small-soma compartment increased (see Figure 3.1). Critically, pharmacological depletion of microglia (PLX5622) abolished these MRI changes, confirming their cellular specificity rather than a non-specific effect of edema or free-water shifts.

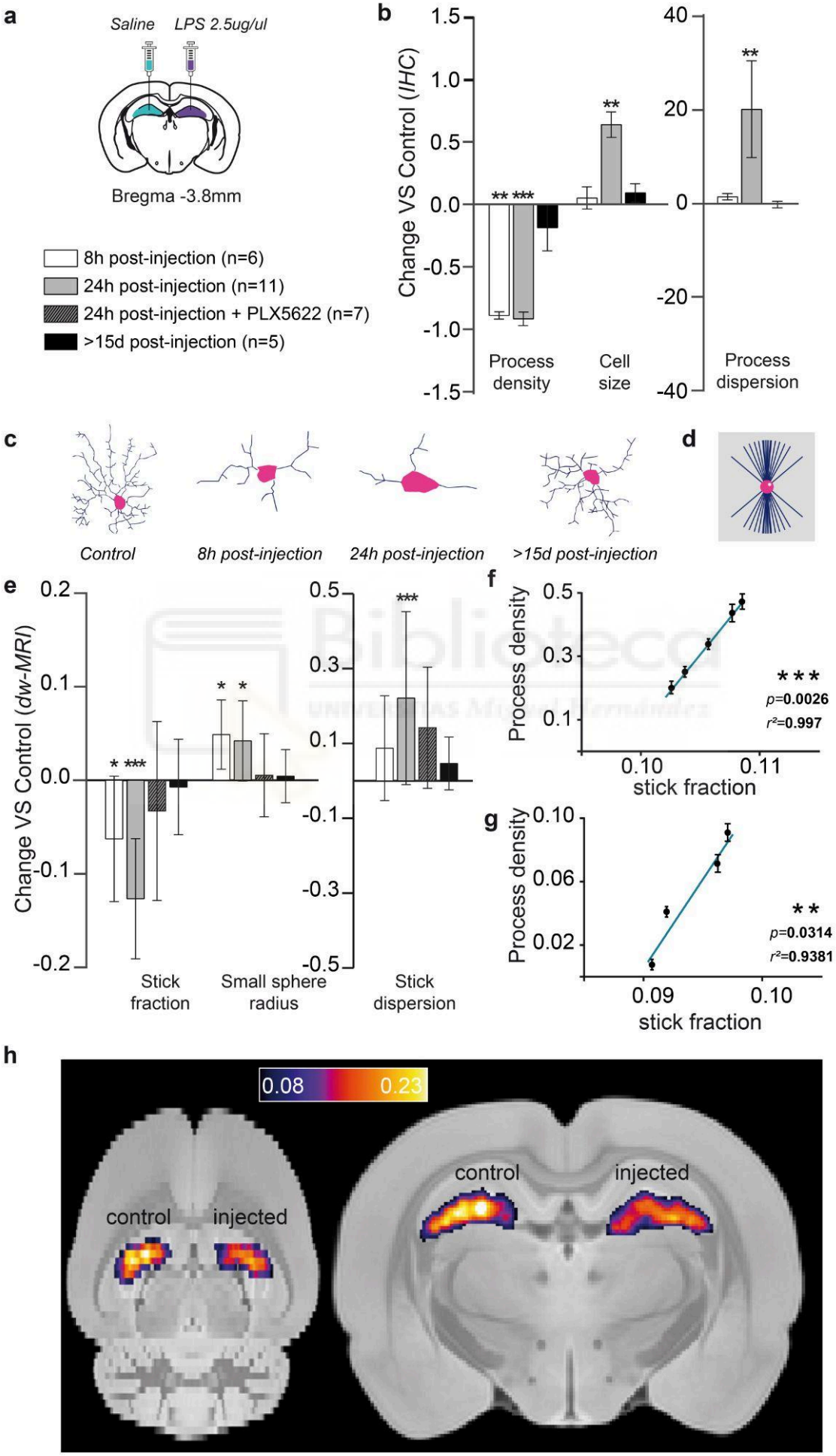
a
Saline
LPS 2.5ug/ul
Bregma -3.8mm
8h post-injection (n=6)
24h post-injection (n=11)
24h post-injection + PLX5622 (n=7)
>15d post-injection (n=5)
b
Change VS Control (IHC)
Process density
Cell size
Process dispersion
c
Control
8h post-injection
24h post-injection
>15d post-injection
d
e
Change VS Control (dw-MRI)
Stick fraction
Small sphere radius
Stick dispersion
f
Process density
stick fraction
p=0.0026
r²=0.997
g
Process density
stick fraction
p=0.0314
r²=0.9381
h
0.08
0.23
control
injected
control
injected

Figure 3.1. Histological characterization of microglia reaction and its associated MRI signature. a. Experimental scheme showing bilateral stereotaxic injection of LPS (left hemisphere)/saline (right hemisphere) and the composition of the four groups: Six animals were scanned 8 hours after injection, 11 animals were scanned 24 hours after injection, 7 animals were treated with PLX5622 for 7 days before the injection and then scanned 24 hours after injection, and 5 animals were scanned 15 days or more after injection. **b.** Normalized change $(P_{injected} - P_{control})/P_{control}$ in process density, cell size, and process dispersion parameter for the injected versus control hippocampus, measured in Iba-1+–stained microglia for the different groups. Asterisks represent significant paired difference between injected and control (**p < 0.01 and ***p < 0.001). Error bars represent SD. IHC, immunohistochemistry. **c.** Morphology reconstruction of representative microglia at the different times. **d.** Geometrical model used for microglia. **e.** Normalized change $(P_{injected} - P_{control})/P_{control}$ between MRI parameter calculated in the injected versus control hemisphere for the microglia compartment. Asterisks represent significant paired difference between injected and control (*p < 0.05 and ***p < 0.001). **f** and **g.** Correlations between stick fraction from MRI and process density from Iba-1 at 8 **f** and 24 hours after injection **g**. **h.** Mean stick fraction maps at 24 hours after injection, normalized to a rat brain template and averaged over all rats. Source: García-Hernández et al. (2022).

Astrocyte activation characterized using GFAP staining and MRI

By contrast, astrocytic hypertrophy unfolded on a delayed timescale. At ~24 h, GFAP immunoreactivity revealed robust astrocyte enlargement which, in the model, was captured as an increase in the large-soma radius. This effect persisted even when microglia were depleted, indicating that the astrocytic signature is dissociable from microglial contributions and can be selectively isolated by timing and pharmacological context (see Figure 3.2).

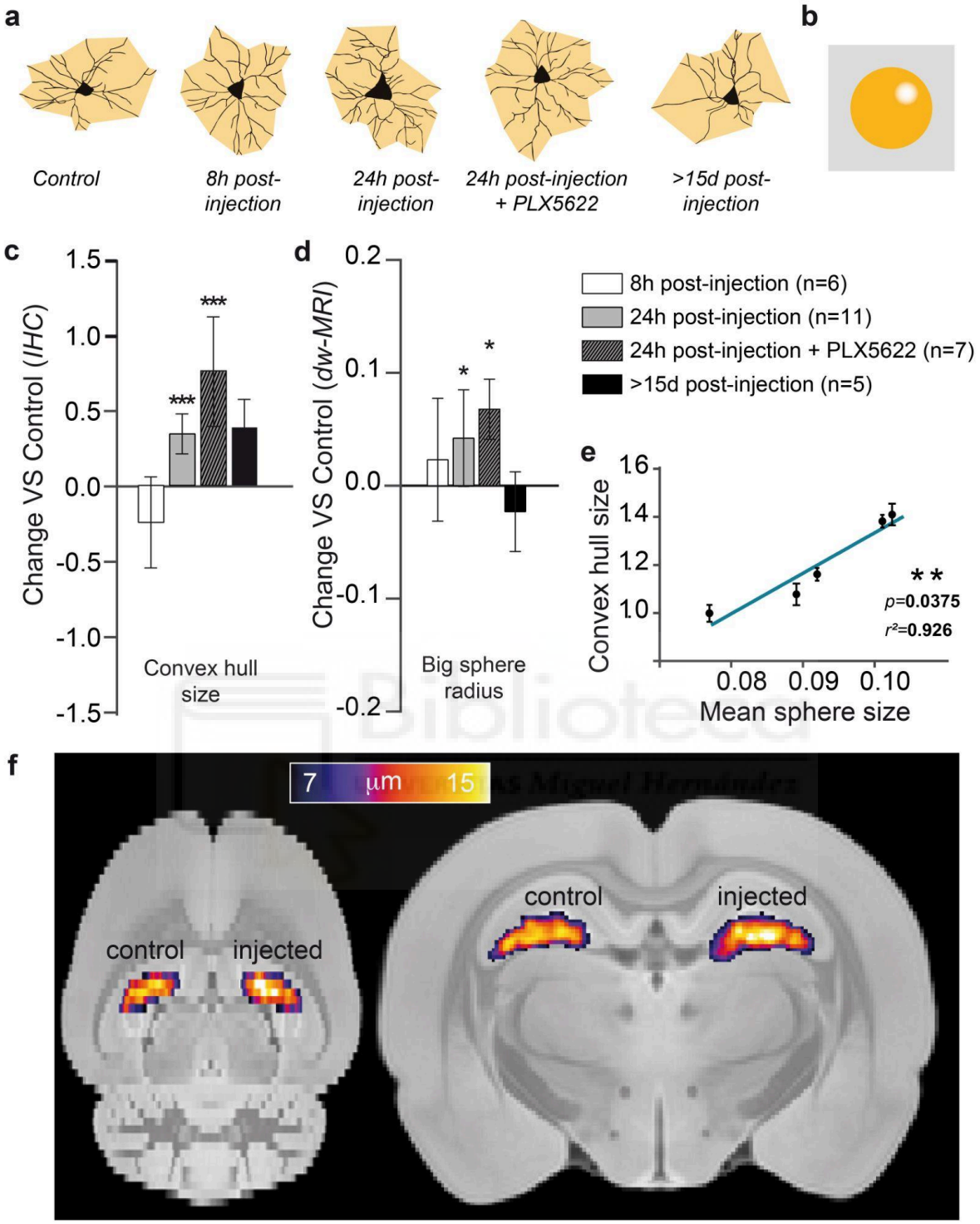

Figure 3.2. Histological characterization of astrocyte reaction and its associated MRI signature. a. Morphology reconstruction of representative astrocytes at the different times in black and two-dimensional (2D) convex hull in orange. **b.** Geometrical model used for astrocytes. **c.** Normalized change $(P_{injected} - P_{control})/P_{control}$ in convex hull mean radius for the

injected versus control hippocampus, measured in GFAP+-stained astrocytes for the different groups. Asterisks represent significant paired difference between injected and control (***$p < 0.001$). Error bars represent SD. **d.** Normalized change $(P_{injected} - P_{control})/P_{control}$ between MRI-derived large sphere radius calculated in the injected versus control hemisphere for the astrocyte compartment (shown in the inset). Asterisks represent significant paired difference between injected and control (*$p < 0.05$). **e.** Correlation between mean sphere radius from MRI and convex hull mean radius from GFAP. **f.** Large sphere radius maps at 24 hours after injection, normalized to a rat brain template and averaged over all rats. Source: García-Hernández et al. (2022).

Concomitant microglia activation and neuronal death characterized using NeuN staining and MRI

To study neurodegenerative alterations, we induced neuronal loss with ibotenic acid. NeuN quantification confirmed reduced neuronal content in the hippocampus, accompanied by microglial proliferation. In dw-MRI terms, this condition produced a decrease in tissue fraction consistent with parenchymal loss and a concomitant increase in the small-soma fraction indexing proliferating microglia. Importantly, anti-inflammatory pretreatment (minocycline) quantitatively attenuated these imaging changes, demonstrating that the derived biomarkers are sensitive to graded biological modulation and are suitable for treatment-response assessment (see Figure 3.3).

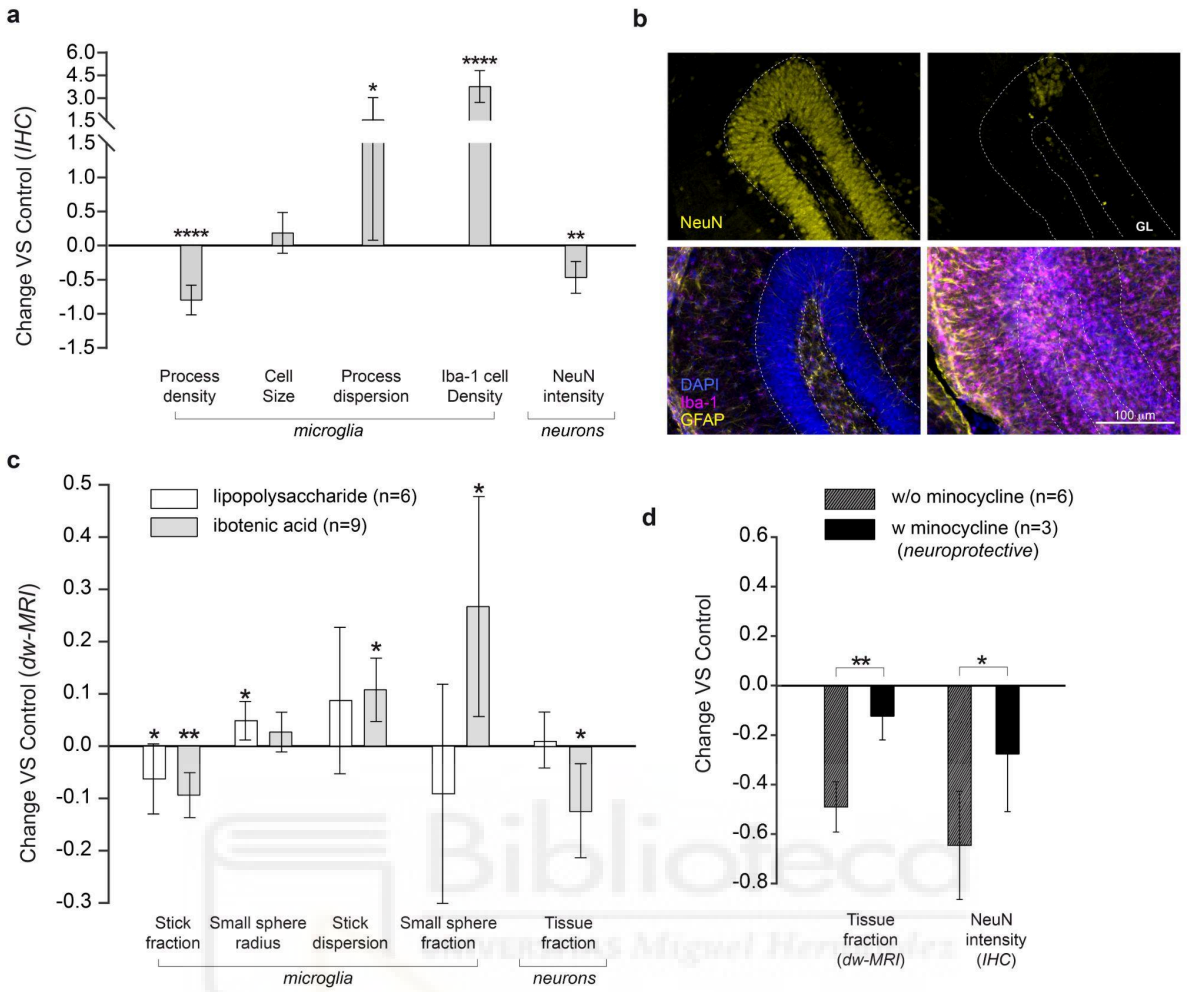

Figure 3.3. Characterization of inflammation in the presence of neuronal death. a. Normalized change $(P_{injected} - P_{control})/P_{control}$ in histological measures for the injected versus control hippocampus. Asterisks represent significant paired difference between injected and control (*p < 0.05, **p < 0.01, and ****p < 0.0001). **b.** NeuN and GFAP–Iba-1 staining of a representative animal (left, control; right, injected). GL, granular layer. **c.** Normalized change $(P_{injected} - P_{control})/P_{control}$ in MRI parameter calculated in the ibotenic-injected versus control hemisphere for microglia and neuron compartments (light gray). For comparison, the same parameters obtained in group 2 of the LPS-injected animals are reported in white. Asterisks represent significant paired difference between injected and control (*p < 0.05 and **p < 0.01). **d.** Normalized change $(P_{injected} - P_{control})/P_{control}$ for MRI and histological markers of neuronal death calculated separately in the untreated animals and in those treated with

minocycline. Asterisks represent significant unpaired difference between the two groups (*p < 0.05 and **p < 0.01). Source: García-Hernández et al. (2022).

Specificity of the model in the presence of demyelination

In a complementary demyelinating paradigm (lysolecithin), myelin basic protein (MBP) loss confirmed myelin disruption while the dw-MRI pattern highlighted the role of extracellular water balance in driving stick-fraction reductions. Parameters linked to process dispersion retained specificity to microglial morphology, illustrating the model's robustness to myelin-related confounds and its ability to distinguish inflammatory from demyelinating effects (see Figure 3.4).

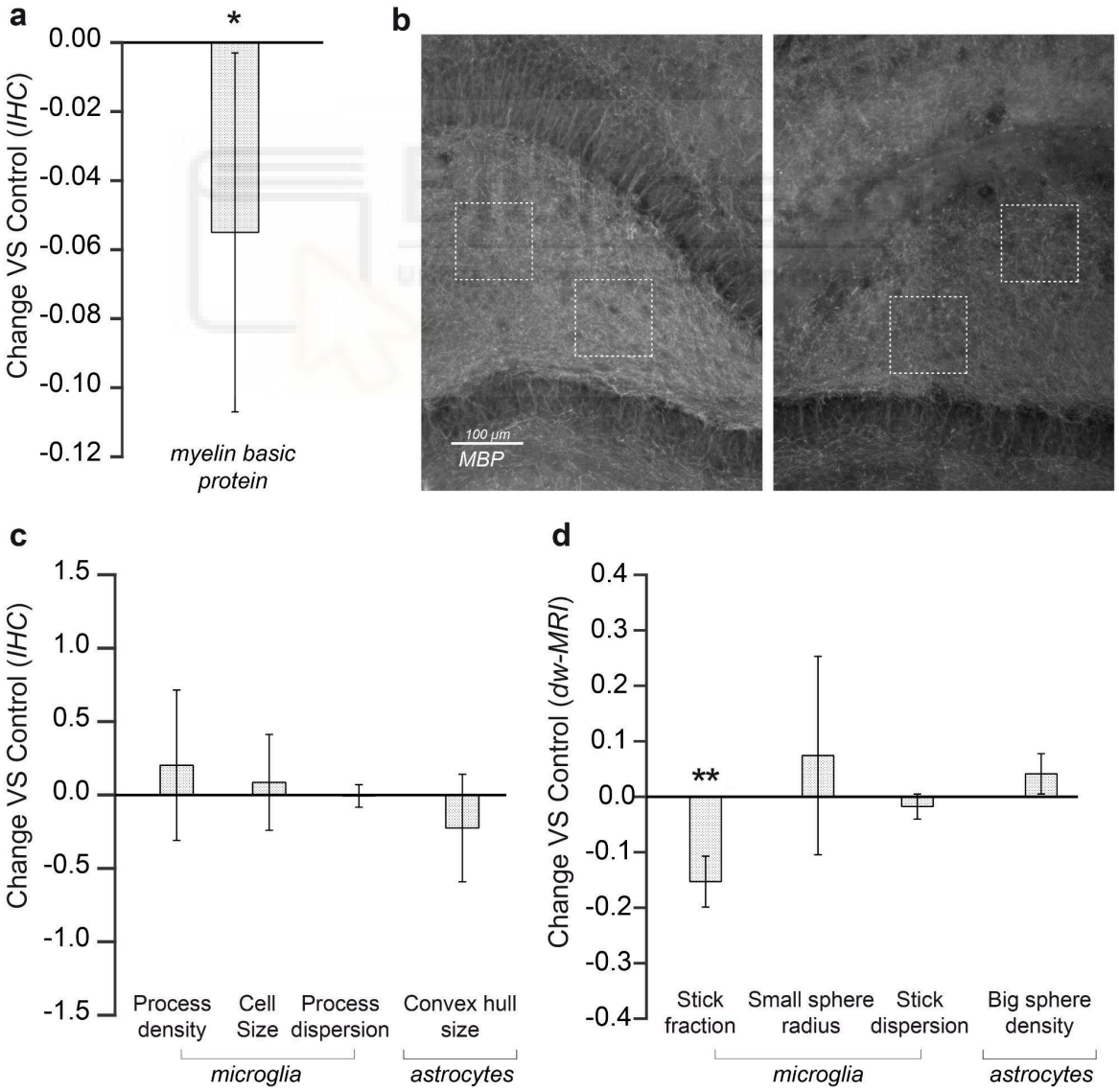

Figure 3.4. Specificity of glia biomarkers in demyelinated tissue. a. Normalized change $(P_{injected} - P_{control})/P_{control}$ in histological Myelin basic protein measures for the injected versus control hippocampus. **b.** MBP staining of a representative animal (left, control; right, injected). **c.** Normalized change $(P_{injected} - P_{control})/P_{control}$ in histological staining calculated in the lysolecithin-injected versus control hemisphere for microglia and astrocyte compartments. **d.** Same as **c** but for MRI parameters. Source: García-Hernández et al. (2022).

Translation to human

We subsequently evaluated the feasibility and anatomical plausibility of the glia-sensitive readouts in healthy humans using the same conceptual acquisition–analysis framework adapted for 3 T scanners. Gray-matter maps of the stick-related metrics (capturing ramified processes) and soma-size indices displayed coherent, regionally structured patterns that were highly reproducible across sessions and hemispheres (coefficient of variation < ~8%; see Figure 3.5).

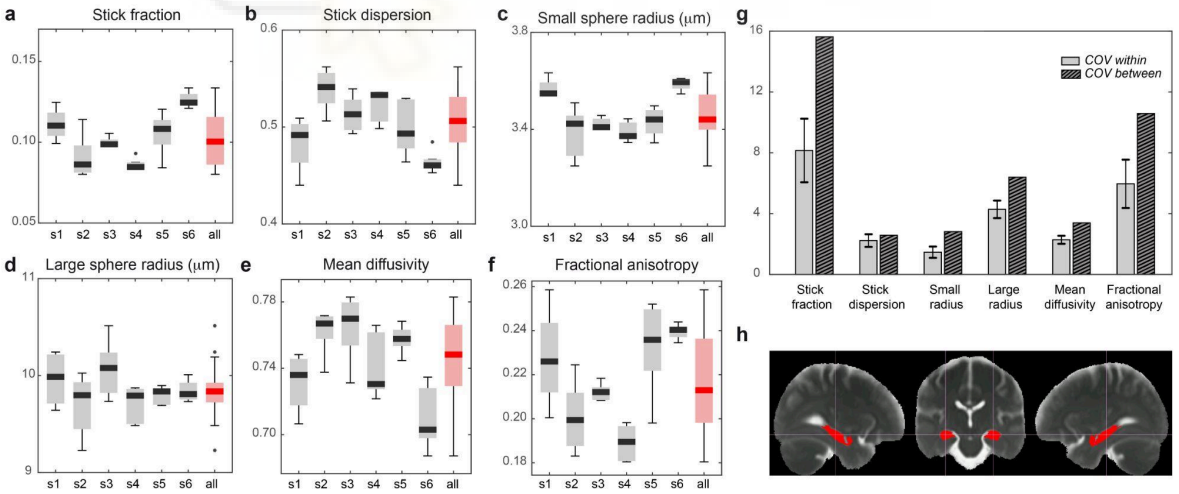

Figure 3.5. Feasibility of the framework translation to human and MR parameter reproducibility analysis. a. Boxplot of stick fraction as measured separately in the hippocampus of six subjects scanned five times (s1 to s6) and pooling all subjects together (red). The same is shown for the stick dispersion parameter **b**, small sphere radius **c**, large

sphere radius **d**, mean diffusivity **e**, and fractional anisotropy **f**. **g.** Average coefficient of variation calculated within subject (light gray) and between subjects (striped). **h.** Region of interest (ROI) in the hippocampus used for the reproducibility analysis, defined according to Desikan et al. (2006). Source: García-Hernández et al. (2022).

Importantly, the spatial distribution of microglia-sensitive parameters showed significant correspondence with literature-based regional microglial density, supporting the biological interpretability of the imaging markers at the macroscale (see Figure 3.6). Altogether, this translational check indicates that the cellularly-informed dw-MRI signatures derived in rodents can be measured reliably in humans, providing anatomically plausible maps of putative microglial and astrocytic features suitable for future clinical applications.

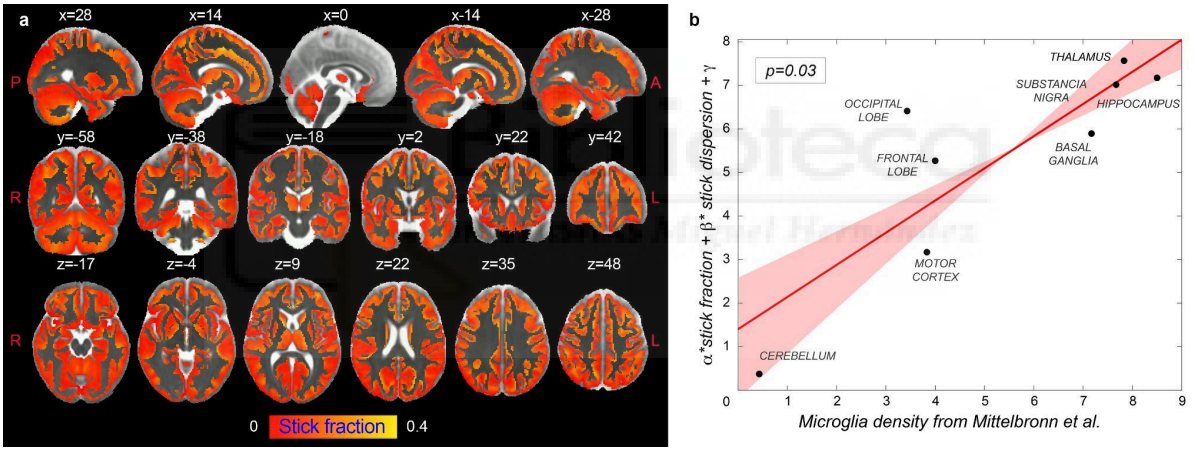

Figure 3.6. Correlation between the stick fraction and microglia density in human brain. a. Stick fraction according to the MCM normalized to the brain template defined in (56), masked for gray matter tissue, and averaged across subjects. **b.** Multiple linear regression using stick fraction and dispersion to explain microglia density measured using histological staining of postmortem human tissue in eight gray matter regions (hippocampus, cerebellum, substantia nigra, basal ganglia, thalamus, motor, frontal, and occipital cortices) as reported in Mittelbronn et al. (2001). Regression confidence intervals are calculated using bootstrap. Source: García-Hernández et al. (2022).

Taken together, these results demonstrate that, under controlled biological manipulations, dw-MRI can (i) differentiate microglial from astrocytic reactivity in gray matter by exploiting temporal windows and depletion strategies, and (ii) disentangle inflammatory signatures from those driven by neuronal loss or demyelination, and (iii) capture these cellularly informed metrics in humans with high reproducibility and anatomically plausible regional distributions. This preclinical-to-human validation underscores the potential of diffusion MRI as a framework to derive cell-specific and biologically meaningful biomarkers of neuroinflammation and neurodegeneration.

A translational MRI approach to validate acute axonal damage detection as an early event in multiple sclerosis

Axonal degeneration is the principal correlate of irreversible disability in multiple sclerosis, yet its noninvasive detection in vivo remains a major challenge. To address this, we developed a translational framework aimed at validating MRI-derived axonal diameter mapping in the context of acute axonal damage. The study combined a preclinical model of selective axonal injury with in vivo MRI, immunohistochemistry, and electron microscopy, and subsequently extended the same protocol to patients with MS. In this way, the work bridges controlled validation in animals with early biomarkers of axonal pathology in human disease.

A rat model of acute axonal damage

We targeted the fimbria to elicit acute axonal damage in a white-matter bundle with clear geometry and projection patterns. Histology confirmed hippocampus neural loss by significantly decreased NeuN intensity and showed increased neurofilament staining consistent with axonal disruption (see Figure 3.7).

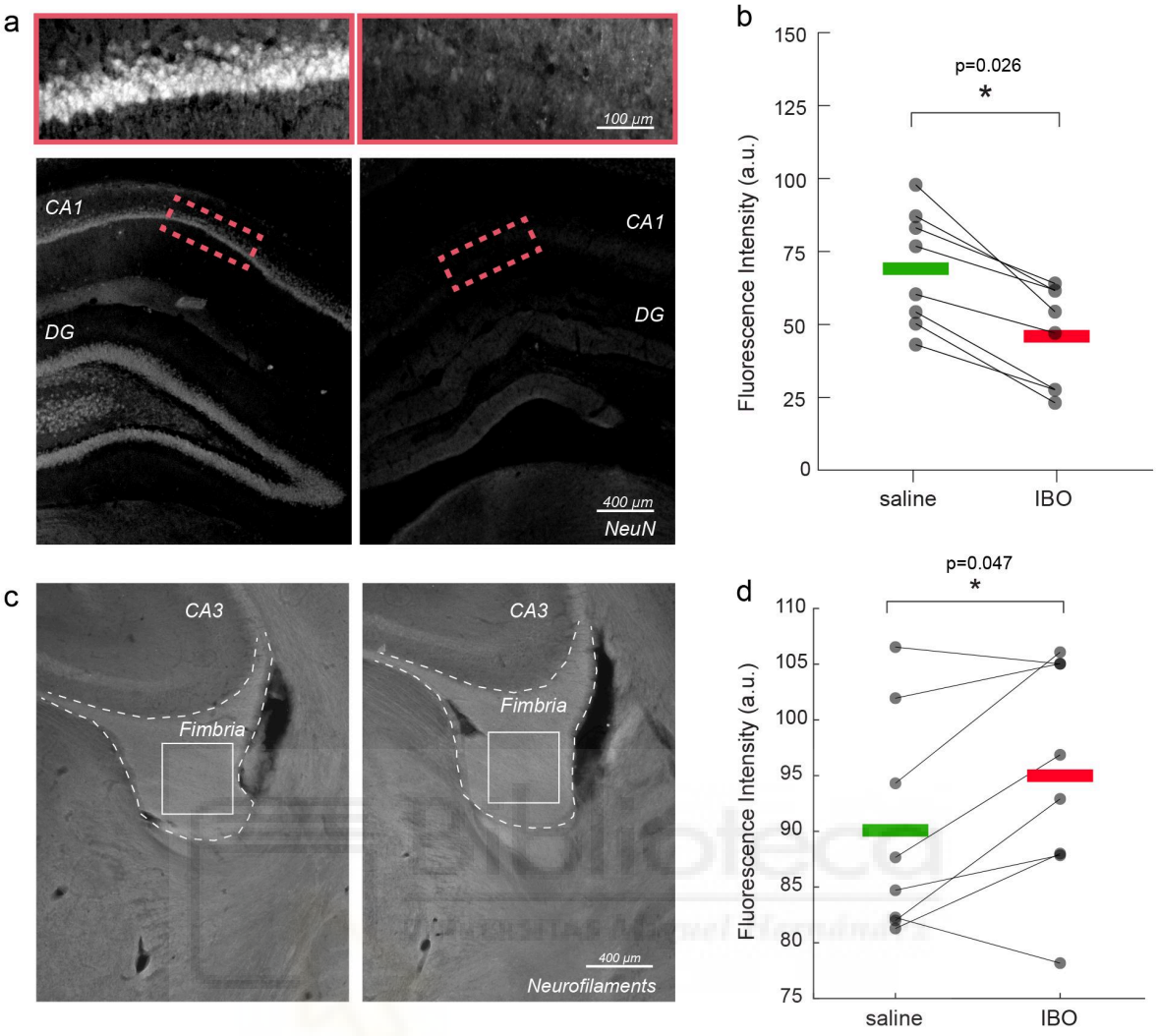

Figure 3.7. Immunofluorescence validation of axonal damage. a. NeuN staining in control vs. injected hippocampi. **b.** Mean NeuN intensity in control vs. injected hippocampi. Asterisks represent significant differences across hemispheres (n=8, paired t test, p=0.026). **c.** Neurofilament staining in control vs. injected fimbria. **d.** Mean neurofilament intensity in control vs. injected hippocampi. Asterisks represent significant differences in means across hemispheres (n=8, paired t test, p=0.047). Source: Cerdán Cerdá et al. (2024).

Scanning transmission electron microscopy confirmed an enlargement of axonal caliber without significant axonal loss (see Figure 3.8).

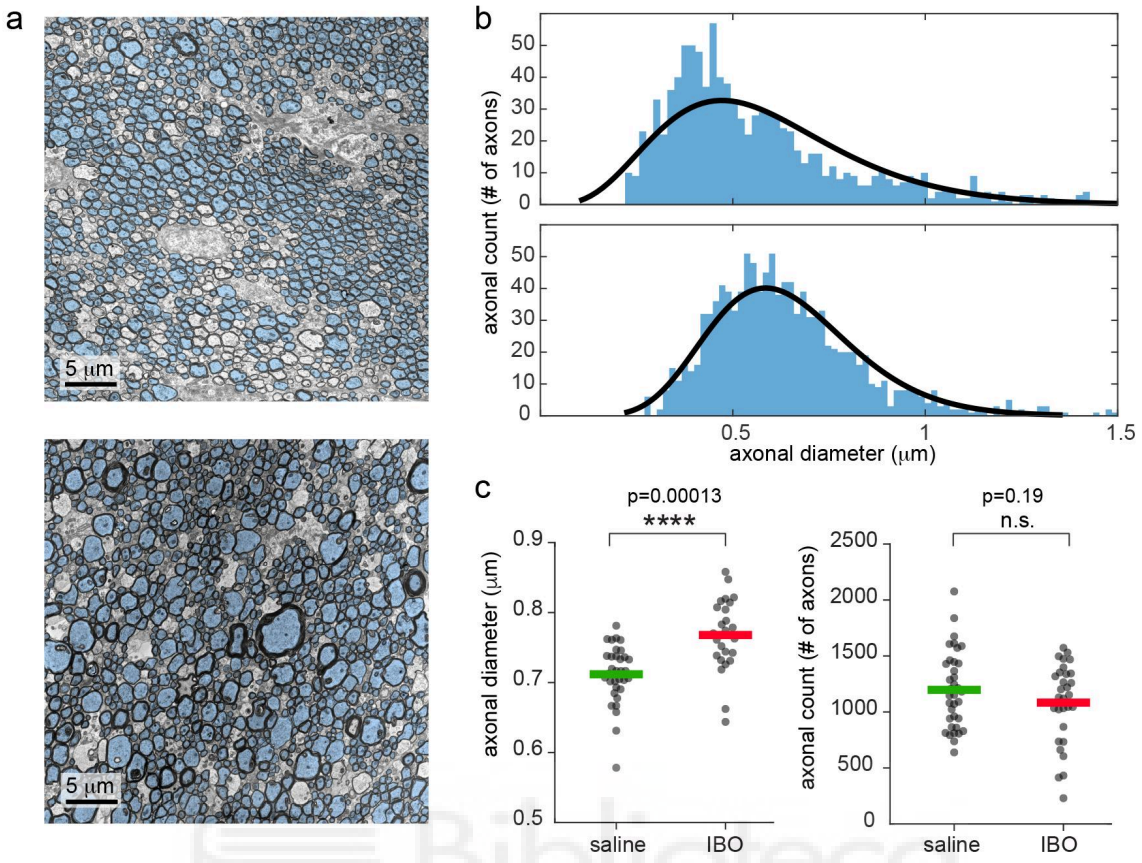

Figure 3.8. Electron microscopy shows increased mean axonal diameter in ibotenic-injected hemisphere compared to saline. a. Representative STEM photos for saline and ibotenic acid fimbriae. Segmented axons are overlaid in light blue. **b.** Histogram of the axonal count in one representative animal: upper line, saline injected, lower line, ibotenic. Black lines represent the gamma function better fitting the histogram. **c.** Mean axonal diameter (left) and count (right) in each photo and group. Asterisks represent significant unpaired t test differences between groups for axonal diameter (n=6, p=0.00013). Source: Cerdán Cerdá et al. (2024).

The dw-MRI axonal-diameter proxy increased in the damaged tract, correlating with neurofilament intensity (see Cerdán Cerdá, et al., 2024) and reflecting genuine morphological dilation rather than selective attrition of small axons (see Figure 3.9).

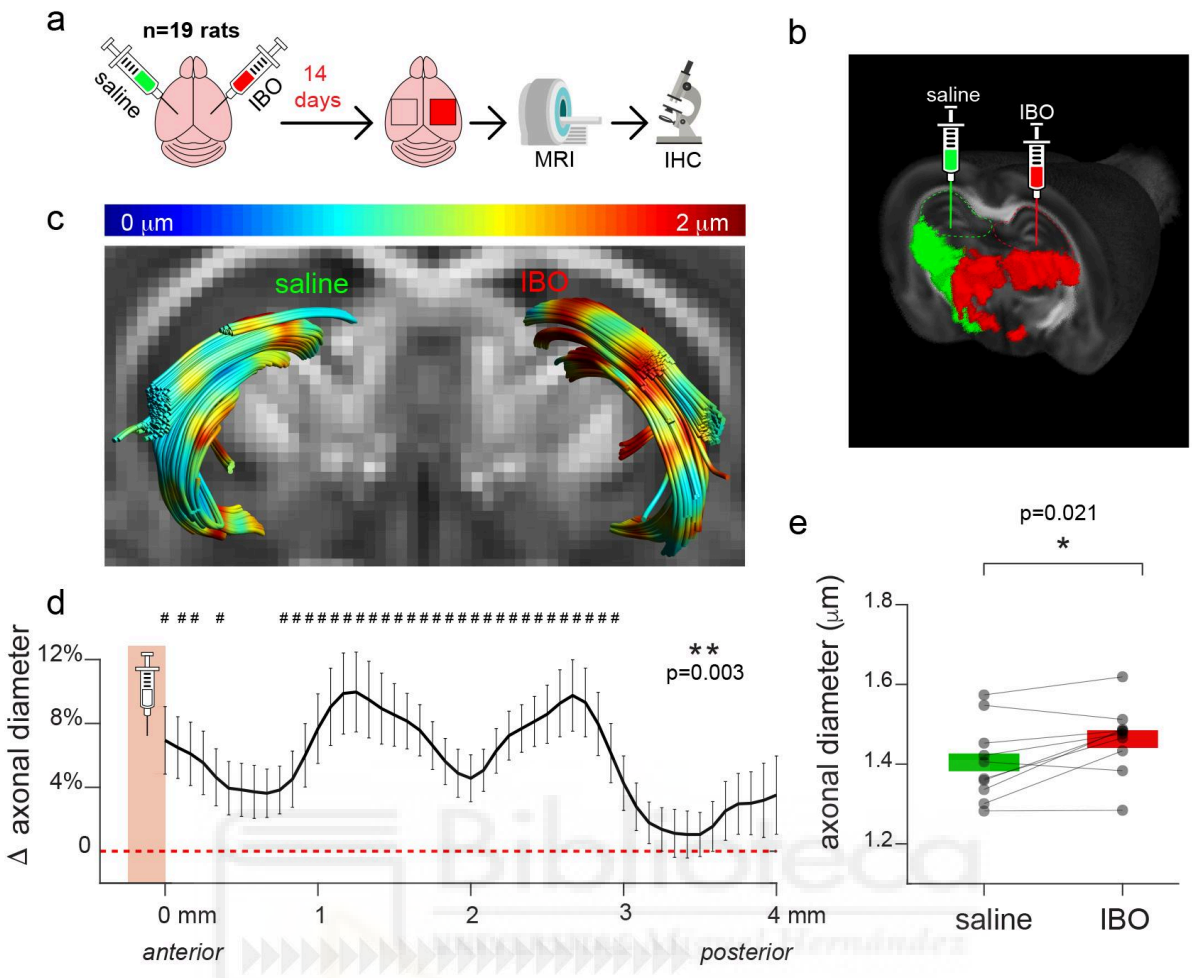

Figure 3.9. Experimental model of axonal damage. a. Experimental scheme of stereotaxic injections of ibotenic acid (IBO) in the left hippocampus of n=19 rats. The right hippocampus was injected with saline solution and used as a control. **b.** Visualization of the injection setup. **c.** Example of the tractography of the fimbriae from one representative animal, superimposed on the fractional anisotropy map. The MRI axonal diameter proxy is projected on the tract through color coding. **d.** Mean difference and standard deviation between groups of MRI axonal diameter proxy measured across all the streamlines constituting the fimbria in the antero-posterior axis, starting from the injection point (n=10). The injection site is shown in red. Asterisks represent significant group effect in the ANOVA, while hashtags represent significant post-hoc differences between groups in each location, corrected for multiple comparisons. **e.** Mean MRI axonal diameter proxy calculated in the ibotenic vs saline-injected fimbria reconstructed using tractography. Asterisks represent significant

differences (n=10, paired t test across hemispheres, p=0.021). Source: Cerdán Cerdá et al. (2024).

Axonal damage in normal-appearing white matter of multiple sclerosis patients

Building on these preclinical insights, we implemented a standardized acquisition and analysis pipeline in humans to interrogate axonal microstructure in MS. Across the NAWM, MS patients exhibited a diffuse increase in the MRI-derived axonal diameter proxy relative to healthy controls, with effects consistently observed across major commissural and projection pathways, including the corpus callosum, corticospinal tract, and internal capsule (see Figure 3.10). This pattern indicates that axonal pathology in MS is not confined to overt lesions but involves widespread microstructural alterations in tissue appearing normal on conventional imaging.

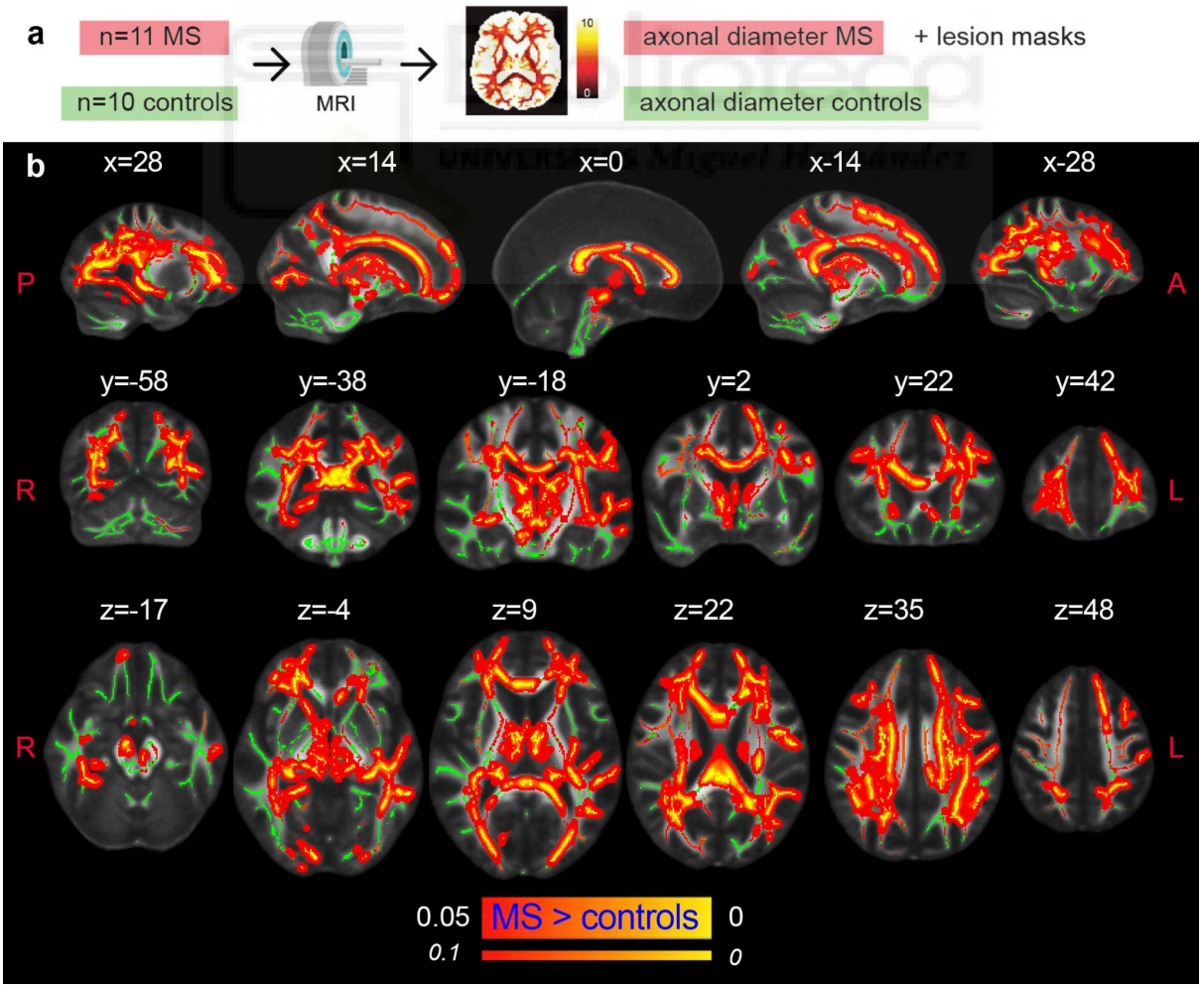

Figure 3.10. Axonal damage in MS normal-appearing white matter. a. Experimental scheme. **b.** Tract-based spatial statistics showing voxels in which the mean MRI axonal diameter proxy is significantly increased in multiple sclerosis versus healthy conditions (n=21, $p<0.05$, corrected). The opposite contrast was not statistically significant. Green: skeletonized white matter. Inflated red-yellow (through the pipeline tbss_fill): significant p value. Redyellow: p-value <0.1. Source: Cerdán Cerdá et al. (2024).

Axonal diameter is preferentially increased in patients with early disease

The temporal profile of these changes suggests an early phenomenon. Axonal diameter proxies showed a significant negative association with disease duration: patients within five years from diagnosis displayed the largest increases, whereas subjects with longer standing disease showed attenuated values (see Figure 3.11). This trajectory is compatible with a transient or partially reversible axonal enlargement phase—interpretable as acute axonal stress or swelling—followed by progressive axonal loss that reduces the aggregate caliber estimate over time. Notably, the axonal-diameter proxy did not correlate with global clinical scales, such as EDSS or SDMT, which may reflect limited statistical power, compensatory plasticity, and/or temporal decoupling between early microstructural changes and macroscopic functional readouts (see Cerdán Cerdá, et al., 2024).

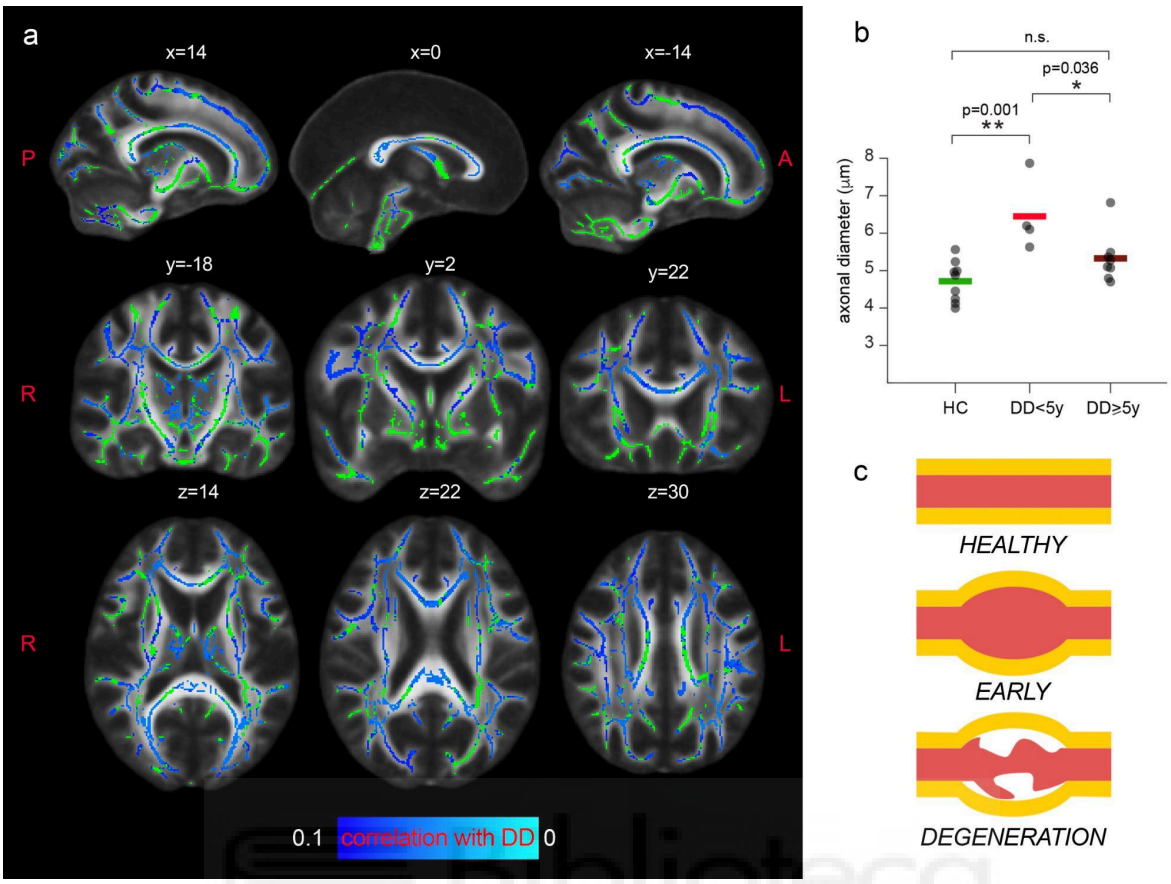

Figure 3.11. Axonal diameter is preferentially increased in patients with early MS. a. Tract-based spatial statistics showing voxels in which a trend of negative association between the MRI axonal diameter proxy and the disease duration (DD) in patients is present (n=11, p<0.1; lowest p-value = 0.051 corrected). Green: skeletonized white matter. Bluel-light blue: p value. **b.** Mean axonal diameter in the whole with matter of healthy controls (n=10, green), MS patients early in the disease course (n=4, <5 years, in red) and MS patients with a longer disease trajectory (n=7, ≥ 5 years, dark red). Asterisks represent unpaired post-hoc group differences following significant group effect in the ANOVA. **c.** Schematic progression of early axonal damage. Panel **c** has been adapted from Figure 1E from Luchicchi et al., 2021. Source: Cerdán Cerdá et al. (2024).

From a mechanistic standpoint, the imaging phenotype aligns with neuropathological observations that emphasize early axon–myelin unit disturbances in NAWM—such as varicosities, spheroids, and myelin blistering with partial axon–myelin detachment—which

can precede overt demyelination. Within this context, dw-MRI cannot, at present, disambiguate intra-axonal swelling from periaxonal space expansion; consequently, an elevated axonal-diameter proxy likely reflects a combination of both processes. Nevertheless, the consistent, tract-wide pattern, its prominence in early disease, and the concordance with preclinical axonal damage readouts support the interpretation of this metric as a sensitive marker of early axonal pathology in MS. Altogether, these findings extend the preclinical framework to humans, demonstrating that advanced diffusion-based mapping can detect subtle, diffuse axonal alterations in NAWM and potentially inform early monitoring and stratification strategies.

V. DISCUSSION

In this collection of studies, we have integrated experimental animal paradigms, histological analyses, and advanced diffusion MRI techniques to investigate neuroinflammation and neurodegeneration *in vivo*. By implementing neurotoxin-induced cell-specific challenges, we have established a framework for assessing microstructural changes occurring in neuroinflammatory and neurodegenerative pathologies. With this framework, we have demonstrated that MRI can differentiate between distinct microglial and astrocytic signatures in grey matter, providing a means to tailor specificity under defined pathological conditions. Additionally, our findings demonstrate the sensitivity of MRI to detect axonal swelling in white matter, a key feature of axonal pathology, and its potential as an early marker of MS in humans. In the following sections, we will discuss these findings in detail, addressing their implications, methodological considerations, and potential clinical applications.

Neurotoxin-validated biomarkers framework to assess neuroinflammatory and neurodegenerative pathologies via MRI

This study introduces a framework designed to induce controlled microglial and astrocytic reactivity *in vivo*. A key strength of this framework is the use of neurotoxin-based challenges, enabling precise isolation of cellular components relevant in pathology. By employing

neurotoxic agents such as lipopolysaccharide, ibotenic acid, and lysolecithin while focusing on relative changes between treated and control hemispheres, we induced controlled patterns of inflammation, neuronal loss, and demyelination. Comparing hemispheres within the same animal increase sensitivity to the induced alteration while minimizing other confounds.

Leveraging the distinct temporal profiles of glial activation, we isolated cell-specific morphological features. LPS-induced microglial reactivity was detectable within 8 hours as morphological alterations without proliferation. In contrast, astrocytic response followed a delayed trajectory, with significant hypertrophy occurring at 24 hours. By capitalizing on these differential time windows, we effectively isolated microglia reactivity. To isolate astrocyte reactivity, we pre-treated animals to achieve microglial depletion (via PLX5622). We demonstrated that we were still capable of achieving astrocytic reactivity 24 hours after LPS injection, but this time without microglia alterations. In addition to inflammation, the framework was applied to investigate neurodegenerative processes. Ibotenic acid-induced neuronal loss produced a reduction in hippocampal tissue alongside an increase of microglial proliferation and changes in its morphology, a condition that was used to study microglia proliferation. Moreover, modulating ibotenic acid-induced neurodegeneration with anti-inflammatory pretreatments revealed a potential utility in tracking dose-dependent microglia reactivity. To test potential signal confounds, we generate lysolecithin-induced myelin damage in a time window when inflammation is resolved. Leveraging the ibotenic acid-induced neuronal loss, we induced significant acute axonal damage in the fimbria, its main projection to prefrontal regions. This was supported by histological findings, including a pronounced reduction in NeuN staining in the hippocampus, indicative of neuronal loss, and an increase in neurofilament staining in the fimbria, suggesting axonal disruption. Furthermore, electron microscopy, comparing fimbria tracks from both hemispheres within the same animal, confirmed that the model achieved a significant enlargement of axonal caliber without significant axonal loss.

Isolating cell-specific contributions is key to developing a framework to challenge sensitivity and specificity of different alterations relevant in pathology, especially in the context of MRI signal. In fact, due to the contrast mechanism based on hydrogen atoms present in all cells in the tissue, and to the relatively large voxel size containing hundreds to thousands of cells (West et al., 1991), MRI signal is notoriously extremely sensitive to changes in cell compartments but also poorly specific.

As described in the introduction, considerable efforts have been devoted to developing microstructural models capable of capturing features specific to distinct tissue subcompartments for dw-MRI. Widely employed, their innovative approaches have been applied to characterize several pathological and non-pathological conditions. In the context of multicompartment diffusion models, comparing imaging findings with pathological evidence is essential to validate the underlying model assumptions. Such models rely on numerous simplifications, including fixed diffusivities (Alexander et al., 2010), lack of exchange between compartments (Lasič et al., 2011), and an indirect estimation of myelin volume (Assaf et al., 2008). However, direct connection between multicompartment diffusion models and biological substrate is either lacking or made using small sample sizes and based on correlations. For example, Ianuş et al. (2022) assessed the correspondence between SANDI fsphere parameter and the histological proxy of cell density based on the Allen Mouse Brain Atlas. A recent study introducing Neurite Exchange Imaging (NEXI), a minimal diffusion MRI model for gray matter that incorporates inter-compartment water exchange (Jelescu et al., 2022), performed histological validation by comparing the spatial patterns of anti-neurofilament immunostaining intensity—particularly in regions like the cortex and hippocampus—with the NEXI-derived neurite density parameter (f), showing that regions with higher or lower staining intensities matched variations in neurite density estimated from the diffusion MRI data. However, while promising this histological validation was conducted using a single fixed brain sample. Further validation is required to strengthen its biological interpretability. Specifically in white matter, challenges persist as researchers

strive to refine *in vivo* methods for studying bundle tract microstructure and pathophysiology. Building on the seminal work of Assaf et al. (2008), previous studies have reported correlations between axonal diameter measurements obtained via dw-MRI and axonal caliber estimations from electron microscopy in healthy tissue (Barazany et al., 2009; Assaf et al., 2013, 2019). However, similar to the limitations mentioned above, these studies relied on histological validation from a limited sample size, restricting their conclusions to naturally occurring variations in axonal diameter distribution. Consequently, they do not account for the morphological effects of pathological conditions on white matter structures, leaving gaps in our understanding of how disease processes alter axonal architecture.

We need to refer to applied specific pathology works to find attempts to directly relate MRI signal with the underlying pathological events. For example, Grussu et al. (2017) found the related NODDI ODI parameter as a marker of microstructural pathology, detecting trends of reduced geometrical complexity of neurite architecture within multiple sclerosis lesions. Specifically, ODI was sensitive and highly specific to histologically derived neurite orientation dispersion, using neurofilament staining, in the presence of multiple sclerosis-related pathology. Furthermore, those NODDI metrics turned out to be specific to neurons and were not influenced by features of the extra-neuronal space, such as density of glial cells. They also found NODDI neurite density index (NDI) sensitive to the local density of axon/dendrites but also strongly influenced by variations of myelination, limiting its interpretability without the support of myelin mapping techniques. Despite their informative value, these approaches face challenges as the precise temporal evolution of cellular processes underlying the inflammatory response remains unclear, particularly in both acute neurological events and chronic neuroinflammatory or neurodegenerative conditions. This raises critical questions regarding the extent to which individual cellular processes influence microstructural alterations detectable by dw-MRI. As demonstrated in previous research (Guglielmetti et al., 2016), the simultaneous occurrence of distinct cellular responses can attenuate the net diffusion signal alterations, thereby hampering the ability of dw-MRI to reliably detect

neuroinflammation and associated neurodegeneration. Furthermore, in cases where multiple cellular mechanisms interact, it remains unclear which process dominates and contributes most significantly to the measurable diffusion signal. By leveraging a combination of controlled tissue perturbations, we have systematically evaluated the sensitivity of MRI to cellular alterations associated with neurodegenerative, demyelinating, and inflammatory pathologies. Our framework integrates advanced multicompartment signal representations, specifically designed to disentangle glial reactivity, with a rigorous validation approach to ensure the specificity of signal interpretation. This methodological integration enhances the capacity of dw-MRI to provide a more precise characterization of the cellular and microstructural changes underlying neuroinflammation.

Despite its transformative potential, several methodological challenges remain. The framework is built to target morphological alterations associated with inflammatory states, such as process retraction, and thus does not fully capture the functional states of glial reactivity, which encompasses a spectrum of different phenotypes (Ransohoff, 2016). The integration of metabolomic or transcriptomic data could enhance the biological specificity of MRI-derived biomarkers. Additionally, validation in chronic or multifactorial disease models, such as those involving amyloid and tau pathology, is required to establish the generalizability of these findings. One critical challenge inherent in advanced imaging techniques is the heterogeneity of glial and axonal populations; factors such as age, sex, brain region, and disease stage influence cellular responses necessitating robust imaging metrics. Our approach, which focused on relative changes between treated and controlled hemispheres, mitigated these confounding variables and provided reproducible results. However, the impact of these factors will be investigated in the future, with the aim of refining the validation platform.

We have developed a framework that effectively disentangles glial activation from neurodegeneration and demyelination. In the context of dw-MRI model validation, this

approach represents a significant advancement in the field, providing platform where the sensitivity and specificity of the different models can be tested and compared.

Demonstrating that MRI Captures Distinct Microglial and Astrocytic Signatures

From the previous subsection, the need for a more rigorous validation of MRI-derived parameters with quantitative assays is evident. Our framework for generating cell-specific alterations was combined with MRI to show that advanced dw-MRI can reliably tease apart microglia versus astrocyte reactivity, as well as distinguish inflammatory responses from neurodegenerative or demyelinating processes. Key findings revealed that LPS-induced neuroinflammation led to a reduction in MRI-derived stick fraction (representing microglial processes) and an increase in small sphere radius (reflecting enlarged cell bodies), findings confirmed by Iba-1 histology. The specificity of these changes was validated through microglia depletion with PLX5622, which resulted in non-significant alterations in the microglia-specific MRI parameters. Similarly, astrocyte activation was characterized by delayed GFAP+ hypertrophy 24 hours post-LPS, corresponding to an increase in large sphere radius, an effect independent of microglial depletion. In the neurodegenerative paradigm, ibotenic acid-induced neuronal loss was accompanied by microglial proliferation, as reflected in MRI tissue fraction decreases. Notably, the small sphere fraction distinguished microglial proliferation from LPS-induced activation. Minocycline treatment mitigated neuronal loss, an effect reflected on the MRI changes in quantitative fashion. Meanwhile, in the demyelination model, lysolecithin-induced myelin degradation (indicated by myelin basic protein loss) did not interfere with glial MRI markers, though changes in the balance between water pools led to a decreased stick fraction. Finally, translation to human studies demonstrated high reproducibility, with MRI parameters such as stick fraction and dispersion correlating with postmortem microglial density patterns across brain regions.

Dw-MRI has demonstrated significant potential for elucidating the inflammatory components of various neurological conditions (De Santis & Canals, 2019). Early inflammatory

responses, characterized by microglial proliferation and astrogliosis, can lead to an isotropic reduction in apparent diffusivity and an increase in kurtosis, reflecting increased cellularity and tissue heterogeneity. For instance, following LPS administration in rodent experimental paradigms, authors reported an initial restriction of diffusion, marked by decreased diffusivity (Lodygensky et al., 2010) and increased kurtosis (Guan et al., 2021), which has been attributed to the proliferation and aggregation of microglia, astrocytes, and macrophages, as confirmed by histological analyses. In agreement with previous findings, our results indicate that conventional diffusion parameters, such as mean diffusivity, are sensitive to morphological changes induced by inflammation. Similarly, the cuprizone mouse experimental preparation, commonly used to study CNS demyelination, has provided insights into the temporal progression of DTI and DKI parameters during acute inflammatory demyelination and subsequent spontaneous remyelination. MD and RD have demonstrated being sensitive to acute and long-lasting changes during demyelination, while DKI offers greater sensitivity to detect morphological heterogeneity and demyelination in gray matter and less affected regions (Wang et al., 2011; Falangola et al., 2014; Guglielmetti et al., 2016; Jelescu et al., 2016).

Although these conventional empirical signal representations offer valuable insights, their primary limitation lies in their lack of specificity for differentiating distinct pathological mechanisms. Multiple physiological and pathological processes can induce similar alterations in apparent diffusivity. For example, reductions in mean diffusivity can result from microgliosis, malignant cell proliferation, or even normal brain development, where myelination and increased dendritic density contribute to comparable diffusion changes (De Santis et al., 2014; Marrale et al., 2016). Overcoming those limitations, our dw-MRI MCM was able to unravel the signal contribution from LPS-induced morphological microglial activation occurring in the absence of neuronal loss, enabling the identification of MRI signatures specific to microglial morphology, such as a reduced "stick fraction" reflecting process retraction. This aligns with previous research demonstrating that LPS triggers rapid

microglial reactivity, characterized by soma hypertrophy and loss of ramification (Kloss et al., 2001). Furthermore, the disappearance of microglial MRI signatures in depleted animals strongly supports the notion that these biomarkers reflect microglial morphology rather than nonspecific tissue alterations. This strategy parallels PET studies employing TSPO knockout models to validate radioligand specificity (Guilarte, 2019), but dw-MRI confers the advantage of higher spatial resolution, offering a more precise characterization of cellular changes.

By inducing neurodegenerative processes through the administration of ibotenic acid, we observed a reduction in tissue fraction, indicative of neuronal degeneration, coexisting with markers of microglial proliferation, such as an increased small sphere fraction. This dual signature addresses a critical gap in neurodegenerative disease research, where inflammation and neuronal loss frequently co-occur but are rarely distinguishable using conventional imaging techniques. In Alzheimer's disease, elevated mean diffusivity in the hippocampus is often interpreted as a marker of neuronal loss (Demey et al., 2015), yet the results of this study suggest that concurrent microglial activation may contribute to these signal alterations. Similarly, in Parkinson's disease, the ability to distinguish neuroinflammation from dopaminergic degeneration could facilitate more precise patient stratification for anti-inflammatory therapies (Q. Wang et al., 2015). Moreover, the ability to detect minocycline-mediated neuroprotection, as evidenced by preserved tissue fraction, echoes previous findings in Alzheimer's disease models where this compound prevents amyloid-induced neuronal death and reduced caspase-3 activation (Noble et al., 2009), suggesting potential clinical applications for monitoring treatment efficacy. By decoupling inflammation from degeneration, this approach resolves ambiguities inherent to conventional MRI metrics, such as mean diffusivity, which fails to distinguish between glial, neuronal, and vascular contributions (De Santis et al., 2014).

In the context of demyelination, lysolecithin-induced myelin damage provided additional insight into the framework's specificity. The study demonstrated that reductions in stick fraction were primarily driven by extracellular free water relative increases, a recognized

confounder in white matter imaging (Stikov et al., 2015). However, parameters such as stick dispersion remained specific to microglial morphology, illustrating the robustness of this approach in differentiating inflammatory from myelin-related alterations. This distinction is particularly relevant for diseases such as multiple sclerosis, where demyelination and inflammation often coexist and require distinct therapeutic strategies (Lassmann, 2018). By isolating glial responses, this framework could enable the identification of patients who are more likely to benefit from immunomodulatory interventions versus those requiring remyelination therapies.

Finally, the translation of this framework to human 3T MRI scanners marks a substantial step toward clinical applicability. The reproducibility of microglial biomarkers, with a coefficient of variation below 8%, is comparable to that of established MRI metrics used in clinical diagnostics (Veenith et al., 2013), while correlations with postmortem microglial density patterns (Mittelbronn et al., 2001) further reinforce their biological validity. These findings parallel to efforts to validate PET TSPO tracers against histological data (Guilarte, 2019) but offer a noninvasive alternative that circumvents the limitations of PET, such as radiation exposure and lower spatial resolution. This methodological approach refines the ability to disentangle overlapping pathological processes but also establishes a rigorous foundation for translating preclinical neuroimaging findings to human applications.

While this study provides valuable insights into glial dynamics, several methodological limitations must be acknowledged. The potential for mild inflammation from stereotaxic injections, the partial volume effects inherent to human imaging resolution, and the reliance on relative rather than absolute histological measures pose challenges to precise quantification. However, methodological refinements employed—such as within-subject controls, region erosion strategies, and advanced biophysical modeling—help mitigate these constraints. Despite these challenges, the findings demonstrate the robustness of this diffusion MRI approach in capturing glial dynamics. By bridging the gap between cellular and whole-brain imaging, this work advances the field of neuroimaging and establishes a

promising framework for studying neuroinflammation, neurodegeneration, and demyelination in both research and clinical applications.

MRI has sensitivity to capture the increase in axonal size due to axonal pathology

In the present study, we used a well-characterized rodent model in which the axonal compartment is selectively damaged. We detected increased neurofilament staining intensity in the damaged tract, demonstrating altered axonal morphology without alteration in the total amount of myelin. This change is picked up by MRI as an increase in the MRI axonal diameter proxy. Electron microscopy and axonal diameter quantification demonstrate that the increase observed in imaging reflects true morphological axonal alterations, hallmarks of axonal pathology. The significant correlation between neurofilament staining intensity and the MRI axonal diameter proxy further validates the imaging parameter as a marker of axonal damage and is compatible with recent work studying the association of MRI metrics sensitive to axonal pathology and the serum neurofilament light chain biomarker in humans (Rahmanzadeh et al., 2021). Importantly, this imaging-based observation was supported by histological findings, providing additional confirmation that the MRI-detected increase in axonal diameter corresponded to a true enlargement of axonal caliber.

Despite significant progress in non-invasive techniques for assessing brain microstructure, the accurate measurement of axonal size remains a subject of ongoing debate in neuroscience due to methodological limitations and biological complexities. Histological studies have long reported discrepancies in axonal size estimation, often attributed to the irregular, non-circular geometry of axons, which necessitates shape corrections for accurate normalization (Duvdevani et al., 1993). Recent advancements in imaging methodologies have provided key insights into axonal microstructure. For instance, ActiveAxADD has demonstrated the potential to extract non-parametric and orientationally invariant axon diameter distributions from isolated intra-axonal signals (Romascano et al., 2020). Similarly, Lee et al. (2020) validated the detection of micrometer-scale axonal variations, such as

axonal beading, using diffusion MRI in conjunction with Monte Carlo simulations of realistic axonal geometries derived from 3D electron microscopy. Further improvements in dw-MRI have been achieved by Veraart et al., (2020), who refined axonal radius estimation by addressing confounding factors such as extra-axonal water and orientation dispersion, thereby enhancing the validity of MRI-derived metrics against histological data.

Emerging approaches have sought to simplify axonal diameter estimation while maintaining accuracy. Harkins et al. (2021) introduced a methodology that leverages changes in radial apparent diffusion coefficients across effective diffusion times, eliminating the need for complex compartmental modeling. More recently, Pizzolato et al. (2023) proposed a general framework for estimating both axial and radial axonal diffusivities at strong diffusion weightings using kernel zonal modeling. Barakovic et al. (2023) integrated T1 and T2 relaxation times with spherical mean diffusion modeling, demonstrating improved sensitivity to smaller axons in the corpus callosum through the application of ultra-strong diffusion gradients. Additionally, Friesen et al. (2024) utilized oscillating gradient spin-echo sequences in high-field MRI systems (e.g., 7T and 15.2T) to model white matter microstructure, enhancing sensitivity to smaller axonal features by accounting for intra- and extra-axonal diffusion dynamics. Their voxel-based analyses captured microstructure heterogeneity more effectively than conventional region-based approaches. Notably, many of the aforementioned studies have yet to fully validate their imaging-derived measurements against underlying biological structures, or their sample sizes remain limited. These gaps underscore the need for further validation studies that integrate advanced imaging techniques with rigorous histological and ultrastructural analyses to enhance the reliability of axonal diameter estimation *in vivo*. In addition, none thus far have demonstrated that AxCaliber is sensitive to axonal damage, but only to naturally occurring caliber dispersion in healthy conditions.

Quantitative comparison between MRI maps and stained sections is severely hampered by the fixation process and other limitations (Horowitz, et al., 2015; Barakovic et al., 2023). A key contribution of this work lies in reconciling MRI and STEM measurements. While MRI

consistently overestimates axonal diameter due to its weighting toward larger axons, STEM underestimates diameters because of tissue shrinkage during fixation—a phenomenon quantified in our study as up to 39% shrinkage in STEM preparations. This discrepancy, consistent with Barakovic et al. (2023), highlights the challenges of histological validation but also emphasizes that both modalities detect the same underlying pathology: axonal swelling. Such swelling, rather than selective loss of small axons, appears to drive the MRI signal changes in our acute model, as supported by the strong correlation between neurofilament staining intensity and MRI-derived diameter proxies. This aligns with clinical studies linking MRI metrics to serum neurofilament light chain levels, a biomarker of neurodegeneration (Rahmanzadeh et al., 2021), underscoring the translational potential of MRI-based axonal mapping.

Like any methodological approach, this study has certain limitations that should be acknowledged. First, the chosen b-value (3000–4000 s/mm²) represented a compromise between sensitivity to small structures and achieving a sufficient signal-to-noise ratio (SNR) *in vivo*. While some studies question whether this value is too low to detect the intra-axonal signal (Veraart et al., 2020), our shrinkage analysis suggests that the current estimated sizes used to determine the minimum b-value required for axonal diameter measurement via MRI—such as those reported in De Santis et al. (2016)—should be updated. However, although this modest b-value is feasible for *in vivo* and clinical applications, it remains suboptimal for measuring axonal diameter. Higher b-values could enhance sensitivity to the intra-axonal compartment (Veraart et al., 2020; Barakovic et al., 2023). In this context, incorporating spherical mean techniques may improve axonal diameter and intra-axonal diffusivity estimations by accounting for fiber distribution effects and improving SNR (Dhital et al., 2019; Fan et al., 2020; Veraart et al., 2020). Additionally, in a subset of animals, we tested a protocol with a lower b-value and a simplified AxCaliber model (without diffusion time dependency) to facilitate future clinical AxCaliber studies. While we observed no qualitative differences in the outcome—MRI-based axonal diameter estimates increased

following fimbria damage—this result should be interpreted with caution. The predominance of extra-axonal signal may act as a confounding factor (Burcaw et al., 2015), highlighting the need for further research and potentially more realistic simulations that consider actual cellular composition and morphology.

Another limitation concerns the quantification of axonal diameter distribution, which was performed using a Poisson distribution. This approach, which relies on a single parameter to describe both the mean and dispersion, does not allow for differentiation between axonal swelling and the selective loss of small-caliber axons. Consequently, our current methodology does not permit us to ascertain whether the observed increase in axonal diameter is attributable to a preferential loss of small-caliber axons or axonal swelling. Future investigations incorporating a more comprehensive experimental protocol and a higher b-value—possibly using non-parametric estimates as proposed by Romascano et al. (2020)—could enable measurement of the full diameter distribution, offering more detailed insights into the underlying pathology.

Furthermore, the AxCaliber model used in this study does not account for fiber orientation dispersion in white matter. This simplification could introduce bias, particularly in regions where fibers are not uniformly aligned, potentially leading to inaccurate axonal diameter estimations. While some studies report modest values of dispersion in single-fiber areas (Mollink et al., 2017), others have measured values as high as 20 degrees (Ronen et al., 2014; Lee et al., 2019). Although it is reasonable to expect that some axonal directional dispersion in single-fiber regions is accounted for by the presence of a secondary fiber population—potentially mitigating the effect—future work should incorporate spherical mean techniques to fully eliminate this bias.

Finally, validation of the method was limited to a single white matter tract (the fimbria in rats). This raises concerns about its generalizability, as different brain regions or tracks may exhibit distinct structural properties that could influence the method’s reliability. However,

extrapolating our results to other tracts should be relatively straightforward. Future studies are needed to confirm this assumption.

Axonal swelling as a marker of early MS pathology

In this subsection, we present key findings that identify axonal swelling as a potential early marker in the pathogenesis of MS. Utilizing a standardized MRI protocol applied to both MS patients and healthy controls, our analysis revealed a diffuse increase in the MRI-derived axonal diameter proxy within the normal-appearing white matter of MS patients. This enlargement was consistently observed across several major white matter tracts, including the corpus callosum, corticospinal tract, and internal capsule. Notably, patients with a disease duration of less than five years exhibited a significantly greater axonal diameter proxy compared to both healthy controls and those with longer disease durations. These findings strongly suggest that axonal swelling is an early pathological event in MS, reinforcing the potential of MRI-based axonal diameter mapping as a sensitive biomarker for early disease detection and progression monitoring.

Axonal damage is a key driver of neurological decline in MS, and early transient axonal swelling may represent an initial structural adaptation to injury, with implications for long-term disability (Kuhlmann, 2002). Neuropathological studies have documented the formation of axonal varicosities and spheroids in the early stages of MS, leading to increased axonal diameters and impaired axonal transport (Criste et al., 2014). Both postmortem histological analyses (Bergers et al., 2002) and *in vivo* animal models (Nikić et al., 2011) provide evidence of axonal swelling occurring in both demyelinated and non-demyelinated regions. Additionally, smaller-caliber axons appear to be particularly vulnerable, potentially predisposing them to early degeneration in the disease process (Tallantyre et al., 2010). Recent studies further support the role of axonal swelling as a key biomarker in MS. Oost et al. (2023) reported that axonal loss in NAWM is frequently accompanied by compensatory swelling in surviving axons, often associated with adjustments in myelin thickness. This

structural adaptation, combined with mitochondrial dysfunction, may render swollen axons more susceptible to secondary injury. Similarly, Luchicchi et al. (2021) identified early morphological changes in NAWM, such as myelin blistering and detachment from axons, which disrupt axon-myelin interactions. These alterations, coupled with biochemical modifications—including increased protein citrullination—may further contribute to axonal dysfunction (Luchicchi et al., 2024). These post-mortem analyses show that the prevalence of these blisters is significantly higher in MS NAWM than in neurological and non-neurological controls, whereas the absolute number of simple axonal swellings does not differ between groups (Luchicchi et al., 2021). Consistent results are obtained in the non-inflammatory cuprizone mouse model, where myelin blisters appear within one week of intoxication—well before overt demyelination or extensive axonal enlargement (Joost et al., 2021) (Joost et al., 2022). Although illustrative, diffusion-MRI cannot presently discriminate between expansion of the axoplasm and enlargement of the periaxonal space, meaning that an elevated axonal-diameter proxy may reflect either axonal swelling, the presence of myelin blisters or both. Collectively, the above mentioned findings are consistent with our results, underscoring the relevance of axonal swelling as a biomarker of early, prelesional pathology in MS.

Beyond these morphological observations, it is important to place our findings within the broader etiopathogenic debate of MS. While an immune-centered, “outside–in” view posits that a primary dysregulation of the adaptive immune system targets CNS elements and drives demyelination, mounting clinicopathological evidence also supports an “inside–out” framework in which early oligodendroglial/axon–myelin unit disturbances precede—and possibly trigger—secondary autoimmune responses (Stys et al., 2012; ’t Hart et al., 2021). In particular, early abnormalities at the inner myelin lamellae, myelin–axon detachment (“blistering”), and the presence of post-translationally modified myelin (e.g., citrullinated epitopes) in NAWM have been proposed as candidate primary lesions capable of releasing antigenic debris and biasing immune recognition in predisposed hosts (Stys et al., 2012; ’t

Hart et al., 2021). Within this framework, diffuse axonal caliber enlargement detectable by MRI in NAWM may index early axon–myelin unit stress—whether intra-axonal swelling or periaxonal space expansion—occurring upstream of overt focal demyelination and before robust lymphocytic infiltration becomes apparent. These considerations do not exclude an immune contribution; rather, they reconcile our observations with a sequence in which early axon–myelin abnormalities can prime or amplify immune reactivity in susceptible individuals.

Building on these neuropathological findings, it is reasonable to expect that axonal damage in MS would manifest as an increase in axonal caliber detectable through MRI. Although a prior MRI study reported increased axonal diameter in MS (Huang et al., 2016), these findings were not validated. Furthermore, this previous work focused on the corpus callosum; our study demonstrates a diffuse increase in the MRI-derived axonal diameter proxy across all major white matter tracts in MS patients, indicating widespread axonal pathology in NAWM.

Notably, our analysis revealed a significant negative correlation between MRI-derived axonal diameter proxy and disease duration, suggesting that axonal swelling is an early event in MS pathogenesis. Patients with a disease duration of less than five years exhibited the most pronounced axonal swelling, whereas those with longer disease durations showed reduced axonal diameter proxies. This finding suggests that early axonal enlargement may be a transient or reversible phenomenon, potentially reflecting an initial response to injury. Furthermore, no other MRI parameters tested in our study were associated with disease duration, reinforcing the specificity of this finding. The observed reduction in axonal diameter over time likely reflects progressive axonal loss, supporting the hypothesis that an increased MRI-derived axonal diameter proxy is a marker of acute axonal damage.

Our results provide strong evidence of a significant increase in MRI-derived axonal diameter across major white matter tracts, including the corpus callosum and corticospinal tract, suggesting widespread axonal pathology in NAWM. These findings align with

neuropathological evidence indicating that early axonal damage in MS is characterized by transient swelling before progressing to degeneration.

Moreover, the negative correlation between MRI-derived axonal diameter and disease duration suggests that axonal swelling precedes overt demyelination and may serve as an initial response to injury. However, we found no significant associations between axonal diameter and clinical measures of disease severity, such as the Expanded Disability Status Scale (EDSS) or the Symbol Digit Modalities Test (SDMT). This absence of correlation may stem from several factors, including sample size limitations and compensatory mechanisms such as neuroplasticity and remyelination, which could mitigate the functional impact of early axonal pathology.

These observations underscore the potential of advanced MRI-based imaging techniques not only to confirm axonal swelling as an early marker of MS pathology but also to facilitate disease monitoring and guide therapeutic interventions aimed at controlling disease progression. Future studies should aim to refine multicompartment diffusion models by incorporating more biologically accurate assumptions and expanding validation efforts across larger and more diverse patient cohorts. By improving our ability to detect and monitor early axonal pathology, these imaging modalities may ultimately contribute to earlier diagnosis, better prognostication, and more targeted therapeutic strategies in MS.

VI. CONCLUSIONS

Both studies advance noninvasive MRI techniques to detect specific pathological processes—axonal damage and glial activation in neuroinflammation. These conclusions underscore the importance of validating imaging biomarkers against histopathology and their potential to transform early diagnosis and therapeutic monitoring into neurological disorders.

Diffusion MRI can noninvasively map and quantify neuroinflammatory processes, such as microglial and astrocyte activation, *in vivo*. This approach offers a translational tool for

studying neuroinflammation in neurodegenerative diseases (e.g., MS, Alzheimer's) and assessing anti-inflammatory therapies.

Key Findings:

1. A multi-compartment diffusion MRI model distinguished microglial and astrocyte reactivity in rodent experimental paradigms of neuroinflammation (LPS-induced), neurodegeneration (ibotenic acid-induced), and demyelination (lysolecithin-induced).
2. Histological validation (Iba1 for microglia, GFAP for astrocytes) confirmed MRI-detected changes in cellular morphology and density.
3. The MRI parameters (e.g., stick fraction, dispersion parameter *k*) differentiated between microglial ramification, neuronal loss, and demyelination, highlighting the specificity of the technique.

Axonal damage, detectable via noninvasive AxCaliber MRI, occurs early in MS and may drive disease progression. This method provides a sensitive biomarker for monitoring axonal pathology and evaluating therapies targeting neurodegeneration in MS.

Key Findings:

4. The AxCaliber MRI framework successfully detected acute axonal damage in a rat experimental paradigm of neurotoxin-induced axonal pathology. Histological (neurofilament staining) and electron microscopy validation confirmed increased axonal diameter as a marker of acute damage.
5. In humans with relapsing-remitting MS, AxCaliber revealed diffuse increases in axonal caliber within NAWM, particularly in patients with shorter disease duration. This suggests axonal swelling is an early pathological event in MS, preceding overt demyelination or axonal loss.
6. The MRI-derived axonal diameter proxy correlated with disease duration but did not show direct associations with clinical disability scores (e.g., EDSS), likely due to limited sample size or compensatory mechanisms.

VII. CONCLUSIONES

Ambos estudios avanzan en el desarrollo de técnicas no invasivas de imagen por resonancia magnética (IRM) para detectar procesos patológicos específicos, como el daño axonal y la activación glial en la neuroinflamación. Estas conclusiones subrayan la importancia de validar los biomarcadores de imagen con histopatología y su potencial para transformar el diagnóstico precoz y el monitoreo terapéutico en los trastornos neurológicos.

La RM por difusión puede mapear y cuantificar de forma no invasiva procesos neuroinflamatorios, como la activación de microglía y astrocitos, en sujetos vivos. Este enfoque ofrece una herramienta translacional para estudiar la neuroinflamación en enfermedades neurodegenerativas (por ejemplo, esclerosis múltiple y Alzheimer) y para evaluar terapias antiinflamatorias.

Hallazgos clave:

1. El modelo de RMI por difusión de múltiples compartimentos logró diferenciar la reactividad de microglía y astrocitos en paradigmas experimentales en roedores de neuroinflamación (inducida por LPS), neurodegeneración (inducida por ácido iboténico) y desmielinización (inducida por lisolectina).
2. La validación histológica (Iba1 para microglía y GFAP para astrocitos) confirmó los cambios detectados por RMI en la morfología y densidad celular.
3. Los parámetros obtenidos por RMI (por ejemplo, fracción de bastón, parámetro de dispersión k) permitieron diferenciar entre ramificación microglial, pérdida neuronal y desmielinización, lo que resalta la especificidad de la técnica.

El daño axonal, detectable mediante la técnica no invasiva AxCaliber MRI, ocurre en etapas tempranas de la esclerosis múltiple (EM) y puede impulsar la progresión de la enfermedad. Este método proporciona un biomarcador sensible para monitorear la patología axonal y evaluar terapias dirigidas a la neurodegeneración en EM.

Hallazgos clave:

4. El modelo AxCaliber MRI detectó exitosamente daño axonal agudo en un paradigma experimental con ratas basado en neurotoxinas. La validación con histología (tinción de neurofilamentos) y microscopía electrónica confirmó el aumento del diámetro axonal como un marcador de daño agudo.
5. En humanos con EM remitente-recurrente, AxCaliber reveló aumentos difusos en el calibre axonal dentro de la sustancia blanca aparentemente normal (NAWM), especialmente en pacientes con menor tiempo desde el diagnóstico. Esto sugiere que la hinchazón axonal es un evento patológico temprano en la EM, que precede a la desmielinización evidente o la pérdida axonal.
6. El parámetro de diámetro axonal derivado de la RM mostró correlación con la duración de la enfermedad, pero no se asoció directamente con las puntuaciones de discapacidad clínica (por ejemplo, EDSS), probablemente debido al tamaño limitado de la muestra o a mecanismos compensatorios.

VIII. REFERENCES

Abe, T., Sugihara, H., Nawa, H., Shigemoto, R., Mizuno, N., & Nakanishi, S. (1992). Molecular characterization of a novel metabotropic glutamate receptor mGluR5 coupled to inositol phosphate/Ca2+ signal transduction. *Journal of Biological Chemistry*, *267*(19), 13361–13368. https://doi.org/10.1016/S0021-9258(18)42219-3

Agosta, F., Galantucci, S., & Filippi, M. (2017). Advanced magnetic resonance imaging of neurodegenerative diseases. *Neurological Sciences*, *38*(1), 41–51. https://doi.org/10.1007/s10072-016-2764-x

Alexander, D. C., Dyrby, T. B., Nilsson, M., & Zhang, H. (2019). Imaging brain microstructure with diffusion MRI: Practicality and applications. *NMR in Biomedicine*, *32*(4), e3841. https://doi.org/10.1002/nbm.3841

Alexander, D. C., Hubbard, P. L., Hall, M. G., Moore, E. A., Ptito, M., Parker, G. J. M., & Dyrby, T. B. (2010). Orientationally invariant indices of axon diameter and density

from diffusion MRI. *NeuroImage*, *52*(4), 1374–1389. https://doi.org/10.1016/j.neuroimage.2010.05.043

Andersson, J. L. R., & Sotiropoulos, S. N. (2016). An integrated approach to correction for off-resonance effects and subject movement in diffusion MR imaging. *NeuroImage*, *125*, 1063–1078. https://doi.org/10.1016/j.neuroimage.2015.10.019

Assaf, Y., Alexander, D. C., Jones, D. K., Bizzi, A., Behrens, T. E. J., Clark, C. A., Cohen, Y., Dyrby, T. B., Huppi, P. S., Knoesche, T. R., LeBihan, D., Parker, G. J. M., & Poupon, C. (2013). The CONNECT project: Combining macro- and micro-structure. *NeuroImage*, *80*, 273–282. https://doi.org/10.1016/j.neuroimage.2013.05.055

Assaf, Y., & Basser, P. J. (2005). Composite hindered and restricted model of diffusion (CHARMED) MR imaging of the human brain. *NeuroImage*, *27*(1), 48–58. https://doi.org/10.1016/j.neuroimage.2005.03.042

Assaf, Y., Blumenfeld‐Katzir, T., Yovel, Y., & Basser, P. J. (2008). Axcaliber: A method for measuring axon diameter distribution from diffusion MRI. *Magnetic Resonance in Medicine*, *59*(6), 1347–1354. https://doi.org/10.1002/mrm.21577

Assaf, Y., Johansen-Berg, H., & Thiebaut de Schotten, M. (2019). The role of diffusion MRI in neuroscience. *NMR in Biomedicine*, *32*(4), e3762. https://doi.org/10.1002/nbm.3762

Atkinson, K. C., Lee, J. B., Hasselmann, J. P. C., Kim, S. H., Drew, A., Soto, J., Katzenellenbogen, J. A., Harris, N. G., Obenaus, A., & Tiwari-Woodruff, S. K. (2019). Diffusion tensor imaging identifies aspects of therapeutic estrogen receptor β ligand-induced remyelination in a mouse model of multiple sclerosis. *Neurobiology of Disease*, *130*, 104501. https://doi.org/10.1016/j.nbd.2019.104501

Avants, B. B., Tustison, N. J., Stauffer, M., Song, G., Wu, B., & Gee, J. C. (2014). The Insight ToolKit image registration framework. *Frontiers in Neuroinformatics*, *8*. https://doi.org/10.3389/fninf.2014.00044

Baijot, J., Van Laethem, D., Denissen, S., Costers, L., Cambron, M., D'Haeseleer, M., D'hooghe, M. B., Vanbinst, A.-M., De Mey, J., Nagels, G., & Van Schependom, J.

(2022). Radial diffusivity reflects general decline rather than specific cognitive deterioration in multiple sclerosis. *Scientific Reports*, *12*(1), 21771. https://doi.org/10.1038/s41598-022-26204-z

Bakshi, R., Ariyaratana, S., Benedict, R. H. B., & Jacobs, L. (2001). Fluid-Attenuated Inversion Recovery Magnetic Resonance Imaging Detects Cortical and Juxtacortical Multiple Sclerosis Lesions. *Archives of Neurology*, *58*(5), 742. https://doi.org/10.1001/archneur.58.5.742

Barakovic, M., Pizzolato, M., Tax, C. M. W., Rudrapatna, U., Magon, S., Dyrby, T. B., Granziera, C., Thiran, J.-P., Jones, D. K., & Canales-Rodríguez, E. J. (2023). Estimating axon radius using diffusion-relaxation MRI: Calibrating a surface-based relaxation model with histology. *Frontiers in Neuroscience*, *17*. https://doi.org/10.3389/fnins.2023.1209521

Barazany, D., Basser, P. J., & Assaf, Y. (2009). In vivo measurement of axon diameter distribution in the corpus callosum of rat brain. *Brain*, *132*(5), 1210–1220. https://doi.org/10.1093/brain/awp042

Barazany, D., Peter J. Basser, Basser, P. J., & Assaf, Y. (2009). In vivo measurement of axon diameter distribution in the corpus callosum of rat brain. *Brain*, *132*(5), 1210–1220. https://doi.org/10.1093/brain/awp042

Basser, P. J., Mattiello, J., & LeBihan, D. (1994). MR diffusion tensor spectroscopy and imaging. *Biophysical Journal*, *66*(1), 259–267. https://doi.org/10.1016/S0006-3495(94)80775-1

Basser, P. J., Pajevic, S., Pierpaoli, C., Duda, J., & Aldroubi, A. (2000). In vivo fiber tractography using DT-MRI data. *Magnetic Resonance in Medicine*, *44*(4), 625–632. https://doi.org/10.1002/1522-2594(200010)44:4<625::AID-MRM17>3.0.CO;2-O

Beard, J. R., Officer, A., de Carvalho, I. A., Sadana, R., Pot, A. M., Michel, J.-P., Lloyd-Sherlock, P., Epping-Jordan, J. E., Peeters, G. M. E. E. (Geeske), Mahanani, W. R., Thiyagarajan, J. A., & Chatterji, S. (2016). The World report on ageing and health: A policy framework for healthy ageing. *The Lancet*, *387*(10033), 2145–2154.

https://doi.org/10.1016/S0140-6736(15)00516-4

Beaulieu, C. (2002). The basis of anisotropic water diffusion in the nervous system—A technical review. *NMR in Biomedicine*, *15*(7–8), 435–455. https://doi.org/10.1002/nbm.782

Behrens, T. e. j., Woolrich, M. w., Jenkinson, M., Johansen-Berg, H., Nunes, R. g., Clare, S., Matthews, P. m., Brady, J. m., & Smith, S. m. (2003). Characterization and propagation of uncertainty in diffusion-weighted MR imaging. *Magnetic Resonance in Medicine*, *50*(5), 1077–1088. https://doi.org/10.1002/mrm.10609

Bergers, E., Bot, J. C. J., De Groot, C. J. A., Polman, C. H., Lycklama à Nijeholt, G. J., Castelijns, J. A., van der Valk, P., & Barkhof, F. (2002). Axonal damage in the spinal cord of MS patients occurs largely independent of T2 MRI lesions. *Neurology*, *59*(11), 1766–1771. https://doi.org/10.1212/01.WNL.0000036566.00866.26

Brites, D., & Fernandes, A. (2015). Neuroinflammation and Depression: Microglia Activation, Extracellular Microvesicles and microRNA Dysregulation. *Frontiers in Cellular Neuroscience*, *9*. https://doi.org/10.3389/fncel.2015.00476

Budde, M. D., Xie, M., Cross, A. H., & Song, S.-K. (2009). Axial Diffusivity Is the Primary Correlate of Axonal Injury in the Experimental Autoimmune Encephalomyelitis Spinal Cord: A Quantitative Pixelwise Analysis. *The Journal of Neuroscience*, *29*(9), 2805–2813. https://doi.org/10.1523/JNEUROSCI.4605-08.2009

Burcaw, L. M., Fieremans, E., & Novikov, D. S. (2015). Mesoscopic structure of neuronal tracts from time-dependent diffusion. *NeuroImage*, *114*, 18–37. https://doi.org/10.1016/j.neuroimage.2015.03.061

Chang, L., Jones, D. K., & Pierpaoli, C. (2005). RESTORE: Robust estimation of tensors by outlier rejection. *Magnetic Resonance in Medicine*, *53*(5), 1088–1095. https://doi.org/10.1002/mrm.20426

Chang, L., Munsaka, S., Kraft-Terry, S. D., & Ernst, T. (2013). Magnetic Resonance Spectroscopy to Assess NeuroInflammation and Neuropathic Pain. *Journal of Neuroimmune Pharmacology*, *8*, 576–593.

https://doi.org/10.1007/s11481-013-9460-x

Chao, C. C., Hu, S., Molitor, T. W., Shaskan, E. G., & Peterson, P. K. (1992). Activated microglia mediate neuronal cell injury via a nitric oxide mechanism. *Journal of Immunology (Baltimore, Md.: 1950)*, *149*(8), 2736–2741.

Cheng, S., Hou, J., Zhang, C., Xu, C., Wang, L., Zou, X., Yu, H., Shi, Y., Yin, Z., & Chen, G. (2015). Minocycline reduces neuroinflammation but does not ameliorate neuron loss in a mouse model of neurodegeneration. *Scientific Reports*, *5*(1), 10535. https://doi.org/10.1038/srep10535

Choi, D. W. (1988). Glutamate neurotoxicity and diseases of the nervous system. *Neuron*, *1*(8), 623–634. https://doi.org/10.1016/0896-6273(88)90162-6

Coleman, M. (2005). Axon degeneration mechanisms: Commonality amid diversity. *Nature Reviews Neuroscience*, *6*(11), 889–898. https://doi.org/10.1038/nrn1788

Compston, A., & Coles, A. (2008). Multiple sclerosis. *The Lancet*, *372*(9648), 1502–1517. https://doi.org/10.1016/S0140-6736(08)61620-7

Conforti, L., Gilley, J., & Coleman, M. P. (2014). Wallerian degeneration: An emerging axon death pathway linking injury and disease. *Nature Reviews Neuroscience*, *15*(6), 394–409. https://doi.org/10.1038/nrn3680

Court, F. A., & Coleman, M. P. (2012). Mitochondria as a central sensor for axonal degenerative stimuli. *Trends in Neurosciences*, *35*(6), 364–372. https://doi.org/10.1016/j.tins.2012.04.001

Criste, G., Trapp, B., & Dutta, R. (2014). Axonal loss in multiple sclerosis: Causes and mechanisms. *Handbook of Clinical Neurology*, *122*, 101–113. https://doi.org/10.1016/B978-0-444-52001-2.00005-4

De Santis, S., & Canals, S. (2019). Non-invasive MRI windows to neuroinflammation. *Neuroscience*, *403*, 1–3. https://doi.org/10.1016/j.neuroscience.2019.01.051

De Santis, S., Cosa-Linan, A., Garcia-Hernandez, R., Dmytrenko, L., Vargova, L., Vorisek, I., Stopponi, S., Bach, P., Kirsch, P., Kiefer, F., Ciccocioppo, R., Sykova, E., Moratal, D., Sommer, W. H., & Canals, S. (2020). Chronic alcohol consumption alters

extracellular space geometry and transmitter diffusion in the brain. *Science Advances*, *6*(26), eaba0154. https://doi.org/10.1126/sciadv.aba0154

De Santis, S., Drakesmith, M., Bells, S., Assaf, Y., & Jones, D. K. (2014). Why diffusion tensor MRI does well only some of the time: Variance and covariance of white matter tissue microstructure attributes in the living human brain. *NeuroImage*, *89*, 35–44. https://doi.org/10.1016/j.neuroimage.2013.12.003

De Santis, S., Granberg, T., Ouellette, R., Treaba, C. A., Herranz, E., Fan, Q., Mainero, C., & Toschi, N. (2019). Evidence of early microstructural white matter abnormalities in multiple sclerosis from multi-shell diffusion MRI. *NeuroImage: Clinical*, *22*, 101699. https://doi.org/10.1016/j.nicl.2019.101699

De Santis, S., Herranz, E., Treaba, C. A., Barletta, V., Mehndiratta, A., Mainero, C., & Toschi, N. (2019). Whole brain in vivo axonal diameter mapping in multiple sclerosis. *2019 41st Annual International Conference of the IEEE Engineering in Medicine and Biology Society (EMBC)*, 204–207. https://doi.org/10.1109/EMBC.2019.8856433

De Santis, S., Jones, D. K., & Roebroeck, A. (2016). Including diffusion time dependence in the extra-axonal space improves in vivo estimates of axonal diameter and density in human white matter. *NeuroImage*, *130*, 91–103. https://doi.org/10.1016/j.neuroimage.2016.01.047

Dell'Acqua, F., & Tournier, J. -Donald. (2019). Modelling white matter with spherical deconvolution: How and why? *Nmr in Biomedicine*, *32*(4), e3945. https://doi.org/10.1002/nbm.3945

Demey, I., Ventrice, F., Rojas, G., Ricardo, A., Somale, V.hippocamswelling, & Zubiri, V. (2015). P4-082: Hippocampal mean diffusivity is a biomarker of neuronal injury in patients with mild cognitive impairment and Alzheimer's disease dementia. *Alzheimer's & Dementia*, *11*(7S_Part_17), P802–P802. https://doi.org/10.1016/j.jalz.2015.06.1787

Desikan, R. S., Ségonne, F., Fischl, B., Quinn, B. T., Dickerson, B. C., Blacker, D., Buckner, R. L., Dale, A. M., Maguire, R. P., Hyman, B. T., Albert, M. S., & Killiany, R. J. (2006).

An automated labeling system for subdividing the human cerebral cortex on MRI scans into gyral based regions of interest. *NeuroImage*, *31*(3), 968–980. https://doi.org/10.1016/j.neuroimage.2006.01.021

Dhital, B., Reisert, M., Kellner, E., & Kiselev, V. G. (2019). Intra-axonal diffusivity in brain white matter. *NeuroImage*, *189*, 543–550. https://doi.org/10.1016/j.neuroimage.2019.01.015

Dong, Y., & Yong, V. (2019). When encephalitogenic T cells collaborate with microglia in multiple sclerosis. *Nature Reviews Neurology*, 1–14. https://doi.org/10.1038/s41582-019-0253-6

Drouin-Ouellet, J., Brownell, A.-L., Saint-Pierre, M., Fasano, C., Emond, V., Trudeau, L.-E., Lévesque, D., & Cicchetti, F. (2011). Neuroinflammation is associated with changes in glial mGluR5 expression and the development of neonatal excitotoxic lesions. *Glia*, *59*(2), 188–199. https://doi.org/10.1002/glia.21086

Duvdevani, R., Lavie, V., Sege, L., & Schwartz, M. (1993). A New Method for Expressing Axonal Size: Rat Optic Nerve Analysis. *Journal of Electron Microscopy*, *42*(6), 412–414. https://doi.org/10.1093/oxfordjournals.jmicro.a051062

Dyrby, T., Innocenti, G., Bech, M., & Lundell, H. (2018). Validation strategies for the interpretation of microstructure imaging using diffusion MRI. *NeuroImage*, *182*, 62–79. https://doi.org/10.1016/j.neuroimage.2018.06.049

Edwards, A. W. F. (2005). R.A. Fischer, statistical methods for research workers, first edition (1925). In *Landmark Writings in Western Mathematics 1640-1940* (pp. 856–870). Elsevier. https://doi.org/10.1016/B978-044450871-3/50148-0

Eed, A., Cerdán Cerdá, A., Lerma, J., & De Santis, S. (2020). Diffusion-weighted MRI in neurodegenerative and psychiatric animal models: Experimental strategies and main outcomes. *Journal of Neuroscience Methods*, *343*, 108814. https://doi.org/10.1016/j.jneumeth.2020.108814

Emsell, L., Van Hecke, W., & Tournier, J.-D. (2016). Introduction to Diffusion Tensor Imaging. In W. Van Hecke, L. Emsell, & S. Sunaert (Eds.), *Diffusion Tensor Imaging* (pp.

7–19). Springer New York. https://doi.org/10.1007/978-1-4939-3118-7_2

Espinosa-Oliva, A. M., de Pablos, R. M., & Herrera, A. J. (2013). Intracranial Injection of LPS in Rat as Animal Model of Neuroinflammation. In B. Joseph & J. L. Venero (Eds.), *Microglia: Methods and Protocols* (pp. 295–305). Humana Press. https://doi.org/10.1007/978-1-62703-520-0_26

Falangola, M. F., Guilfoyle, D. N., Tabesh, A., Hui, E. S., Nie, X., Jensen, J. H., Gerum, S. V., Hu, C., LaFrancois, J., Collins, H. R., & Helpern, J. A. (2014). Histological correlation of diffusional kurtosis and white matter modeling metrics in cuprizone‐induced corpus callosum demyelination. *NMR in Biomedicine*, *27*(8), 948–957. https://doi.org/10.1002/nbm.3140

Fan, Q., Nummenmaa, A., Witzel, T., Ohringer, N., Tian, Q., Setsompop, K., Klawiter, E. C., Rosen, B. R., Wald, L. L., & Huang, S. Y. (2020). Axon diameter index estimation independent of fiber orientation distribution using high-gradient diffusion MRI. *NeuroImage*, *222*, 117197. https://doi.org/10.1016/j.neuroimage.2020.117197

Feigin, V. L., Vos, T., Nichols, E., Owolabi, M. O., Carroll, W. M., Dichgans, M., Deuschl, G., Parmar, P., Brainin, M., & Murray, C. (2020). The global burden of neurological disorders: Translating evidence into policy. *The Lancet Neurology*, *19*(3), 255–265. https://doi.org/10.1016/S1474-4422(19)30411-9

Fieremans, E., Burcaw, L. M., Lee, H.-H., Lemberskiy, G., Veraart, J., & Novikov, D. S. (2016). *In vivo* observation and biophysical interpretation of time-dependent diffusion in human white matter. *NeuroImage*, *129*, 414–427. https://doi.org/10.1016/j.neuroimage.2016.01.018

Fieremans, E., Jensen, J. H., & Helpern, J. A. (2011). White matter characterization with diffusional kurtosis imaging. *NeuroImage*, *58*(1), 177–188. https://doi.org/10.1016/j.neuroimage.2011.06.006

Filippi, M., Preziosa, P., Banwell, B. L., Barkhof, F., Ciccarelli, O., De Stefano, N., Geurts, J. J. G., Paul, F., Reich, D. S., Toosy, A. T., Traboulsee, A., Wattjes, M. P., Yousry, T. A., Gass, A., Lubetzki, C., Weinshenker, B. G., & Rocca, M. A. (2019). Assessment of

lesions on magnetic resonance imaging in multiple sclerosis: Practical guidelines. *Brain*, *142*(7), 1858–1875. https://doi.org/10.1093/brain/awz144

Filippi, M., Rocca, M. A., Horsfield, M. A., Hametner, S., Geurts, J. J. G., Comi, G., & Lassmann, H. (2013). Imaging Cortical Damage and Dysfunction in Multiple Sclerosis. *JAMA Neurology*, *70*(5), 556–564. https://doi.org/10.1001/jamaneurol.2013.1954

Franceschi, C., Garagnani, P., Parini, P., Giuliani, C., & Santoro, A. (2018). Inflammaging: A new immune–metabolic viewpoint for age-related diseases. *Nature Reviews Endocrinology*, *14*(10), 576–590. https://doi.org/10.1038/s41574-018-0059-4

Franklin, R. J. M., & ffrench-Constant, C. (2008). Remyelination in the CNS: From biology to therapy. *Nature Reviews Neuroscience*, *9*(11), 839–855. https://doi.org/10.1038/nrn2480

Friedman, B. R. (Ed.). (1989). *Principles of MRI*. McGraw-Hill Information Services Co.

Friesen, E., Chisholm, M., Dhakal, B., Mercredi, M., Does, M. D., Gore, J. C., & Martin, M. (2024). Modelling white matter microstructure using diffusion OGSE MRI: Model and analysis choices. *Magnetic Resonance Imaging*, *113*, 110221. https://doi.org/10.1016/j.mri.2024.110221

Galea, I., Felton, L., Waters, S., Rooijen, N. van, Perry, H., & Newman, T. (2008). Immune-to-brain signalling: The role of cerebral CD163-positive macrophages. *Neuroscience Letters*, *448*, 41–46. https://doi.org/10.1016/j.neulet.2008.09.081

Garcia-Hernandez, R., Cerdán Cerdá, A., Trouve Carpena, A., Drakesmith, M., Koller, K., Jones, D. K., Canals, S., & De Santis, S. (2022). Mapping microglia and astrocyte activation in vivo using diffusion MRI. *Science Advances*, *8*(21), eabq2923. https://doi.org/10.1126/sciadv.abq2923

Garyfallidis, E., Brett, M., Amirbekian, B., Rokem, A., Van Der Walt, S., Descoteaux, M., & Nimmo-Smith, I. (2014). Dipy, a library for the analysis of diffusion MRI data. *Frontiers in Neuroinformatics*, *8*. https://www.frontiersin.org/articles/10.3389/fninf.2014.00008

Geiger, B. M., Frank, L. E., Caldera-Siu, A. D., & Pothos, E. N. (2008). Survivable Stereotaxic Surgery in Rodents. *Journal of Visualized Experiments (JoVE)*, *20*, e880. https://doi.org/10.3791/880

Giulian, D. (1993). Reactive glia as rivals in regulating neuronal survival. *Glia*, *7*(1), 102–110. https://doi.org/10.1002/glia.440070116

Glasser, M. F., Sotiropoulos, S. N., Wilson, J. A., Coalson, T. S., Fischl, B., Andersson, J. L., Xu, J., Jbabdi, S., Webster, M., Polimeni, J. R., Van Essen, D. C., & Jenkinson, M. (2013). The minimal preprocessing pipelines for the Human Connectome Project. *NeuroImage*, *80*, 105–124. https://doi.org/10.1016/j.neuroimage.2013.04.127

Goldschmidt, T., Antel, J., König, F. B., Brück, W., & Kuhlmann, T. (2009). Remyelination capacity of the MS brain decreases with disease chronicity. *Neurology*, *72*(22), 1914–1921. https://doi.org/10.1212/WNL.0b013e3181a8260a

Grover, V. P. B., Tognarelli, J. M., Crossey, M. M. E., Cox, I. J., Taylor-Robinson, S. D., & McPhail, M. J. W. (2015). Magnetic Resonance Imaging: Principles and Techniques: Lessons for Clinicians. *Journal of Clinical and Experimental Hepatology*, *5*(3), 246–255. https://doi.org/10.1016/j.jceh.2015.08.001

Grussu, F., Schneider, T., Tur, C., Yates, R. L., Tachrount, M., Ianuş, A., Yiannakas, M. C., Newcombe, J., Zhang, H., Alexander, D. C., DeLuca, G. C., & Gandini Wheeler-Kingshott, C. A. M. (2017). Neurite dispersion: A new marker of multiple sclerosis spinal cord pathology? *Annals of Clinical and Translational Neurology*, *4*(9), 663–679. https://doi.org/10.1002/acn3.445

Guan, X., Liu, S., Liang, M., Li, G., Dong, J., & Zhou, Q. (2021). Diffusion kurtosis imaging to evaluate the effect and mechanism of tetramethylpyrazine on cognitive impairment induced by lipopolysaccharide in rats. *Brain Imaging and Behavior*, *15*(5), 2492–2501. https://doi.org/10.1007/s11682-021-00449-0

Guglielmetti, C., Veraart, J., Roelant, E., Mai, Z., Daans, J., Van Audekerke, J., Naeyaert, M., Vanhoutte, G., Delgado Y Palacios, R., Praet, J., Fieremans, E., Ponsaerts, P., Sijbers, J., Van Der Linden, A., & Verhoye, M. (2016). Diffusion kurtosis imaging

probes cortical alterations and white matter pathology following cuprizone induced demyelination and spontaneous remyelination. *NeuroImage*, *125*, 363–377. https://doi.org/10.1016/j.neuroimage.2015.10.052

Guilarte, T. R. (2019). TSPO in diverse CNS pathologies and psychiatric disease: A critical review and a way forward. *Pharmacology & Therapeutics*, *194*, 44–58. https://doi.org/10.1016/j.pharmthera.2018.09.003

Haines, J. D., Inglese, M., & Casaccia, P. (2011). Axonal Damage in Multiple Sclerosis. *Mount Sinai Journal of Medicine: A Journal of Translational and Personalized Medicine*, *78*(2), 231–243. https://doi.org/10.1002/msj.20246

Han, J., Harris, R. A., & Zhang, X.-M. (2017). An updated assessment of microglia depletion: Current concepts and future directions. *Molecular Brain*, *10*(1), 25. https://doi.org/10.1186/s13041-017-0307-x

Harkins, K. D., Beaulieu, C., Xu, J., Gore, J. C., & Does, M. D. (2021). A simple estimate of axon size with diffusion MRI. *NeuroImage*, *227*, 117619. https://doi.org/10.1016/j.neuroimage.2020.117619

Harms, R. L., Fritz, F. J., Tobisch, A., Goebel, R., & Roebroeck, A. (2017). Robust and fast nonlinear optimization of diffusion MRI microstructure models. *NeuroImage*, *155*, 82–96. https://doi.org/10.1016/j.neuroimage.2017.04.064

Hennessy, E., Griffin, É., & Cunningham, C. (2015). Astrocytes Are Primed by Chronic Neurodegeneration to Produce Exaggerated Chemokine and Cell Infiltration Responses to Acute Stimulation with the Cytokines IL-1β and TNF-α. *The Journal of Neuroscience*, *35*, 8411–8422. https://doi.org/10.1523/JNEUROSCI.2745-14.2015

Herrera, A. J., Castaño, A., Venero, J. L., Cano, J., & Machado, A. (2000). The Single Intranigral Injection of LPS as a New Model for Studying the Selective Effects of Inflammatory Reactions on Dopaminergic System. *Neurobiology of Disease*, *7*(4), 429–447. https://doi.org/10.1006/nbdi.2000.0289

Horowitz, A., Barazany, D., Tavor, I., Bernstein, M., Yovel, G., & Assaf, Y. (2015). In vivo correlation between axon diameter and conduction velocity in the human brain. *Brain*

Structure and Function, *220*(3), 1777–1788. https://doi.org/10.1007/s00429-014-0871-0

Horowitz, A., Barazany, D., Tavor, I., Yovel, G., & Assaf, Y. (2015). Response to the comments on the paper by Horowitz et al. (2014). *Brain Structure and Function*, *220*(3), 1791–1792. https://doi.org/10.1007/s00429-015-1031-x

Huang, S. Y., Tobyne, S. M., Nummenmaa, A., Witzel, T., Wald, L. L., McNab, J. A., & Klawiter, E. C. (2016). Characterization of Axonal Disease in Patients with Multiple Sclerosis Using High-Gradient-Diffusion MR Imaging. *Radiology*, *280*(1), 244–251. https://doi.org/10.1148/radiol.2016151582

Ianuş, A., Carvalho, J., Fernandes, F. F., Cruz, R., Chavarrias, C., Palombo, M., & Shemesh, N. (2022). Soma and Neurite Density MRI (SANDI) of the in-vivo mouse brain and comparison with the Allen Brain Atlas. *NeuroImage*, *254*, 119135. https://doi.org/10.1016/j.neuroimage.2022.119135

Ifergan, I., Kebir, H., Alvarez, J. I., Marceau, G., Bernard, M., Bourbonnière, L., Poirier, J., Duquette, P., Talbot, P., Arbour, N., & Prat, A. (2011). Central nervous system recruitment of effector memory CD8+ T lymphocytes during neuroinflammation is dependent on α4 integrin. *Brain*, *134*, 3560–3577. https://doi.org/10.1093/brain/awr268

Jelescu, I. O., De Skowronski, A., Geffroy, F., Palombo, M., & Novikov, D. S. (2022). Neurite Exchange Imaging (NEXI): A minimal model of diffusion in gray matter with inter-compartment water exchange. *NeuroImage*, *256*, 119277. https://doi.org/10.1016/j.neuroimage.2022.119277

Jelescu, I. O., & Fieremans, E. (2023). Chapter 2—Sensitivity and specificity of diffusion MRI to neuroinflammatory processes. In C. Laule & J. D. Port (Eds.), *Advances in Magnetic Resonance Technology and Applications* (Vol. 9, pp. 31–50). Academic Press. https://doi.org/10.1016/B978-0-323-91771-1.00010-1

Jelescu, I. O., Zurek, M., Winters, K. V., Veraart, J., Rajaratnam, A., Kim, N. S., Babb, J. S., Shepherd, T. M., Novikov, D. S., Kim, S. G., & Fieremans, E. (2016). *In vivo*

quantification of demyelination and recovery using compartment-specific diffusion MRI metrics validated by electron microscopy. *NeuroImage*, *132*, 104–114. https://doi.org/10.1016/j.neuroimage.2016.02.004

Jenkinson, M., & Chappell, M. (2018). *Introduction to neuroimaging analysis*. Oxford university press.

Jeong, H.-K., Jou, I., & Joe, E. (2010). Systemic LPS administration induces brain inflammation but not dopaminergic neuronal death in the substantia nigra. *Experimental & Molecular Medicine*, *42*(12), 823–832. https://doi.org/10.3858/emm.2010.42.12.085

Johansen-Berg, H., & Behrens, T. E. J. (2009). *Diffusion MRI: From quantitative measurement to in-vivo neuroanatomy* (1st ed). Elsevier/Academic Press.

Johnson, H. L., Chen, Y., Jin, F., Hanson, L. M., Gamez, J. D., Pirko, I., & Johnson, A. J. (2012). CD8 T cell-initiated blood-brain barrier disruption is independent of neutrophil support. *Journal of Immunology (Baltimore, Md.: 1950)*, *189*(4), 1937–1945. https://doi.org/10.4049/jimmunol.1200658

Jones, D. K. (Ed.). (2011). *Diffusion MRI: Theory, methods, and applications*. Oxford Univ. Press.

Jones, D. K., Alexander, D. C., Bowtell, R., Cercignani, M., Dell'Acqua, F., McHugh, D. J., Miller, K. L., Palombo, M., Parker, G. J. M., Rudrapatna, U. S., & Tax, C. M. W. (2018). Microstructural imaging of the human brain with a 'super-scanner': 10 key advantages of ultra-strong gradients for diffusion MRI. *NeuroImage*, *182*, 8–38. https://doi.org/10.1016/j.neuroimage.2018.05.047

Jones, D. K., & Basser, P. J. (2004). "Squashing peanuts and smashing pumpkins": How noise distorts diffusion-weighted MR data. *Magnetic Resonance in Medicine*, *52*(5), 979–993. https://doi.org/10.1002/mrm.20283

Jones, D. K., Knösche, T. R., & Turner, R. (2013). White matter integrity, fiber count, and other fallacies: The do's and don'ts of diffusion MRI. *NeuroImage*, *73*, 239–254. https://doi.org/10.1016/j.neuroimage.2012.06.081

Jonkman, L., Kenkhuis, B., Geurts, J., & Berg, W. D. (2019). Post-Mortem MRI and Histopathology in Neurologic Disease: A Translational Approach. *Neuroscience Bulletin*, *35*, 229–243. https://doi.org/10.1007/s12264-019-00342-3

Just, M., & Thelen, M. (1988). Tissue characterization with T1, T2, and proton density values: Results in 160 patients with brain tumors. *Radiology*. https://doi.org/10.1148/radiology.169.3.3187000

Kamagata, K., Andica, C., Uchida, W., Takabayashi, K., Saito, Y., Lukies, M., Hagiwara, A., Fujita, S., Akashi, T., Wada, A., Hori, M., Kamiya, K., Zalesky, A., & Aoki, S. (2024). Advancements in Diffusion MRI Tractography for Neurosurgery. *Investigative Radiology*, *59*(1), 13. https://doi.org/10.1097/RLI.0000000000001015

Karussis, D. (2014). The diagnosis of multiple sclerosis and the various related demyelinating syndromes: A critical review. *Journal of Autoimmunity*, *48–49*, 134–142. https://doi.org/10.1016/j.jaut.2014.01.022

Kastler, B., & Anstett, P. (2011). *Comprendre l'IRM: Manuel d'auto-apprentissage* (7ème éd. entièrement rév). Elsevier Masson.

Kaur, D., Sharma, V., & Deshmukh, R. (2019). Activation of microglia and astrocytes: A roadway to neuroinflammation and Alzheimer's disease. *Inflammopharmacology*, *27*, 663–677. https://doi.org/10.1007/s10787-019-00580-x

Keil, B., Blau, J. N., Biber, S., Hoecht, P., Tountcheva, V., Setsompop, K., Triantafyllou, C., & Wald, L. L. (2013). A 64-channel 3T array coil for accelerated brain MRI. *Magnetic Resonance in Medicine*, *70*(1), 248–258. https://doi.org/10.1002/mrm.24427

Kellner, E., Dhital, B., Kiselev, V. G., & Reisert, M. (2016). Gibbs-ringing artifact removal based on local subvoxel-shifts. *Magnetic Resonance in Medicine*, *76*(5), 1574–1581. https://doi.org/10.1002/mrm.26054

Kiselev, V. G. (2021). Microstructure with diffusion MRI: What scale we are sensitive to? *Journal of Neuroscience Methods*, *347*, 108910. https://doi.org/10.1016/j.jneumeth.2020.108910

Klein, A., Andersson, J., Ardekani, B. A., Ashburner, J., Avants, B., Chiang, M.-C.,

Christensen, G. E., Collins, D. L., Gee, J., Hellier, P., Song, J. H., Jenkinson, M., Lepage, C., Rueckert, D., Thompson, P., Vercauteren, T., Woods, R. P., Mann, J. J., & Parsey, R. V. (2009). Evaluation of 14 nonlinear deformation algorithms applied to human brain MRI registration. *NeuroImage*, *46*(3), 786–802. https://doi.org/10.1016/j.neuroimage.2008.12.037

Kloss, C. U. A., Bohatschek, M., Kreutzberg, G. W., & Raivich, G. (2001). Effect of Lipopolysaccharide on the Morphology and Integrin Immunoreactivity of Ramified Microglia in the Mouse Brain and in Cell Culture. *Experimental Neurology*, *168*(1), 32–46. https://doi.org/10.1006/exnr.2000.7575

Knight, M. J., McCann, B., Tsivos, D., Couthard, E., & Kauppinen, R. (2016). Quantitative T1 and T2 MRI signal characteristics in the human brain: Different patterns of MR contrasts in normal ageing. *Magma (New York, N.y.)*, *29*, 833–842. https://doi.org/10.1007/s10334-016-0573-0

Kuhlmann, T. (2002). Acute axonal damage in multiple sclerosis is most extensive in early disease stages and decreases over time. *Brain*, *125*(10), 2202–2212. https://doi.org/10.1093/brain/awf235

Kurtzke, J. F. (1983). Rating neurologic impairment in multiple sclerosis: An expanded disability status scale (EDSS). *Neurology*, *33*(11), 1444–1444. https://doi.org/10.1212/WNL.33.11.1444

Lasič, S., Nilsson, M., Lätt, J., Ståhlberg, F., & Topgaard, D. (2011). Apparent exchange rate mapping with diffusion MRI. *Magnetic Resonance in Medicine*, *66*(2), 356–365. https://doi.org/10.1002/mrm.22782

Lassmann, H. (2018). Multiple Sclerosis Pathology. *Cold Spring Harbor Perspectives in Medicine*, *8*(3), a028936. https://doi.org/10.1101/cshperspect.a028936

Lassmann, H., & van Horssen, J. (2011). The molecular basis of neurodegeneration in multiple sclerosis. *FEBS Letters*, *585*(23), 3715–3723. https://doi.org/10.1016/j.febslet.2011.08.004

Lazari, A., & Lipp, I. (2020). Can MRI measure myelin? Systematic review, qualitative

assessment, and meta-analysis of studies validating microstructural imaging with myelin histology. *Neuroimage*, *230*. https://doi.org/10.1016/j.neuroimage.2021.117744

Le Bihan, D. (2003). Looking into the functional architecture of the brain with diffusion MRI. *Nature Reviews Neuroscience*, *4*(6), 469–480. https://doi.org/10.1038/nrn1119

Le Bihan, D., Breton, E., Lallemand, D., Grenier, P., Cabanis, E., & Laval-Jeantet, M. (1986). MR imaging of intravoxel incoherent motions: Application to diffusion and perfusion in neurologic disorders. *Radiology*, *161*(2), 401–407. https://doi.org/10.1148/radiology.161.2.3763909

Le Bihan, D., Mangin, J., Poupon, C., Clark, C. A., Pappata, S., Molko, N., & Chabriat, H. (2001). Diffusion tensor imaging: Concepts and applications. *Journal of Magnetic Resonance Imaging*, *13*(4), 534–546. https://doi.org/10.1002/jmri.1076

Le Bihan, D., Poupon, C., Amadon, A., & Lethimonnier, F. (2006). Artifacts and pitfalls in diffusion MRI. *Journal of Magnetic Resonance Imaging*, *24*(3), 478–488. https://doi.org/10.1002/jmri.20683

Lee, H.-H., Papaioannou, A., Kim, S.-L., Novikov, D. S., & Fieremans, E. (2020). A time-dependent diffusion MRI signature of axon caliber variations and beading. *Communications Biology*, *3*(1), 1–13. https://doi.org/10.1038/s42003-020-1050-x

Lee, H.-H., Yaros, K., Veraart, J., Pathan, J. L., Liang, F.-X., Kim, S. G., Novikov, D. S., & Fieremans, E. (2019). Along-axon diameter variation and axonal orientation dispersion revealed with 3D electron microscopy: Implications for quantifying brain white matter microstructure with histology and diffusion MRI. *Brain Structure and Function*, *224*(4), 1469–1488. https://doi.org/10.1007/s00429-019-01844-6

Leemans, A., Jeurissen, B., Sijbers, J., & Jones, D. K. (2009). *ExploreDTI: a graphicaltoolbox for processing, analyzing, and visualizing diffusion MR data*. *17*, 3537.

Leemans, A., & Jones, D. K. (2009). The B-matrix must be rotated when correcting for subject motion in DTI data. *Magnetic Resonance in Medicine*, *61*(6), 1336–1349.

https://doi.org/10.1002/mrm.21890

Ligneul, C., Palombo, M., Hernández-Garzón, E., Carrillo-de Sauvage, M.-A., Flament, J., Hantraye, P., Brouillet, E., Bonvento, G., Escartin, C., & Valette, J. (2019). Diffusion-weighted magnetic resonance spectroscopy enables cell-specific monitoring of astrocyte reactivity in vivo. *NeuroImage*, *191*, 457–469. https://doi.org/10.1016/j.neuroimage.2019.02.046

Lin, M. T., & Beal, M. F. (2006). Mitochondrial dysfunction and oxidative stress in neurodegenerative diseases. *Nature*, *443*(7113), 787–795. https://doi.org/10.1038/nature05292

Liu, L., Du, D., Zheng, T., Fang, Y., Chen, Y.-S., Yi, H., He, Q., Gao, D., & Shi, Q. (2017). Detecting dopaminergic neuronal degeneration using diffusion tensor imaging in a rotenone-induced rat model of Parkinson's disease: Fractional anisotropy and mean diffusivity values. *Neural Regeneration Research*, *12*, 1485–1491. https://doi.org/10.4103/1673-5374.213559

Lodygensky, G. A., West, T., Stump, M., Holtzman, D. M., Inder, T. E., & Neil, J. J. (2010). In vivo MRI analysis of an inflammatory injury in the developing brain. *Brain, Behavior, and Immunity*, *24*(5), 759–767. https://doi.org/10.1016/j.bbi.2009.11.005

Long, K. L. P., Chao, L. L., Kazama, Y., An, A., Hu, K. Y., Peretz, L., Muller, D. C. Y., Roan, V. D., Misra, R., Toth, C. E., Breton, J. M., Casazza, W., Mostafavi, S., Huber, B. R., Woodward, S. H., Neylan, T. C., & Kaufer, D. (2021). Regional gray matter oligodendrocyte- and myelin-related measures are associated with differential susceptibility to stress-induced behavior in rats and humans. *Translational Psychiatry*, *11*(1), 631. https://doi.org/10.1038/s41398-021-01745-5

Luchicchi, A., Hart, B., Frigerio, I., van Dam, A.-M., Perna, L., Offerhaus, H. L., Stys, P. K., Schenk, G. J., & Geurts, J. J. G. (2021). Axon-Myelin Unit Blistering as Early Event in MS Normal Appearing White Matter. *Annals of Neurology*, *89*(4), 711–725. https://doi.org/10.1002/ana.26014

Luchicchi, A., Muñoz‐Gonzalez, G., Halperin, S. T., Strijbis, E., Van Dijk, L. H. M., Foutiadou,

C., Uriac, F., Bouman, P. M., Schouten, M. A. N., Plemel, J., 'T Hart, B. A., Geurts, J. J. G., & Schenk, G. J. (2024). Micro-diffusely abnormal white matter: An early multiple sclerosis lesion phase with intensified myelin blistering. *Annals of Clinical and Translational Neurology*, *11*(4), 973–988. https://doi.org/10.1002/acn3.52015

Mahad, D. J., Ziabreva, I., Campbell, G., Lax, N., White, K., Hanson, P. S., Lassmann, H., & Turnbull, D. M. (2009). Mitochondrial changes within axons in multiple sclerosis. *Brain*, *132*(5), 1161–1174. https://doi.org/10.1093/brain/awp046

Mammana, S., Fagone, P., Cavalli, E., Basile, M., Petralia, M., Nicoletti, F., Bramanti, P., & Mazzon, E. (2018). The Role of Macrophages in Neuroinflammatory and Neurodegenerative Pathways of Alzheimer's Disease, Amyotrophic Lateral Sclerosis, and Multiple Sclerosis: Pathogenetic Cellular Effectors and Potential Therapeutic Targets. *International Journal of Molecular Sciences*, *19*. https://doi.org/10.3390/ijms19030831

Marrale, M., Collura, G., Brai, M., Toschi, N., Midiri, F., La Tona, G., Lo Casto, A., & Gagliardo, C. (2016). Physics, Techniques and Review of Neuroradiological Applications of Diffusion Kurtosis Imaging (DKI). *Clinical Neuroradiology*, *26*(4), 391–403. https://doi.org/10.1007/s00062-015-0469-9

Matousek, S. B., Ghosh, S., Shaftel, S. S., Kyrkanides, S., Olschowka, J. A., & O'Banion, M. K. (2012). Chronic IL-1β-Mediated Neuroinflammation Mitigates Amyloid Pathology in a Mouse Model of Alzheimer's Disease without Inducing Overt Neurodegeneration. *Journal of Neuroimmune Pharmacology*, *7*(1), 156–164. https://doi.org/10.1007/s11481-011-9331-2

Mittelbronn, M., Dietz, K., Schluesener, H. J., & Meyermann, R. (2001). Local distribution of microglia in the normal adult human central nervous system differs by up to one order of magnitude. *Acta Neuropathologica*, *101*(3), 249–255. https://doi.org/10.1007/s004010000284

Mollink, J., Kleinnijenhuis, M., Cappellen Van Walsum, A.-M. V., Sotiropoulos, S. N., Cottaar, M., Mirfin, C., Heinrich, M. P., Jenkinson, M., Pallebage-Gamarallage, M., Ansorge,

O., Jbabdi, S., & Miller, K. L. (2017). Evaluating fibre orientation dispersion in white matter: Comparison of diffusion MRI, histology and polarized light imaging. *NeuroImage*, *157*, 561–574. https://doi.org/10.1016/j.neuroimage.2017.06.001

Morawski, M., Kirilina, E., Scherf, N., Jäger, C., Reimann, K., Trampel, R., Gavriilidis, F., Geyer, S., Biedermann, B., Arendt, T., & Weiskopf, N. (2018). Developing 3D microscopy with CLARITY on human brain tissue: Towards a tool for informing and validating MRI-based histology. *NeuroImage*, *182*, 417–428. https://doi.org/10.1016/j.neuroimage.2017.11.060

Morris, R., Amaral, D. G., Bliss, T., Duff, K., & O'Keefe, J. (2024). *The Hippocampus Book*. Oxford University Press.

Nave, K.-A., & Trapp, B. D. (2008). Axon-glial signaling and the glial support of axon function. *Annual Review of Neuroscience*, *31*, 535–561. https://doi.org/10.1146/annurev.neuro.30.051606.094309

Niccoli, T., & Partridge, L. (2012). Ageing as a Risk Factor for Disease. *Current Biology*, *22*, 741–752. https://doi.org/10.1016/j.cub.2012.07.024

Nikić, I., Merkler, D., Sorbara, C., Brinkoetter, M., Kreutzfeldt, M., Bareyre, F. M., Brück, W., Bishop, D., Misgeld, T., & Kerschensteiner, M. (2011). A reversible form of axon damage in experimental autoimmune encephalomyelitis and multiple sclerosis. *Nature Medicine*, *17*(4), Article 4. https://doi.org/10.1038/nm.2324

Noble, W., Garwood, C., Stephenson, J., Kinsey, A. M., Hanger, D. P., & Anderton, B. H. (2009). Minocycline reduces the development of abnormal tau species in models of Alzheimer's disease. *The FASEB Journal*, *23*(3), 739–750. https://doi.org/10.1096/fj.08-113795

Noor, M. B. T., Zenia, N. Z., Kaiser, M. S., Mamun, S. A., & Mahmud, M. (2020). Application of deep learning in detecting neurological disorders from magnetic resonance images: A survey on the detection of Alzheimer's disease, Parkinson's disease and schizophrenia. *Brain Informatics*, *7*(1), 11. https://doi.org/10.1186/s40708-020-00112-2

Noristani, H. N., Boukhaddaoui, H., Saint-Martin, G., Auzer, P., Sidiboulenouar, R., Lonjon, N., Alibert, E., Tricaud, N., Goze-Bac, C., Coillot, C., & Perrin, F. E. (2017). A Combination of Ex vivo Diffusion MRI and Multiphoton to Study Microglia/Monocytes Alterations after Spinal Cord Injury. *Frontiers in Aging Neuroscience*, *9*. https://doi.org/10.3389/fnagi.2017.00230

Novikov, D. S., Fieremans, E., Jespersen, S. N., & Kiselev, V. G. (2019). Quantifying brain microstructure with diffusion MRI: Theory and parameter estimation. *NMR in Biomedicine*, *32*(4), e3998. https://doi.org/10.1002/nbm.3998

Oost, W., Huitema, A. J., Kats, K., Giepmans, B. N. G., Kooistra, S. M., Eggen, B. J. L., & Baron, W. (2023). Pathological ultrastructural alterations of myelinated axons in normal appearing white matter in progressive multiple sclerosis. *Acta Neuropathologica Communications*, *11*(1), 100. https://doi.org/10.1186/s40478-023-01598-7

Ou, Z., Sun, Y., Lin, L., You, N., Liu, X., Li, H., Ma, Y., Cao, L., Han, Y., Liu, M., Deng, Y., Yao, L., Lu, Q. R., & Chen, Y. (2016). Olig2-Targeted G-Protein-Coupled Receptor Gpr17 Regulates Oligodendrocyte Survival in Response to Lysolecithin-Induced Demyelination. *The Journal of Neuroscience*, *36*(41), 10560–10573. https://doi.org/10.1523/JNEUROSCI.0898-16.2016

Palombo, M., Ianus, A., Guerreri, M., Nunes, D., Alexander, D. C., Shemesh, N., & Zhang, H. (2020). SANDI: A compartment-based model for non-invasive apparent soma and neurite imaging by diffusion MRI. *NeuroImage*, *215*, 116835. https://doi.org/10.1016/j.neuroimage.2020.116835

Paxinos, G., & Franklin, K. B. J. (2019). *Paxinos and Franklin's The mouse brain in stereotaxic coordinates* (Fifth edition). Academic Press, an imprint of Elsevier.

Pizzolato, M., Canales-Rodríguez, E. J., Andersson, M., & Dyrby, T. B. (2023). Axial and radial axonal diffusivities and radii from single encoding strongly diffusion-weighted MRI. *Medical Image Analysis*, *86*, 102767. https://doi.org/10.1016/j.media.2023.102767

Polman, C. H., Reingold, S. C., Banwell, B., Clanet, M., Cohen, J. A., Filippi, M., Fujihara, K., Havrdova, E., Hutchinson, M., Kappos, L., Lublin, F. D., Montalban, X., O'Connor, P., Sandberg-Wollheim, M., Thompson, A. J., Waubant, E., Weinshenker, B., & Wolinsky, J. S. (2011). Diagnostic criteria for multiple sclerosis: 2010 Revisions to the McDonald criteria. *Annals of Neurology*, *69*(2), 292–302. https://doi.org/10.1002/ana.22366

Poynton, C., Jenkinson, M., Adalsteinsson, E., Sullivan, E., Pfefferbaum, A., & Wells, W. (2014). Quantitative Susceptibility Mapping by Inversion of a Perturbation Field Model: Correlation With Brain Iron in Normal Aging. *IEEE Transactions on Medical Imaging*, *34*, 339–353. https://doi.org/10.1109/TMI.2014.2358552

Preziosa, P., Kiljan, S., Steenwijk, M., Meani, A., Berg, W. V. D. van de, Schenk, G., Rocca, M., Filippi, M., Geurts, J., & Jonkman, L. (2019). Axonal degeneration as substrate of fractional anisotropy abnormalities in multiple sclerosis cortex. *Brain : A Journal of Neurology*. https://doi.org/10.1093/brain/awz143

Rahmanzadeh, R., Lu, P.-J., Barakovic, M., Weigel, M., Maggi, P., Nguyen, T. D., Schiavi, S., Daducci, A., La Rosa, F., Schaedelin, S., Absinta, M., Reich, D. S., Sati, P., Wang, Y., Bach Cuadra, M., Radue, E.-W., Kuhle, J., Kappos, L., & Granziera, C. (2021). Myelin and axon pathology in multiple sclerosis assessed by myelin water and multi-shell diffusion imaging. *Brain*, *144*(6), 1684–1696. https://doi.org/10.1093/brain/awab088

Ransohoff, R. M. (2016). A polarizing question: Do M1 and M2 microglia exist? *Nature Neuroscience*, *19*(8), 987–991. https://doi.org/10.1038/nn.4338

Ravanfar, P., Loi, S., Syeda, W., Rheenen, T. V. V., Bush, A., Desmond, P., Cropley, V., Lane, D., Opazo, C., Moffat, B., Velakoulis, D., & Pantelis, C. (2021). Systematic Review: Quantitative Susceptibility Mapping (QSM) of Brain Iron Profile in Neurodegenerative Diseases. *Frontiers in Neuroscience*, *15*. https://doi.org/10.3389/fnins.2021.618435

Rayleigh, Lord. (1903). On the Theory of Optical Images, with special reference to the Microscope. *Journal of the Royal Microscopical Society*, *23*(4), 474–482.

https://doi.org/10.1111/j.1365-2818.1903.tb04831.x

Rodieck, R. W. (1973). *The vertebrate retina: Principles of structure and function*. Freeman.

Romascano, D., Barakovic, M., Rafael-Patino, J., Dyrby, T. B., Thiran, J.-P., & Daducci, A. (2020). ActiveAxADD: Toward non-parametric and orientationally invariant axon diameter distribution mapping using PGSE. *Magnetic Resonance in Medicine*, *83*(6), 2322–2330. https://doi.org/10.1002/mrm.28053

Ronen, I., Budde, M., Ercan, E., Annese, J., Techawiboonwong, A., & Webb, A. (2014). Microstructural organization of axons in the human corpus callosum quantified by diffusion-weighted magnetic resonance spectroscopy of N-acetylaspartate and post-mortem histology. *Brain Structure and Function*, *219*(5), 1773–1785. https://doi.org/10.1007/s00429-013-0600-0

Rossi, S., Motta, C., Studer, V., Macchiarulo, G., Volpe, E., Barbieri, F., Ruocco, G., Buttari, F., Finardi, A., Mancino, R., Weiss, S., Battistini, L., Martino, G., Furlan, R., Drulovic, J., & Centonze, D. (2014). Interleukin-1β causes excitotoxic neurodegeneration and multiple sclerosis disease progression by activating the apoptotic protein p53. *Molecular Neurodegeneration*, *9*(1), 56. https://doi.org/10.1186/1750-1326-9-56

Schaefer, P. W., Grant, P. E., & Gonzalez, R. G. (2000). Diffusion-weighted MR Imaging of the Brain. *Radiology*, *217*(2), 331–345. https://doi.org/10.1148/radiology.217.2.r00nv24331

Schiffmann, R., & van der Knaap, M. S. (2009). Invited Article: An MRI-based approach to the diagnosis of white matter disorders. *Neurology*, *72*(8), 750–759. https://doi.org/10.1212/01.wnl.0000343049.00540.c8

Schmierer, K., Scaravilli, F., Altmann, D. R., Barker, G. J., & Miller, D. H. (2004). Magnetization transfer ratio and myelin in postmortem multiple sclerosis brain. *Annals of Neurology*, *56*(3), 407–415. https://doi.org/10.1002/ana.20202

Schmierer, K., Wheeler-Kingshott, C., Boulby, P., Scaravilli, F., Altmann, D., Barker, G., Tofts, P., & Miller, D. H. (2007). Diffusion tensor imaging of post mortem multiple sclerosis brain. *Neuroimage*, *35*, 467–477. https://doi.org/10.1016/j.neuroimage.2006.12.010

Selkoe, D. J., & Hardy, J. (2016). The amyloid hypothesis of Alzheimer's disease at 25 years. *EMBO Molecular Medicine*, *8*(6), 595–608. https://doi.org/10.15252/emmm.201606210

SheikhBahaei, S., Morris, B., Collina, J., Anjum, S., Znati, S., Gamarra, J., Zhang, R., Gourine, A. V., & Smith, J. C. (2018). Morphometric analysis of astrocytes in brainstem respiratory regions. *Journal of Comparative Neurology*, *526*(13), 2032–2047. https://doi.org/10.1002/cne.24472

Smith, A. (2016). *Symbol Digit Modalities Test* [Dataset]. https://doi.org/10.1037/t27513-000

Smith, S. M., Jenkinson, M., Johansen-Berg, H., Rueckert, D., Nichols, T. E., Mackay, C. E., Watkins, K. E., Ciccarelli, O., Cader, M. Z., Matthews, P. M., & Behrens, T. E. J. (2006). Tract-based spatial statistics: Voxelwise analysis of multi-subject diffusion data. *NeuroImage*, *31*(4), 1487–1505. https://doi.org/10.1016/j.neuroimage.2006.02.024

Spotorno, N., Strandberg, O., Stomrud, E., Janelidze, S., Blennow, K., Nilsson, M., van Westen, D., & Hansson, O. (2023). Diffusion MRI tracks cortical microstructural changes during the early stages of Alzheimer's disease. *Brain*, awad428. https://doi.org/10.1093/brain/awad428

Spotorno, N., Strandberg, O., Vis, G., Stomrud, E., Nilsson, M., & Hansson, O. (2023). Measures of cortical microstructure are linked to amyloid pathology in Alzheimer's disease. *Brain*, *146*(4), 1602–1614. https://doi.org/10.1093/brain/awac343

Steinmetz, J. D., Seeher, K. M., Schiess, N., Nichols, E., Cao, B., Servili, C., Cavallera, V., Cousin, E., Hagins, H., Moberg, M. E., Mehlman, M. L., Abate, Y. H., Abbas, J., Abbasi, M. A., Abbasian, M., Abbastabar, H., Abdelmasseh, M., Abdollahi, M., Abdollahi, M., … Dua, T. (2024). Global, regional, and national burden of disorders affecting the nervous system, 1990–2021: A systematic analysis for the Global Burden of Disease Study 2021. *The Lancet Neurology*, *23*(4), 344–381. https://doi.org/10.1016/S1474-4422(24)00038-3

Stejskal, E. O., & Tanner, J. E. (1965). Spin Diffusion Measurements: Spin Echoes in the

Presence of a Time-Dependent Field Gradient. *The Journal of Chemical Physics*, *42*(1), 288–292. https://doi.org/10.1063/1.1695690

Stern, C. (2008). *Principles of Functional Magnetic Resonance Imaging and its Applications in Cognitive Neuroscience*. https://www.semanticscholar.org/paper/Principles-of-Functional-Magnetic-Resonance-Imaging-Stern/93a1ba855bc3b19803b50785e6ff64124d7f28ca

Stevenson, V. L., Parker, G. J. M., Barker, G. J., Birnie, K., Tofts, P. S., Miller, D. H., & Thompson, A. J. (2000). Variations in T1 and T2 relaxation times of normal appearing white matter and lesions in multiple sclerosis. *Journal of the Neurological Sciences*, *178*(2), 81–87. https://doi.org/10.1016/S0022-510X(00)00339-7

Stikov, N., Campbell, J. S. W., Stroh, T., Lavelée, M., Frey, S., Novek, J., Nuara, S., Ho, M.-K., Bedell, B. J., Dougherty, R. F., Leppert, I. R., Boudreau, M., Narayanan, S., Duval, T., Cohen-Adad, J., Picard, P.-A., Gasecka, A., Côté, D., & Pike, G. B. (2015). In vivo histology of the myelin g-ratio with magnetic resonance imaging. *NeuroImage*, *118*, 397–405. https://doi.org/10.1016/j.neuroimage.2015.05.023

Strimbu, K., & Tavel, J. A. (2010). What are biomarkers? *Current Opinion in HIV and AIDS*, *5*(6), 463. https://doi.org/10.1097/COH.0b013e32833ed177

Subhramanyam, C. S., Wang, C., Hu, Q., & Dheen, S. T. (2019). Microglia-mediated neuroinflammation in neurodegenerative diseases. *Seminars in Cell & Developmental Biology*, *94*, 112–120. https://doi.org/10.1016/j.semcdb.2019.05.004

Tahedl, M. (2020). Towards individualized cortical thickness assessment for clinical routine. *Journal of Translational Medicine*, *18*(1), 151. https://doi.org/10.1186/s12967-020-02317-9

Tallantyre, E. C., Bo, L., Al-Rawashdeh, O., Owens, T., Polman, C. H., Lowe, J., & Evangelou, N. (2009). Greater loss of axons in primary progressive multiple sclerosis plaques compared to secondary progressive disease. *Brain*, *132*(5), 1190–1199. https://doi.org/10.1093/brain/awp106

Tallantyre, E. C., Bø, L., Al-Rawashdeh, O., Owens, T., Polman, C. H., Lowe, J. S., &

Evangelou, N. (2010). Clinico-pathological evidence that axonal loss underlies disability in progressive multiple sclerosis. *Multiple Sclerosis Journal*, *16*(4), 406–411. https://doi.org/10.1177/1352458510364992

Taquet, M., Jankovski, A., Rensonnet, G., Jacobs, D., Rieux, A. des, Macq, B., Warfield, S., & Scherrer, B. (2019). Extra-axonal restricted diffusion as an in-vivo marker of reactive microglia. *Scientific Reports*, *9*. https://doi.org/10.1038/s41598-019-50432-5

Traboulsee, A., Zhao, G., & Li, D. K. B. (2005). Neuroimaging in multiple sclerosis. *Neurologic Clinics*, *23*(1), 131–148. https://doi.org/10.1016/j.ncl.2004.10.001

Trapp, B. D., & Nave, K.-A. (2008). Multiple sclerosis: An immune or neurodegenerative disorder? *Annual Review of Neuroscience*, *31*, 247–269. https://doi.org/10.1146/annurev.neuro.30.051606.094313

Tsolaki, E., Kashanian, A., Chiu, K., Bari, A., & Pouratian, N. (2024). Connectivity-based segmentation of the thalamic motor region for deep brain stimulation in essential tremor: A comparison of deterministic and probabilistic tractography. *NeuroImage : Clinical*, *41*, 103587. https://doi.org/10.1016/j.nicl.2024.103587

van der Kouwe, A. J. W., Benner, T., Salat, D. H., & Fischl, B. (2008). Brain morphometry with multiecho MPRAGE. *NeuroImage*, *40*(2), 559–569. https://doi.org/10.1016/j.neuroimage.2007.12.025

Vangelderen, P., Despres, D., Vanzijl, P. C. M., & Moonen, C. T. W. (1994). Evaluation of Restricted Diffusion in Cylinders. Phosphocreatine in Rabbit Leg Muscle. *Journal of Magnetic Resonance, Series B*, *103*(3), 255–260. https://doi.org/10.1006/jmrb.1994.1038

Veenith, T. V., Carter, E., Grossac, J., Newcombe, V. F. J., Outtrim, J. G., Lupson, V., Williams, G. B., Menon, D. K., & Coles, J. P. (2013). Inter Subject Variability and Reproducibility of Diffusion Tensor Imaging within and between Different Imaging Sessions. *PLOS ONE*, *8*(6), e65941. https://doi.org/10.1371/journal.pone.0065941

Veraart, J., Nunes, D., Rudrapatna, U., Fieremans, E., Jones, D. K., Novikov, D. S., & Shemesh, N. (2020). Noninvasive quantification of axon radii using diffusion MRI.

eLife, *9*, e49855. https://doi.org/10.7554/eLife.49855

Veroni, C., Serafini, B., Rosicarelli, B., Fagnani, C., Aloisi, F., & Agresti, C. (2020). Connecting Immune Cell Infiltration to the Multitasking Microglia Response and TNF Receptor 2 Induction in the Multiple Sclerosis Brain. *Frontiers in Cellular Neuroscience*, *14*. https://doi.org/10.3389/fncel.2020.00190

Vos, S. B., Tax, C. M. W., Luijten, P. R., Ourselin, S., Leemans, A., & Froeling, M. (2017). The importance of correcting for signal drift in diffusion MRI. *Magnetic Resonance in Medicine*, *77*(1), 285–299. https://doi.org/10.1002/mrm.26124

Walderveen, M. V., Kamphorst, W., Scheltens, P., Waesberghe, J. V., Ravid, R., Valk, J., Polman, C., & Barkhof, F. (1998). Histopathologic correlate of hypointense lesions on T1-weighted spin-echo MRI in multiple sclerosis. *Neurology*, *50*, 1282–1288. https://doi.org/10.1212/WNL.50.5.1282

Waller, A. V. (1850). XX. Experiments on the section of the glossopharyngeal and hypoglossal nerves of the frog, and observations of the alterations produced thereby in the structure of their primitive fibres. *Philosophical Transactions of the Royal Society of London*, *140*, 423–429. https://doi.org/10.1098/rstl.1850.0021

Wang, Q., Liu, Y., & Zhou, J. (2015). Neuroinflammation in Parkinson's disease and its potential as therapeutic target. *Translational Neurodegeneration*, *4*(1), 19. https://doi.org/10.1186/s40035-015-0042-0

Wang, W.-Y., Tan, M., Yu, J.-T., & Tan, L. (2015). Role of pro-inflammatory cytokines released from microglia in Alzheimer's disease. *Annals of Translational Medicine*, *3 10*. https://doi.org/10.3978/j.issn.2305-5839.2015.03.49

Wang, Y., Wang, Q., Haldar, J. P., Yeh, F.-C., Xie, M., Sun, P., Tu, T.-W., Trinkaus, K., Klein, R. S., Cross, A. H., & Song, S.-K. (2011). Quantification of increased cellularity during inflammatory demyelination. *Brain*, *134*(12), 3590–3601. https://doi.org/10.1093/brain/awr307

West, M. J., Slomianka, L., & Gundersen, H. J. G. (1991). Unbiased stereological estimation of the total number of neurons in the subdivisions of the rat hippocampus using the

optical fractionator. *The Anatomical Record*, *231*(4), 482–497. https://doi.org/10.1002/ar.1092310411

Weston, P. S. J., Poole, T., Nicholas, J. M., Toussaint, N., Simpson, I. J. A., Modat, M., Ryan, N. S., Liang, Y., Rossor, M. N., Schott, J. M., Ourselin, S., Zhang, H., & Fox, N. C. (2020). Measuring cortical mean diffusivity to assess early microstructural cortical change in presymptomatic familial Alzheimer's disease. *Alzheimer's Research & Therapy*, *12*(1), 112. https://doi.org/10.1186/s13195-020-00679-2

Winkler, A. M., Ridgway, G. R., Webster, M. A., Smith, S. M., & Nichols, T. E. (2014). Permutation inference for the general linear model. *NeuroImage*, *92*, 381–397. https://doi.org/10.1016/j.neuroimage.2014.01.060

Winklewski, P. J., Sabisz, A., Naumczyk, P., Jodzio, K., Szurowska, E., & Szarmach, A. (2018). Understanding the Physiopathology Behind Axial and Radial Diffusivity Changes—What Do We Know? *Frontiers in Neurology*, *9*, 92. https://doi.org/10.3389/fneur.2018.00092

Wolbarst, A., & Yanasak, N. (2019). *An Introduction to MRI: For Medical Physicists and Engineers*. Medical Physics Publishing. https://doi.org/10.54947/9781930524200

Woodruff, R. H., & Franklin, R. J. M. (1999). Demyelination and remyelination of the caudal cerebellar peduncle of adult rats following stereotaxic injections of lysolecithin, ethidium bromide, and complement/anti-galactocerebroside: A comparative study. *Glia*, *25*(3), 216–228. https://doi.org/10.1002/(SICI)1098-1136(19990201)25:3<216::AID-GLIA2>3.0.CO;2-L

Yano, R., Hata, J., Abe, Y., Seki, F., Yoshida, K., Komaki, Y., Okano, H., & Tanaka, K. F. (2017). Quantitative temporal changes in DTI values coupled with histological properties in cuprizone-induced demyelination and remyelination. *Neurochemistry International*, *119*, 151–158. https://doi.org/10.1016/j.neuint.2017.10.004

Ye, L., Huang, Y., Zhao, L., Li, Y., Sun, L., Zhou, Y., Qian, G., & Zheng, J. C. (2013). IL-1β and TNF-α induce neurotoxicity through glutamate production: A potential role for neuronal glutaminase. *Journal of Neurochemistry*, *125*(6), 897–908.

https://doi.org/10.1111/jnc.12263

Yi, S. Y., Barnett, B. R., Torres-Velázquez, M., Zhang, Y., Hurley, S., Rowley, P. A., Hernando, D., & Yu, J.-P. J. (2019). Detecting Microglial Density With Quantitative Multi-Compartment Diffusion MRI. *Frontiers in Neuroscience*, *13*. https://doi.org/10.3389/fnins.2019.00081

Zanon Zotin, M. C., Yilmaz, P., Sveikata, L., Schoemaker, D., Van Veluw, S. J., Etherton, M. R., Charidimou, A., Greenberg, S. M., Duering, M., & Viswanathan, A. (2023). Peak Width of Skeletonized Mean Diffusivity: A Neuroimaging Marker for White Matter Injury. *Radiology*, *306*(3), e212780. https://doi.org/10.1148/radiol.212780

Zhang, H., Schneider, T., Wheeler-Kingshott, C. A., & Alexander, D. C. (2012a). NODDI: Practical in vivo neurite orientation dispersion and density imaging of the human brain. *NeuroImage*, *61*(4), 1000–1016. https://doi.org/10.1016/j.neuroimage.2012.03.072

Zhang, H., Schneider, T., Wheeler-Kingshott, C. A., & Alexander, D. C. (2012b). NODDI: Practical in vivo neurite orientation dispersion and density imaging of the human brain. *NeuroImage*, *61*(4), 1000–1016. https://doi.org/10.1016/j.neuroimage.2012.03.072

Zinkand, W. C., Moore, W. C., Thompson, C., Salama, A. I., & Patel, J. (1992). Ibotenic acid mediates neurotoxicity and phosphoinositide hydrolysis by independent receptor mechanisms. *Molecular and Chemical Neuropathology*, *16*(1), 1–10. https://doi.org/10.1007/BF03159956

IX. APPENDICES

Publication Serving as an Indicator of the Quality of This Work

RESEARCH ARTICLE

A translational MRI approach to validate acute axonal damage detection as an early event in multiple sclerosis

Antonio Cerdán Cerdá[1†], Nicola Toschi[2,3†], Constantina A Treaba[2], Valeria Barletta[2], Elena Herranz[2], Ambica Mehndiratta[2], Jose A Gomez-Sanchez[1,4,5], Caterina Mainero[2‡], Silvia De Santis[1*‡]

[1]Instituto de Neurociencias de Alicante, CSIC-UMH, San Juan de Alicante, Spain; [2]Athinoula A. Martinos Center for Biomedical Imaging, Department of Radiology, Massachusetts General Hospital, Harvard Medical School, Boston, United States; [3]Department of Biomedicine and Prevention, University of Rome Tor Vergata, Rome, Italy; [4]Instituto de Investigación Sanitaria y Biomédica de Alicante (ISABIAL), Alicante, Spain; [5]Millennium Nucleus for the Study of Pain (MiNuSPain), Santiago, Chile

Abstract Axonal degeneration is a central pathological feature of multiple sclerosis and is closely associated with irreversible clinical disability. Current noninvasive methods to detect axonal damage in vivo are limited in their specificity and clinical applicability, and by the lack of proper validation. We aimed to validate an MRI framework based on multicompartment modeling of the diffusion signal (AxCaliber) in rats in the presence of axonal pathology, achieved through injection of a neurotoxin damaging the neuronal terminal of axons. We then applied the same MRI protocol to map axonal integrity in the brain of multiple sclerosis relapsing-remitting patients and age-matched healthy controls. AxCaliber is sensitive to acute axonal damage in rats, as demonstrated by a significant increase in the mean axonal caliber along the targeted tract, which correlated with neurofilament staining. Electron microscopy confirmed that increased mean axonal diameter is associated with acute axonal pathology. In humans with multiple sclerosis, we uncovered a diffuse increase in mean axonal caliber in most areas of the normal-appearing white matter, preferentially affecting patients with short disease duration. Our results demonstrate that MRI-based axonal diameter mapping is a sensitive and specific imaging biomarker that links noninvasive imaging contrasts with the underlying biological substrate, uncovering generalized axonal damage in multiple sclerosis as an early event.

Editor's evaluation

This is a valuable study that aims to validate and translate an established non-invasive proxy measure of axonal diameter that is derived from magnetic resonance imaging. The results are solid, demonstrating alterations in the proxy measure in rodent models of axonal damage and patients with multiple sclerosis. The Discussion acknowledges weaknesses relating to the details of modelling and signal-to-noise ratio of the measurements. This work will be of interest to researchers studying the microstructural changes in neurodegeneration.

***For correspondence:** dsilvia@umh.es

†These authors contributed equally to this work
‡These authors also contributed equally to this work

Competing interest: The authors declare that no competing interests exist.

Funding: See page 14

Received: 01 April 2022
Preprinted: 29 April 2022
Accepted: 05 December 2023
Published: 09 January 2024

Reviewing Editor: Karla L Miller, University of Oxford, United Kingdom

Introduction

Axonal damage is the main pathological substrate of irreversible neurological disability in multiple sclerosis (MS). In MS, axonal damage can either be direct or secondary to demyelination, glial

activation, or exposure to excitatory amino acids and cytokines (***Haines et al., 2011***). As the transition to progressive MS occurs when an axonal loss threshold is reached, and the brain compensatory capacity is surpassed (***Criste et al., 2014***), the development of novel in vivo, noninvasive strategies for characterizing axonal microstructure becomes essential for early disease detection.

Magnetic resonance imaging (MRI), particularly diffusion-based approaches, has been applied in MS to investigate the white matter (WM) damage (***Inglese and Bester, 2010***). However, conventional diffusion MRI is unspecific to different tissue compartments, such as axons or myelin (***De Santis et al., 2014***), hampering the ability to distinguish axonal damage from other microstructural changes. In addition, due to the limitations of quantitatively comparing in vivo to ex vivo data, validation of imaging findings is rarely performed (***Horowitz et al., 2015***). While animal models recapitulating specific aspects of MS pathophysiology are available (***Torkildsen et al., 2008***, ***Constantinescu et al., 2011***), none focuses on axonal damage but rather on the demyelinating aspect of the disease.

AxCaliber is an advanced imaging framework able to estimate an MRI axonal diameter proxy (***Assaf et al., 2008***), which has become applicable in humans thanks to recent hardware advances (***Jones et al., 2018***). AxCaliber has revealed a higher axonal diameter proxy in the normal-appearing WM (NAWM) of the corpus callosum of MS patients compared to healthy controls, which was interpreted as a sign of axonal damage (***Huang et al., 2016***). However, in its original formulation, AxCaliber is only applicable to voxels characterized by a single fiber orientation (such as the corpus callosum, as in ***Huang et al., 2016***), while at least 70% of brain voxels contain two or more dominant fiber orientations (***Jeurissen et al., 2013***). Recently, we used a modified AxCaliber model to map whole-brain MRI axonal diameter proxy (***De Santis et al., 2019b***), hence providing a means to characterize the axonal damage in MS in a whole-brain fashion.

From a pathophysiological point of view, measuring a higher estimated MRI axonal diameter proxy in MS does not, per se, represent conclusive evidence of axonal damage, especially in the light of the known bias toward larger axons of MRI-based axonal diameter quantification (***Horowitz et al., 2015***). Indeed, MRI sensitivity to axonal pathology is yet to be fully demonstrated to establish its clinical utility. Recently, an approach to selectively manipulate specific microstructural aspects of the parenchyma through targeted, unilateral injection of neurotoxic agents has been proposed (***Garcia-Hernandez et al., 2022***).

In this study, we aimed to (i) validate AxCaliber-based axonal mapping in a preclinical model of fimbrial damage induced by stereotaxic injection of ibotenic acid into the hippocampus and (ii) translate the model to investigate changes in axonal microstructure in the brain white matter of patients with MS, particularly in normal-appearing tissue where pathological microstructural abnormalities have been previously reported (***Luchicchi et al., 2021***). Specifically, we (iia) compared whole-brain, voxelwise MRI axonal diameter proxy in MS patients relative to healthy controls and (iib) tested the association between clinical features and the MRI axonal diameter proxy in MS patients. We uncovered an abnormal increase in the MRI axonal diameter proxy in NAWM in MS, outside the inflammatory lesions, which was greater in patients with short disease duration, implicating axonal pathology as a primary event in MS pathogenesis.

Results

A rat model of acute axonal damage

Fourteen days after injection of the neurotoxin ibotenic acid into the hippocampus, paired t-test revealed a significant increase in the mean MRI axonal diameter proxy ($p=0.021$) in the fimbria belonging to the injected hemisphere compared to the control (***Figure 1e***), confirming that the damage affected a large portion of the tract. The other parameters extracted from the MRI analysis are not significantly different between hemispheres, although there is a tendency of reduced slope of the extra-axonal radial diffusivity decay for increasing diffusion time in the injected hemisphere (***Figure 1—figure supplement 1***). The fimbrias were reconstructed through Diffusion Tensor Imaging (DTI)-based tractography. Through tract-based analysis, we revealed a significant effect of the injection ($F_{1,9}=20.3$, $p=0.001$), of the position along the tract ($F_{48,432}=83.9$, $p<0.001$) and of their interaction ($F_{48,432}=5.7$, $p=0.003$); post-hoc comparisons between injection type, performed for each position and corrected for multiple comparisons, revealed significant differences in the mean MRI axonal diameter proxy between ibotenic acid- and saline-injected tracts in most parts of the tract. Significant

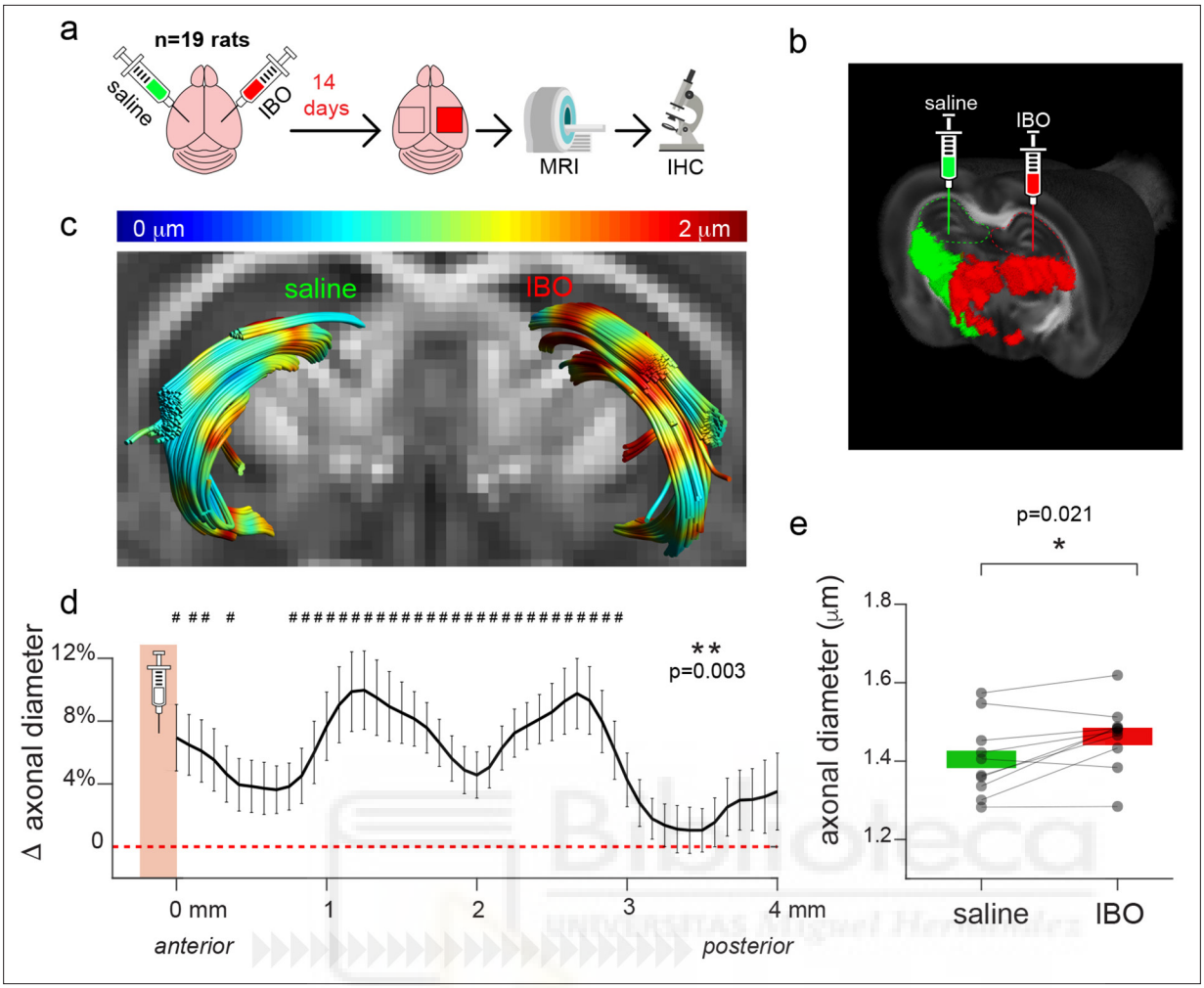

Figure 1. Experimental model of axonal damage. (**a**) Experimental scheme of stereotaxic injections of ibotenic acid (IBO) in the left hippocampus of n=19 rats. The right hippocampus was injected with saline solution and used as a control. (**b**) Visualization of the injection setup. (**c**) Example of the tractography of the fimbriae from one representative animal, superimposed on the fractional anisotropy map. The MRI axonal diameter proxy is projected on the tract through color coding. (**d**) Mean difference and standard deviation between groups of MRI axonal diameter proxy measured across all the streamlines constituting the fimbria in the antero-posterior axis, starting from the injection point (n=10). The injection site is shown in red. Asterisks represent significant group effect in the ANOVA, while hashtags represent significant post-hoc differences between groups in each location, corrected for multiple comparisons. (**e**) Mean MRI axonal diameter proxy calculated in the ibotenic vs saline-injected fimbria reconstructed using tractography. Asterisks represent significant differences (n=10, paired t test across hemispheres, p=0.021).

The online version of this article includes the following figure supplement(s) for figure 1:

Figure supplement 1. Other MRI parameters in control vs injected fimbriae.

Figure supplement 2. Axonal diameter estimation using the low b-value MRI protocol.

Figure supplement 3. Comparison between linear and log(t)/t functional forms.

differences were mostly localized posterior to the injection site (***Figure 1d***). In the subset of animals undergoing a protocol with lower b-values and a diffusion model not including the Δ dependency (AxCaliber), we obtained similar results (***Figure 1—figure supplement 2***).

When comparing immunofluorescence staining in ibotenic acid- versus saline-injected hemispheres, we confirmed both neuronal loss in the hippocampus (p=0.026, ***Figure 2a–b***) and axonal damage in the fimbria (p=0.047, ***Figure 2c–d***), corresponding to a lower staining intensity of neuronal nuclear protein (NeuN) and higher intensity of neurofilament staining in the hemisphere injected with ibotenic acid. No differences were found in the fimbria myelin content using Myelin Basic Protein (MBP) staining (***Figure 2—figure supplement 1***), suggesting that at the studied time point, axonal structure was significantly altered, but the total myelin content was still preserved. Neurofilament fluorescence intensity

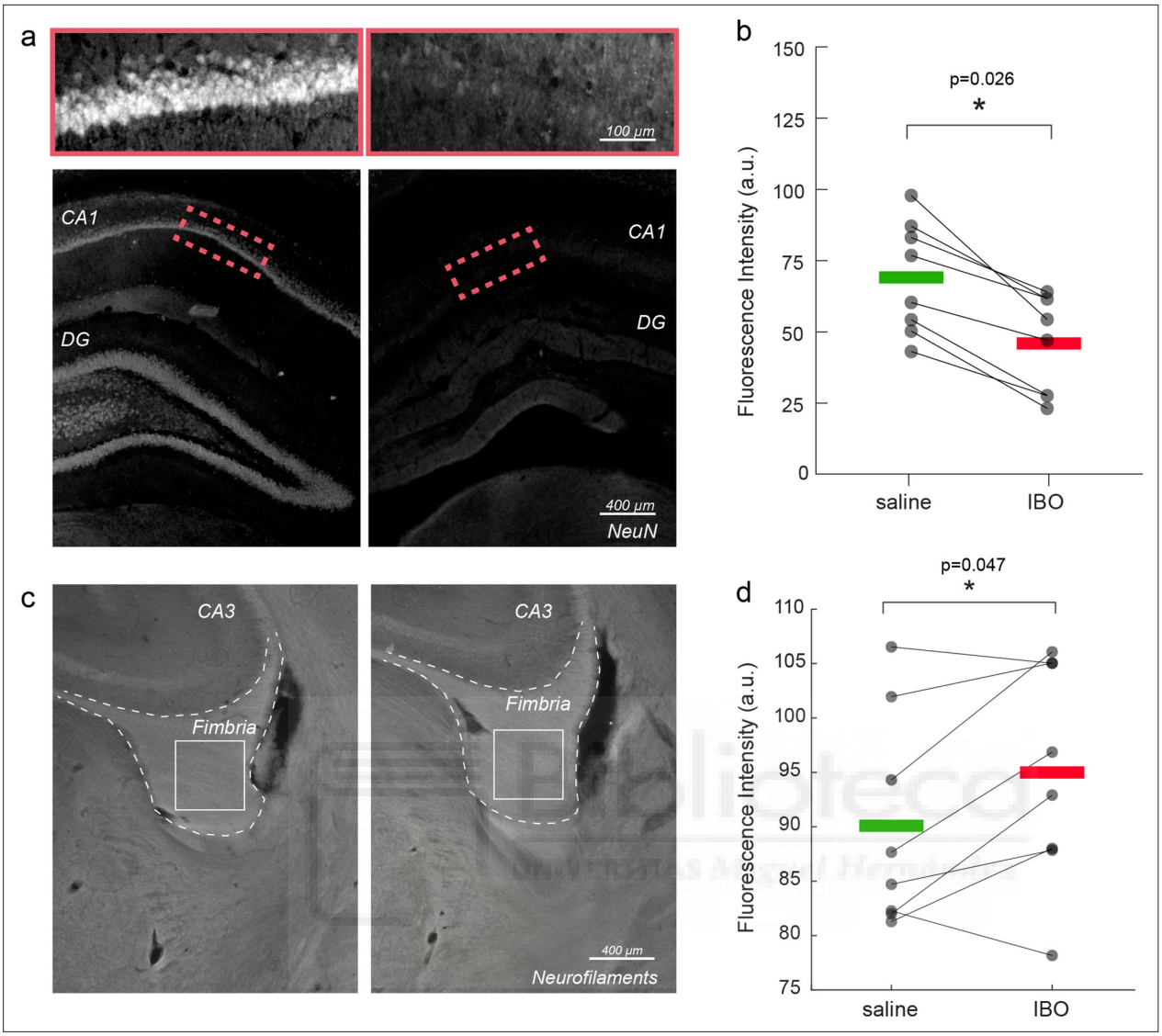

Figure 2. Immunofluorescence validation of axonal damage. (**a**) NeuN staining in control vs. injected hippocampi. (**b**) Mean NeuN intensity in control vs. injected hippocampi. Asterisks represent significant differences across hemispheres (n=8, paired t test, p=0.026). (**c**) Neurofilament staining in control vs. injected fimbria. (**d**) Mean neurofilament intensity in control vs. injected hippocampi. Asterisks represent significant differences in means across hemispheres (n=8, paired t test, p=0.047).

The online version of this article includes the following figure supplement(s) for figure 2:

Figure supplement 1. Myelin Basic Protein staining in injected versus control fimbria.

Figure supplement 2. Correlation between MRI and histology.

was significantly correlated with the axonal diameter proxy measured with MRI (r=0.54, p=0.029) in both the fimbria tract of injected and control hemispheres (***Figure 2—figure supplement 2***).

Scanning transmission electron microscopy (STEM) revealed increased axonal diameter in the hemisphere injected with ibotenic acid, with no significant reduction in axonal count, indicating limited axonal loss, as reported in ***Figure 3***. In ***Figure 3—figure supplement 1***, the total brain shrinkage from in vivo to after perfusion was quantified in three animals as 28%. Since the post-fixation with 1% osmium tetroxide gives at least a 15% additional shrinkage (***Kinney et al., 2013***), the total shrinkage caused by the STEM preparation can be quantified as 39%.

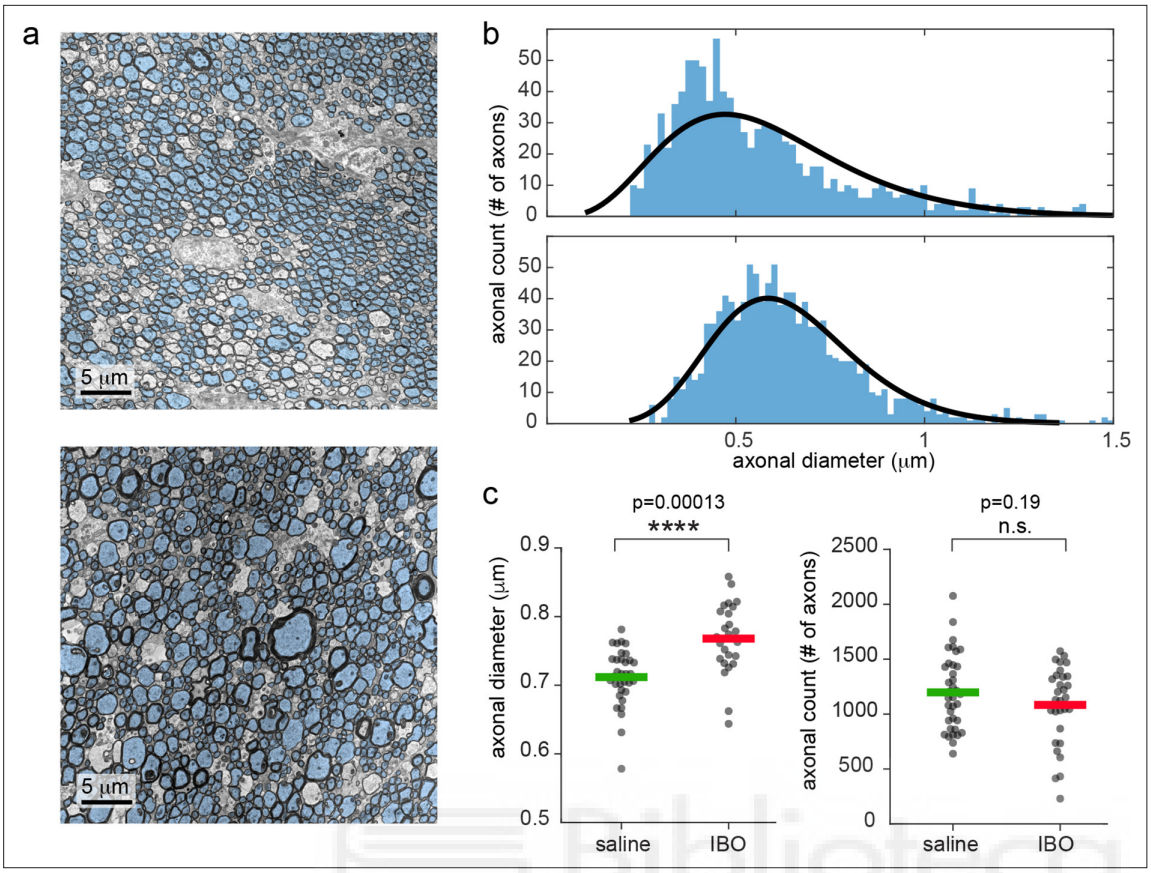

Figure 3. Electron microscopy shows increased mean axonal diameter in ibotenic-injected hemisphere compared to saline. (**a**) Representative STEM photos for saline and ibotenic acid fimbriae. Segmented axons are overlaid in light blue. (**b**) Histogram of the axonal count in one representative animal: upper line, saline injected, lower line, ibotenic. Black lines represent the gamma function better fitting the histogram. (**c**) Mean axonal diameter (left) and count (right) in each photo and group. Asterisks represent significant unpaired t test differences between groups for axonal diameter (n=6, p=0.00013).

The online version of this article includes the following figure supplement(s) for figure 3:

Figure supplement 1. Brain shrinkage during histology.

Axonal damage in normal-appearing white matter of multiple sclerosis patients

After preclinical validation in rats, we applied the clinical version of the AxCaliber MRI protocol to a cohort of 11 MS patients and 10 age-matched healthy controls. When comparing the MRI axonal diameter proxy in the NAWM of MS patients and controls, we found higher values in the MS group ($p<0.05$, corrected; ***Figure 4***). The differences were mostly symmetrical across hemispheres and involved all major WM tracts, notably: the corpus callosum, the corticospinal tract, the internal capsule, the corona radiata, the thalamic radiation, the inferior longitudinal fasciculus, the cingulum, the fornix, the superior longitudinal fasciculus, the inferior fronto-occipital fasciculus, the uncinate fasciculus, and the tapetum.

Axonal diameter is preferentially increased in patients with early disease

Next, we tested for associations between the measured MRI axonal diameter proxy and the disease duration. The rationale is that axonal swelling could be an early event in the disease, as suggested by postmortem evidence (***Luchicchi et al., 2021***).

Tract-based spatial statistics unveiled a trend of negative correlation between the magnitude of the MRI axonal diameter proxy in patients and the disease duration, as shown in ***Figure 5a***. When comparing average values of MRI axonal diameter proxy in the whole white matter (excluding lesions in MS) between groups (controls, short and long disease duration), we report a significant group effect

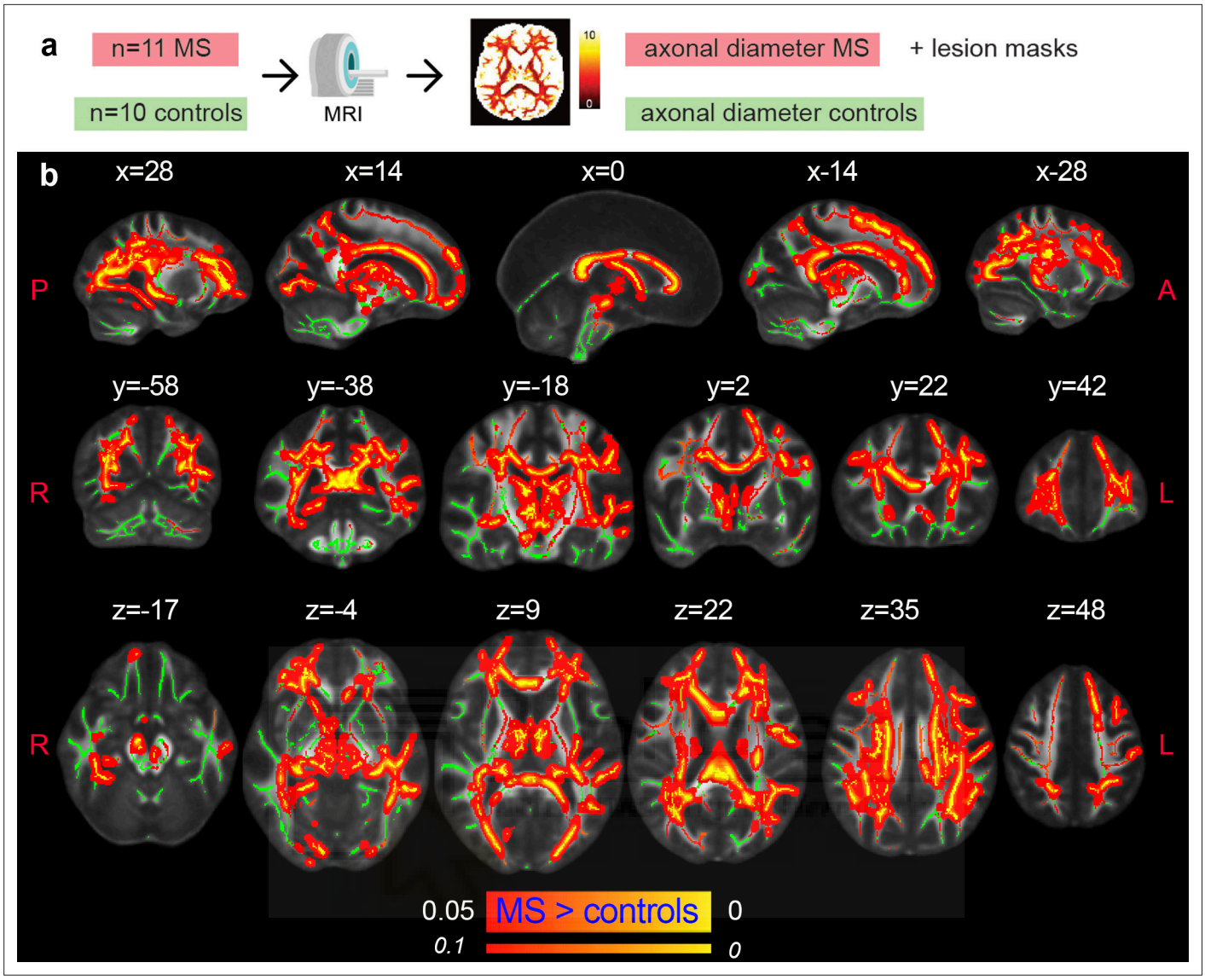

Figure 4. Axonal damage in MS normal-appearing white matter. (**a**) Experimental scheme. (**b**) Tract-based spatial statistics showing voxels in which the mean MRI axonal diameter proxy is significantly increased in multiple sclerosis versus healthy conditions (n=21, p<0.05, corrected). The opposite contrast was not statistically significant. Green: skeletonized white matter. Inflated red-yellow (through the pipeline tbss_fill): significant p value. Red-yellow: p-value <0.1.

The online version of this article includes the following figure supplement(s) for figure 4:

Figure supplement 1. Slope of extra-axonal radial diffusivity and restricted signal fraction in patients vs. controls.

Figure supplement 2. Rician simulations showing accuracy of MRI axonal diameters proxy.

in the ANOVA ($F_{2,18}$=9.2, p=0.002). MS patients for whom the disease onset was less than 5 years prior to the MRI scan had increased axonal diameter compared to controls (p=0.001, corrected for multiple comparisons), while this increase was not significant in MS patients with a longer disease course (p=0.18). We did not find significant associations between axonal diameter and other tested clinical variables of neurological disability and information processing speed (Expanded Disability Status Scale [EDDS] and Symbol Digit Modalities Test [SDMT]).

Finally, we tested both group differences and associations with disease duration for the rest of the parameters extracted in the MRI analysis. While both the slope of the extra-axonal radial diffusivity decay for increasing diffusion time and the restricted signal fraction are significantly reduced in a

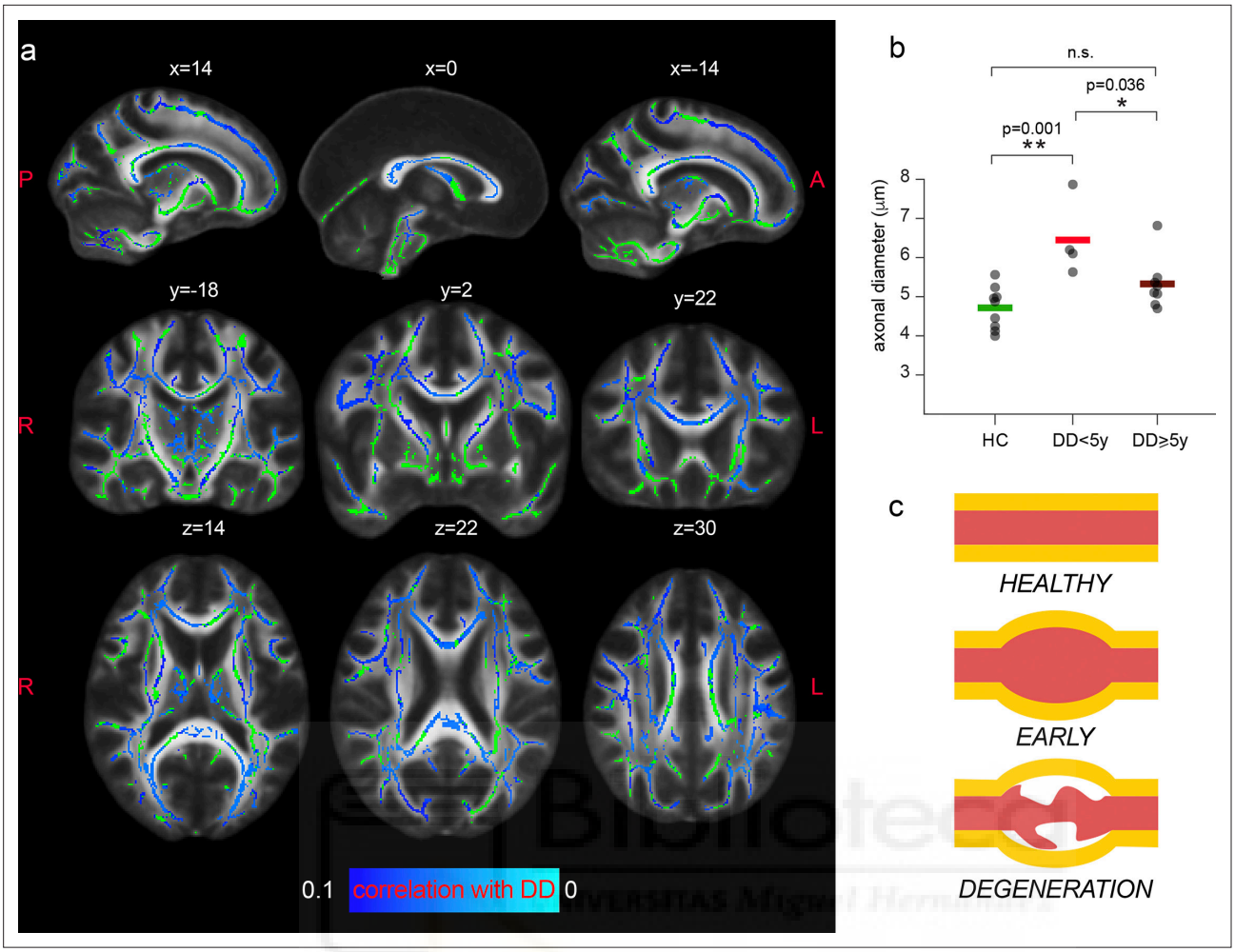

Figure 5. Axonal diameter is preferentially increased in patients with early MS. (**a**) Tract-based spatial statistics showing voxels in which a trend of negative association between the MRI axonal diameter proxy and the disease duration (DD) in patients is present (n=11, p<0.1; lowest p-value = 0.051 corrected). Green: skeletonized white matter. Bluel-light blue: p value. (**b**) Mean axonal diameter in the whole with matter of healthy controls (n=10, green), MS patients early in the disease course (n=4, <5 years, in red) and MS patients with a longer disease trajectory (n=7, ≥ 5 years, dark red). Asterisks represent unpaired post-hoc group differences following significant group effect in the ANOVA. (**c**) Schematic progression of early axonal damage. Figure 5c has been adapted from Figure 1E from ***Luchicchi et al., 2021***.

portion of the normal-appearing white matter in MS (reported in ***Figure 4—figure supplement 1***), no MRI parameter except the MRI axonal diameter proxy is significantly associated with disease duration.

Discussion

In this work, we used a preclinical model of acute axonal damage to demonstrate that MRI-based axonal diameter mapping is sensitive to axonal degeneration. We then applied the same MRI preclinical protocol to a cohort of patients with MS and age-matched healthy controls, uncovering diffuse axonal damage in the NAWM of MS patients that was inversely associated with disease duration.

Neuropathologically, early axonal damage in MS manifests through the formation of varicosities and spheroids that enlarge the axonal diameter and are associated with impaired axonal transport (***Criste et al., 2014***). Accordingly, histological postmortem (***Bergers et al., 2002***) and animal studies (***Nikić et al., 2011***) report an increase in the mean axonal diameter in MS compared to controls in demyelinating and non-demyelinating areas. This increase is also influenced by the higher vulnerability of smaller axons compared to larger ones (***Tallantyre et al., 2010***), which implies that smaller axons are lost earlier. Histological alterations in axonal morphology have also been observed in the

NAWM of MS brain specimens in the absence of inflammation (**Luchicchi et al., 2021**), suggesting that an imbalance of axon-myelin units could represent the primary event in MS pathogenesis.

Based on neuropathological evidence, axonal damage in MS would reasonably manifest as an increase in axonal caliber measured with imaging. An increase in axonal diameter in MS was indeed reported in previous MRI studies (**Huang et al., 2016**), but the results were not validated. In the context of multicompartment models for diffusion signals, comparing imaging results with pathological evidence is fundamental to validate the model, as multicompartment models make numerous assumptions and simplifications (to cite a few: fixed diffusivities [**Alexander et al., 2010**], no exchange [**Lasič et al., 2011**], indirect account of the volume occupied by myelin [**Assaf et al., 2008**]).

Previous studies reported correlations between the axonal diameter measured with MRI and axonal caliber estimated using electron microscopy in healthy tissue (**Barazany et al., 2009**), but with a reduced sample size. In addition, none thus far have demonstrated that AxCaliber is sensitive to axonal damage. Quantitative comparison between MRI maps and stained sections is severely hampered by the fixation process and other limitations (**Horowitz et al., 2015**; **Barakovic et al., 2023**); here, we used a well-characterized rodent model in which the axonal compartment is selectively damaged. This approach has been previously used to prove the capability of diffusion MRI to dissect astrocyte and microglia reactivity in gray matter (**Garcia-Hernandez et al., 2022**). Here, we detected increased neurofilament staining intensity in the damaged tract, demonstrating altered axonal morphology without alteration in the total amount of myelin. This change is picked up by MRI as an increase in the MRI axonal diameter proxy. Electron microscopy and axonal diameter quantification demonstrate that the increase observed in imaging reflects true morphological axonal alterations, hallmarks of axonal pathology. The significant correlation between neurofilament staining intensity and the MRI axonal diameter proxy further validates the imaging parameter as a marker of axonal damage, and is compatible with recent work studying the association of MRI metrics sensitive to axonal pathology and the serum neurofilament light chain biomarker in humans (**Rahmanzadeh et al., 2021**). Overall, our preclinical results show that axonal diameter mapping through MRI can detect axonal pathology in vivo and can thus be used as a biomarker of axonal damage in MS and possibly other neurological diseases. These results are extremely important given the ongoing debate on the discrepancy between MRI axonal diameter proxy and axonal diameter measured in fixated tissue using electron microscopy. The fact that both MRI and STEM detect a significant increase in the axonal diameter reconciles such findings, demonstrating that while absolute quantification of axonal caliber might differ (with MRI consistently overestimating axonal diameter due to higher weightings of larger axons, and STEM consistently underestimating axonal diameter due to heavy tissue fixation, as shown by our shrinkage analysis), both are sensitive to the same underlying pathological phenomenon. In many clinical contexts, detecting differences in pathological versus healthy conditions is far more interesting and valuable than absolute quantification, and we firmly believe this result validates the use of MRI-based axonal diameter mapping. In addition, we quantified the shrinkage due to the sample processing as high as 39% in our preparation. While this value cannot be directly used to correct STEM quantification, due to possible different shrinkage of extra- and intracellular space (**Barakovic et al., 2023**), it partially explains the discrepancy between STEM and MRI axonal diameter proxy, validating even further the used framework. Since this is an often-disregarded issue, we believe that this piece of information would help future validation of MRI-based microstructural characterization.

Our work used an AxCaliber formulation that allows accounting for multiple fibers and thus accesses whole-brain axonal diameter mapping. Indeed, while previous findings focused on the corpus callosum (**Huang et al., 2016**), our results indicate an increase in MRI axon diameter proxy in MS patients in all the major tracts, demonstrating diffuse axonal pathology in the NAWM. Notably, the combination of whole brain mapping and a larger sample size uncovered significant negative associations between MRI axonal diameter proxy and disease duration, suggesting enlarged axonal caliber as an early event in MS pathogenesis, as illustrated in **Figure 5c**. Other tested MRI parameters are not associated with disease duration. This result indicates that consolidated axonal loss can manifest as a reduction in axonal diameter, meaning that the increase in the MRI axonal diameter proxy observed in our MS population is a candidate marker for acute axonal damage. The presence of axonal pathology so early in the disease is an incredibly meaningful result that puts the spot of MS pathogenesis in degeneration rather than myelin loss (**Luchicchi et al., 2021**).

The lack of significant correlations with clinical variables (EDSS and SDMT) can possibly be explained by a lack of power due to limited sample size or potentially compensatory phenomena in our MS population, mainly composed of patients with relatively low disease scores. Although out of the scope of this work, it would be interesting to assess whether the MRI axonal diameter proxy is associated with more relevant clinical measures like the disability progression independent of relapse activity (***Granziera et al., 2023***).

This study has some limitations. Despite some inevitable minor differences due to different brain sizes and magnet features, the human protocol was built to match the main characteristics of the preclinical diffusion sequence, such as the b-value and diffusion time range. The chosen b-value has been a compromise between sensitivity to small structures and the signal-to-noise ratio (SNR) achievable in vivo and in the MS population, as indicated by recent animal (***Crater et al., 2022***) and human (***Jensen et al., 2016***; ***McKinnon et al., 2017***; ***Moss et al., 2019***) work, pointing at 3000–4000 s/mm^2 as the b-value for which the intra-axonal water signal starts to be observable. While some works question this value as too low to detect intra-axonal signal (***Veraart et al., 2020***), our shrinkage analysis suggests that current estimated sizes fed into the calculation to determine the minimum b-value needed to measure axonal diameter through MRI, as the one reported in ***De Santis et al., 2016***, should be updated. However, while feasible in vivo and in patients, this modest b-value is still suboptimal to measure axonal diameter, and higher b-values can boost the sensitivity to the intra-axonal compartment (***Veraart et al., 2020***; ***Barakovic et al., 2023***). In this context, including spherical mean techniques might improve axonal diameter and intra-axonal diffusivity estimations by factoring out the effect of fibre distribution, and by providing better SNR (***Fan et al., 2020***; ***Veraart et al., 2020***; ***Dhital et al., 2019***).

In a subset of animals, we tested a protocol with a lower b-value and a simpler AxCaliber model (without diffusion time dependency), with the aim of facilitating future clinical AxCaliber studies. We found no qualitative differences in the outcome: MRI axonal diameter proxy was increased following fimbria damage. This result should be taken with caution due to possible predominance of extra-axonal signal as a confounding factor (***Burcaw et al., 2015***); thus, further work and perhaps more realistic simulations, considering real cell composition and morphology, are needed to clarify this issue.

We must emphasize that our quantification of the axonal diameter distribution is conducted through a Poisson distribution, which utilizes a single parameter to define both the average and dispersion. Consequently, our current methodology does not permit us to ascertain whether the observed increase is attributable to a preferential loss of small caliber axons or axonal swelling. Future investigations employing a more comprehensive experimental protocol and higher b-value, possibly using non-parametric estimates as done by ***Romascano et al., 2020***, may provide the opportunity to measure the full diameter distribution, thereby offering more detailed insights into the underlying pathology.

In addition, the AxCaliber model does not take into account fiber dispersion present in the white matter. While some work point at modest values of dispersion at least in single-fiber areas (***Mollink et al., 2017***), other measured values as high as 20 degrees (***Ronen et al., 2014***; ***Lee et al., 2019***). While it is reasonable to expect that some axonal directional dispersion in areas of a single fiber is likely accounted for by the second fiber population, possibly mitigating the effect, future work should include spherical mean techniques to fully remove this bias.

It is important to stress that the aim of this work is not to propose a new animal model of MS, a disease that only affects humans, but rather to validate axonal damage detection (independently from the pathology that has induced it) through noninvasive MRI, and apply the framework to characterize axonal pathology in MS. The same innovative validation framework proposed here can be used in the future to dissect the sensitivity of other more refined methods to detect axonal pathology.

We cannot exclude that other pathological processes including glial activation and gliosis could have contributed, at least in part, to the observed changes in diffusion measures. However, in contrast to our findings of axonal swelling, these processes tend to increase with advancing of disease duration and stage (***Gallego-Delgado et al., 2020***). Additionally, pathological glial changes in MS do not occur in isolation but often in association with axonal changes. Future diffusion models combining estimates of changes either in soma or fiber diameter and density could help further elucidate this aspect.

Last, the method has been demonstrated preclinically only looking at one specific tract (the fimbria, as the tract with the largest number of hippocampal projections in the rat); however, it would be

straightforward to extrapolate our results to other tracts. Future studies are needed to demonstrate this.

In conclusion, given the central role of axonal pathology in MS, developing and validating strategies for early detection of axonal damage, in vivo and noninvasively, is of high priority; our results have the potential to improve early detection and monitoring of axonal pathology in the disease, as well as provide a novel imaging marker for monitoring the effects of treatments on the progression of axonal degeneration.

Materials and methods

Animal preparation

Animal preparation (n=19 rodents) was carried out as described before (***Garcia-Hernandez et al., 2022***). Briefly, axonal damage in the fimbria was achieved by injecting 1 µl of ibotenic acid (a selective agonist of N-methyl-D-aspartate (NMDA) glutamate receptors that produces selective neurotoxicity ***Zinkand et al., 1992***) at a concentration of 2.5 µg/µl in the dorsal hippocampus (coordinates bregma –3.8 mm, sup-inf 3.0 mm, 2 mm from the midline in the left hemisphere) (***Figure 1a***). Each animal was used as its own control by injecting the same amount of saline in the opposite hemisphere. The injection does not infect the contralateral structure, as previously reported (***Garcia-Hernandez et al., 2022***). Neuronal degeneration in the hippocampus translates into axonal loss in its major axonal output bundle, the fimbria, which is therefore used as a model for Wallerian-like axonal degeneration (***Conforti et al., 2014***). Fourteen days after surgery, rats underwent MRI scans in vivo using the AxCaliber protocol and were immediately perfused. N=9 animals were processed for immunohistological analysis, while n=6 animals were prepared for electron microscopy pipeline. Histological analysis was used to stain neuronal somas (NeuN) and quantify neuronal death in the hippocampus, neurofilaments and MBP to quantify axonal integrity and myelination in the fimbria, respectively. Electron microscopy was used to quantify axonal diameter and count in the fimbriae. N=3 additional animals were used to measure brain shrinkage from the in vivo condition to post-perfusion, post-fixation and post- sample embedding.

Subjects

The local institutional review board approved this study and written informed consent was obtained from all participants. Eleven MS patients (age range 26–57, 6 males) and ten healthy controls (age range 23–53, 4 males) participated in the study. The minimum sample size needed to detect the effect was calculated based on previous literature (***Huang et al., 2016***). Age and sex were matched across groups. Eligibility criteria in patients were a diagnosis of relapsing-remitting MS (***Polman et al., 2011***), being on stable disease-modifying treatment or no treatment for at least 3 months, absence of clinical relapse within 3 months, and absence of corticosteroid use within one month from study enrollment. A neurologist assessed physical disability according to the EDSS (***Kurtzke, 1983***) and cognitive ability using the SDMT. Demographic and clinical data are shown in ***Table 1***.

Table 1. Demographic characteristics of the studied cohort, including age/sex, disease duration, EDSS, SDMT, and MS treatment.

The reported p-value is the outcome of the chi-square test comparing MS and healthy controls.

	HC (n=10)		MS (n=11)		p value
Age (mean and SD)	35 y	+/-11 y	43 y	+/-12 y	0.27
Sex	6 M		4 M		0.13
Disease duration (mean and SD)	-		6.40	+/-5.47	
EDSS (median, min/max)	-		2	1/4.5	
SDMT (mean z score and SD)	-		–0.70	+/-1.47	
Medication	-		1 avonex; 1 plegridy; 2 tecfidera; 1 gilenya; 3 ocrelizumab; 2 copaxone; 1 Rituximab		

MRI acquisition

Rats

MRI was performed on a 7T scanner (Bruker, BioSpect 70/30, Ettlingen, Germany) featuring a maximum gradient intensity of 700 mT/m. Diffusion Weighted Magnetic Resonance Imaging (DW-MRI) data were acquired using a stimulated echo planar imaging diffusion sequence, with 132 uniform distributed gradient directions, b=0 (3), 2000(15) and 4000(15) s/mm^2, diffusion times (Δ) 15, 25, 40 and 60ms, diffusion pulse width 5ms, diffusion duration of 5ms, repetition time (TR)=7000ms and echo time (TE)=25ms. Fourteen slices were set up centered in the fimbria with field of view (FOV)=25 × 25 mm^2, matrix size = 110 × 110, in-plane resolution = 0.225 × 0.225 mm^2 and slice thickness = 0.6 mm. The total acquisition time was 1 hr. A subset of nine animals underwent a similar protocol, with slightly lower b-values (1000 and 2500 s/mm^2) to explore a protocol with better clinical compatibility. Finally, three animals underwent a T2-weighted high resolution MRI protocol with full brain coverage to measure the brain volume in vivo. The T2-weighted sequence was acquired using a Rapid Acquisition with Relaxation Enhancement sequence with TR = 6253ms, TE = 11ms, 4 averages. Fifty-six slices covered the whole brain with field of view 25×25 mm^2, matrix size 200×200, in-plane resolution 0.125×0.125 mm^2 and slice thickness 0.5 mm.

Humans

All participants were scanned on a Siemens 3T Connectom scanner, a customized 3T MAGNETOM Skyra system (Siemens Healthcare, Erlangen, Germany) housed at the MGH/HST Athinoula A. Martinos Center for Biomedical Imaging, Boston, Massachusetts, USA. The Connectom scanner is equipped with gradient coils capable of generating a maximum gradient strength of 300 mT/m, hence allowing minimization of δ (gradient duration) and echo times even at high b-values. A 64-channel brain array coil (***Keil et al., 2013***) was used for data acquisition. DW-MRI data were acquired using a spin echo echo planar imaging diffusion sequence, with 273 uniformly distributed gradient directions, b=0 (1), 2000(30), and 4000(60) s/mm^2, diffusion times (Δ) 17, 35, and 61 ms with four nondiffusion weighted images, diffusion pulse width 7ms, TR = 5000 ms and TE = 89ms. Eighty-two slices were set up to cover the whole brain with FOV = 220 × 220 mm^2, matrix size = 110 × 110, in-plane resolution = 2 × 2 mm^2 and slice thickness = 2 mm, partial Fourier factor 7/8, GRAPPA acceleration factor 2. In addition, anatomical images were acquired using 3D sequences with a 1.0 mm isotropic voxel size: T_1-weighted multiecho magnetization-prepared rapid gradient-echo images were acquired in all participants (***van der Kouwe et al., 2008***). Fluid-attenuation inversion recovery (FLAIR) images were also acquired in MS patients for white matter lesion segmentation. The total acquisition time was around 1 hr.

Tissue processing for immunohistochemistry

Rats were deeply anesthetized with a lethal dose of sodium pentobarbital, 46 mg/kg, injected intraperitoneally (Dolethal, E.V.S.A. laboratories., Madrid, España). Rats were then perfused intracardially with 100 ml of 0.9% phosphate saline buffer (PBS) and 100 ml of ice-cold 4% paraformaldehyde (PFA, BDH, Prolabo, VWR International, Louvain, Belgium). Then, brains were immediately extracted from the skull and fixed for 1 hr in 4% PFA. Afterwards, brains were included in 3% agarose/PBS (Sigma–Aldrich, Madrid, Spain) and cut in a vibratome (VT 1000 S, Leica, Wetzlar, Germany) into 50-µm-thick serial coronal sections.

Coronal sections were rinsed and permeabilized three times in 1 x PBS with Triton X-100 at 0.5% (Sigma–Aldrich, Madrid, Spain) for 10 min each and then blocked in the same solution with 4% bovine serum albumin (Sigma-Aldrich, Madrid, Spain) and 2% goat serum donor herd (Sigma-Aldrich) for 2 hr at room temperature. The slices were then incubated overnight at 4 °C with primary antibodies against myelin basic protein (1:250 Millipore Cat# MAB384-1ML, RRID:AB_240837), neurofilament 160 kD medium (1:250, Abcam Cat# ab134458, RRID:AB_2860025) and NeuN (1:250, Millipore Cat# MAB377, RRID:AB_2298772) to label myelin, axonal processes and nuclei, respectively. The sections were subsequently incubated in specific secondary antibodies conjugated to the fluorescent probes, each at 1:500 (Molecular Probes Cat# A-11029, RRID:AB_2534088; Molecular Probes Cat# A-11042, RRID:AB_2534099) for 2 hr at room temperature. Sections were then treated with 4′,6-Diamidine-2′-phenylindole dihydrochloride at 15 mM (DAPI, Sigma-Aldrich) for 15 min at room temperature. Finally, sections were mounted on slides and covered with an anti-fading medium using a mix solution 1:10 Propyl-gallate: Mowiol (P3130, Sigma-Aldrich; 475904, MERCK-Millipore,

Massachusetts, United States). For myelin labeling, antigen retrieval was performed in 1% citrate buffer (Sigma-Aldrich) and 0.05% Tween 20 (Sigma-Aldrich) warmed to 80 °C for protein unmasking.

The tissue sections were then examined using a computer-assisted morphometry system consisting of a Leica DM4000 fluorescence microscope equipped with a QICAM Qimaging camera 22577 (Biocompare, San Francisco, USA) and Neurolucida morphometric software (MBF, Biosciences, VT, USA). Myelin, neurofilament and neural nuclei fluorescent analysis was performed using Icy software (***de Chaumont et al., 2012***). For neural nuclei, two ROIs of 200 μm^2 were placed per hippocampus per hemisphere in at least 5 slices per rat to obtain the corresponding intensity values. Similarly, for MBP and neurofilaments, an ROI of 400 μm^2 was placed per fimbria per hemisphere in at least 5 slices per rat.

Tissue processing for electron microscopy

Rats were deeply anesthetized with a lethal dose of sodium pentobarbital, 46 mg/kg, injected intraperitoneally (Dolethal, E.V.S.A. laboratories., Madrid, Spain). Afterwards, rats were transcardially perfused with 100 ml of 0.9% PBS and 100 ml of a fixative solution containing 2% paraformaldehyde and 2.5% glutaraldehyde in 0.1 M cacodylate buffer (pH 7.3) (Electron Microscopy Science, USA). The brains were quickly removed and postfixed overnight in the same fixative solution at 4 °C. The following day, the brains were washed with 0.1 M cacodylate buffer. Subsequently, the fixed brains were sliced into 250-µm-thick horizontal sections using a vibratome (Leica VT1000S, Germany). The sections were collected in cacodylate buffer, and those containing the fimbria were washed three times with 0.1 M cacodylate buffer for 15 minutes each, and subsequently postfixed with 1% osmium tetroxide in 0.1 M cacodylate buffer for 1.5 hr at 4 °C. The tissue was then washed in distilled water twice for 15 min each and dehydrated in a graded series of ethanol solutions, followed by propylene oxide. The sections were then infiltrated with a mixture of propylene oxide and Agar 100 embedding resin (Agar Scientific, UK) for 2 hr at room temperature, and then placed in fresh embedding resin overnight at room temperature. The following day, the samples were transferred to fresh embedding resin and polymerized for 30 hr at 60 °C in flat silicon moulds. Ultrathin sections (90 nm) were cut using an ultramicrotome (Leica UC7) and placed on formvar-coated copper slot grids. The ultrathin sections were then stained with lead citrate and imaged using STEM on a scanning electron microscope (Zeiss GeminiSEM 460, Germany).

Photos were binarized, and axons were quantified semiautomatically by two operators blind to animals and conditions (ACC and SDS). While the cell's inner area is detected automatically using the MATLAB function *bwconncomp*, nonaxonal structures are eliminated via visual screening. Six photos per condition per animal were analyzed, generating a total segmented number of axons of 12272. Axonal diameter and count were compared across conditions using an unpaired t test.

Volume measurements

Volume measurements were taken using high-resolution T2-weighted images for in vivo conditions. Four different measurements were obtained for ex vivo conditions: immediately after perfusion, and at 4-, 7-, and 10 days post-perfusion. The volumes were extracted as follows: in vivo volumes were calculated by counting the number of voxels corresponding to brain tissue in the high-resolution T2-weighted images, multiplied by the voxel volume. The volume of the perfused brains was measured using Archimedes' principle. Briefly, a predetermined volume of fresh fixative solution was placed in a test tube, and the fixed brain was inserted into it. The difference between the final and initial volumes was considered as the volume occupied by the brain.

Data analysis

Paired t tests were used to assess the differences in histological quantities between injected versus control hemispheres. Diffusion-weighted rat MRI data were preprocessed as described here (***De Santis et al., 2019a***). The mean signal-to-noise (SNR) of the b0 images, calculated according to ***Aja-Fernández et al., 2015*** was 11.2 for rats (fimbria average) and 17.3 for humans (white matter average). We also tested an alternative method (***Koay and Basser, 2006***) for SNR calculation. While the average SNR quantification was very similar between the two approaches, in the Koay and Basser SNR maps we observed artefacts due to the iterative process, so we decided to use the method by ***Aja-Fernández et al., 2015***.

Human diffusion-weighted MRI data were preprocessed with software tools in FreeSurfer V5.3.0 (https://surfer.nmr.mgh.harvard.edu) and FSL V5.0 (https://fsl.fmrib.ox.ac.uk). Preprocessing included gradient nonlinearity correction, motion correction, and eddy current correction, including corresponding b-matrix reorientation. Additional preprocessing details are available at http://www.humanconnectome.org/. In both rats and humans, MRI data were employed to fit the AxCaliber model using in-house software written in MATLAB R2015b (The Mathworks) to extract the average axonal diameter proxy. The theoretical framework described here (***De Santis et al., 2019b***) was modified to include the dependency of the extra-axonal signal on the diffusion time through a linear term, in the form $D^{RADIAL}_{\Delta MIN}$+slope*(D- D_{MIN}). While this is a simplification of the proposed Δ dependency (***Burcaw et al., 2015***), we believe that it is a parsimonious choice that is supported by the relatively short range of Δ values explored as compared to previous work exploring time dependency (***De Santis et al., 2016***; ***Fieremans et al., 2016***), and also by comparison of a linear with a non-linear model in our data through a Bayesian information criterion (BIC), which preferred a linear fit over the expression used in ***De Santis et al., 2016*** in 100% of the subjects. The comparison between the two functional forms fitted to the radial diffusivity for the dataset acquired with the lower b-value protocol is reported in ***Figure 1—figure supplement 3***. The fit is implemented through a cascade model as done in ***Harms et al., 2017***, so that an initial CHARMED fit (***Assaf and Basser, 2005***) is performed using the data acquired at the shorter diffusion time to initialize the volume fractions. The intra-axonal axial diffusivity and the main fiber orientations are estimated through the CHARMED fit and kept fixed in the AxCaliber fit. The radial diffusivity (at the shortest Δ) in the extra-axonal compartment is first modelled using the tortuosity approximation (***Zhang et al., 2012***), and then this constraint is released in a last iteration of model fitting where everything in the model is fixed except for the radial diffusivity and the noise factor. As such, the fitted parameters are: the restricted main orientations and fractions, the intra-axonal axial diffusivity, the extra-axonal radial diffusivity, the slope of the extra-axonal radial diffusivity decay for increasing Δ, the axonal diameter and the Rician noise term. For STEAM data, an additional T1 decay is included in the fit. The BIC preferred a mono-exponential T1 decay over a bi-exponential decay in 98% of the examined voxels. Simulations using Rician noise were run on 10^5 different combinations of parameters sampled randomly from a uniform distribution in the following ranges: axonal diameter 0.5–5 μm, volume fraction 0.1–0.5, intra-axonal axial diffusivity 0.7–2.2x10^{-3} mm^2/s. The simulations were repeated with a narrower range of intra-axonal axial diffusivity (1.7–2.2x10^{-3} mm^2/s) matching more closely the scenario proposed by ***Dhital et al., 2019***. Each configuration was simulated 10 times by adding different Rician random noise with two different values of SNRs, matching human and animal acquisitions. The results demonstrate excellent agreement between ground truth and fitted axonal diameter for both human and animal acquisitions: r=0.90 and 0.75 respectively for a single repetition, r=0.98 and 0.95 respectively for 10 repetitions, and r=0.92 and 0.79 respectively for the narrower intraaxonal axial diffusivity range. The simulations are shown in ***Figure 4—figure supplement 2***.

For all MS patients, lesion masks were segmented on the FLAIR images using a semiautomated method (3D-Slicer v4.2.0; https://www.slicer.org).

In rats, the fimbria was reconstructed bilaterally using the DTI-based tractography (***Figure 1b***) algorithm in the software ExploreDTI (***Leemans et al., 2009***), which was set to employ the lowest Δ and b-value. Mean axonal diameter values along the tracts were obtained for each animal in both hemispheres. Injection sites were aligned and considered the origin of the analyzed tract portion. Paired t tests were used to assess differences in the axonal diameter between the injected and contralateral fimbria, and repeated-measure ANOVA (factors: tract location, treatment (ibotenic acid *vs.* saline) and tract location*treatment) was used to assess the effect of ibotenic acid injection. p-Values were corrected according to Greenhouse-Geisser approach when sphericity assumption was not met. Post-hoc comparisons between treatment for each tract location were corrected for multiple comparisons according to the false discovery rate approach.

For groupwise analysis of NAWM, we employed a previously detailed approach (***De Santis et al., 2019a***). Briefly, fractional anisotropy maps (calculated using the lowest Δ and b-value) were employed to initialize the first steps of an improved version of the TBSS (***Smith et al., 2006***). This version performs the coregistration steps using extremely accurate tools (***Klein et al., 2009***). The warping procedure accounts for lesion masks by excluding them from the similarity metric calculation, a permutation-based nonparametric inference approach to general linear modeling (***Winkler et al.,***

2014). We tested for a general linear model comprising group and disease duration as regressors. Our hypothesis, compatible with postmortem evidence (*Luchicchi et al., 2021*), is that axonal blistering is an early event in the disease. Lesion masks were excluded from the statistical analysis, and multiple comparisons across clusters were controlled for by using threshold-free cluster enhancement. In addition, we tested for voxelwise associations of axonal diameter with EDSS and SDMT in MS patients only. Lastly, we calculate the average MRI axonal diameter proxy of each subject in the whole white matter (excluding lesions in MS) and compared the average across the three groups: healthy controls, MS with less than 5 years of disease duration, and MS with 5 or more years of disease duration.

Acknowledgements

We thank Aroa Sanz Maroto for excellent technical support and the ISABIAL electron microscopy service for assistance with experiments and quantification. We thank Dr. S Aja-Fernández for assistance with signal-to-noise calculations. Funding: This work was supported by NIH 1R21NS123419-01 to CM. SDS was supported by the the Spanish Ministerio de Ciencia e Innovación, Agencia Estatal de Investigación (PID2021-128909NA-I00), by the "Centro de Excelencia Severo Ochoa" Grant CEX2021-001165-S funded by MCIN/AEI/10.13039/501100011033, and by the Generalitat Valenciana through a Subvencion a la Excelencia de Juniors Investigadores (SEJI/2019/038) and a Subvencion para la contratación de investigadoras e investigadores doctores de excelencia 2021 (CIDEGENT/2021/015). ACC is supported by the Generalitat Valenciana through a PhD fellowship ACIF/2020/301. JAG-S is supported by a Miguel Servet Fellowship from the Spanish Health Institute Carlos III (CP22/00078).

Additional information

Funding

Funder	Grant reference number	Author
National Institutes of Health	NIH 1R21NS123419-01	Caterina Mainero
Agencia Estatal de Investigación	PID2021-128909NA-I00	Silvia De Santis
Ministry of Science, Innovation and Universities	CEX2021-001165-S	Silvia De Santis Antonio Cerdán Cerdá Jose A Gomez-Sanchez
Generalitat Valenciana	SEJI/2019/038	Silvia De Santis
Generalitat Valenciana	CIDEGENT/2021/015	Silvia De Santis
Generalitat Valenciana	ACIF/2020/301	Antonio Cerdán Cerdá
Instituto de Salud Carlos III	CP22/00078	Jose A Gomez-Sanchez

The funders had no role in study design, data collection and interpretation, or the decision to submit the work for publication.

Author contributions

Antonio Cerdán Cerdá, Formal analysis, Investigation, Methodology, Software, Visualization, Writing – original draft; Nicola Toschi, Conceptualization, Supervision, Investigation, Methodology, Writing – original draft, Writing – review and editing; Constantina A Treaba, Valeria Barletta, Ambica Mehndiratta, Software; Elena Herranz, Software, Methodology; Jose A Gomez-Sanchez, Resources, Methodology; Caterina Mainero, Conceptualization, Supervision, Funding acquisition, Methodology, Writing – original draft, Writing – review and editing; Silvia De Santis, Conceptualization, Data curation, Formal analysis, Funding acquisition, Investigation, Methodology, Project administration, Resources, Software, Supervision, Validation, Visualization, Writing – original draft, Writing – review and editing

Author ORCIDs

Antonio Cerdán Cerdá https://orcid.org/0000-0001-6641-014X
Jose A Gomez-Sanchez http://orcid.org/0000-0002-6746-1800

Silvia De Santis https://orcid.org/0000-0001-9739-6926

Ethics

The local institutional review board at the Massachussets General Hospital approved this study, and written informed consent was obtained from all participants.
All animal experiments were approved by the Institutional Animal Care and Use Committee of the Instituto de Neurociencias de Alicante, Alicante, Spain, and comply with the Spanish (law 32/2007) and European regulations (EU directive 86/609, EU decree 2001-486, and EU recommendation 2007/526/EC; Project MRI-STRUCTURE 677/2018). The ARRIVE 10 checklist was used.

Decision letter and Author response

Decision letter https://doi.org/10.7554/eLife.79169.sa1
Author response https://doi.org/10.7554/eLife.79169.sa2

Additional files

Supplementary files

- MDAR checklist

Data availability

The preclinical data (imaging and histology) and the human imaging data that support the findings of this study are available in the open repository DIGITAL.CSIC. The human data are anonymized according to the regulations of the institution where they were acquired (Massachusetts General Hospital, Boston, USA). The software used to process the imaging data is available in the open repository DIGITAL.CSIC.

The following datasets were generated:

Author(s)	Year	Dataset title	Dataset URL	Database and Identifier
De Santis S, Cerdán Cerdá A, Antonio T, Toschi N, Mainero C	2023	Multi-shell multi-delta MRI data from multiple sclerosis patients and controls, and rats injected with ibotenic acid in one hemisphere of the hippocampus	https://doi.org/10.20350/digitalCSIC/15716	DIGITAL.CSIC, 10.20350/digitalCSIC/15716
De Santis S	2022	AxCaliber_3D	https://doi.org/10.20350/digitalCSIC/14601	DIGITAL.CSIC, 10.20350/digitalCSIC/14601

References

Aja-Fernández S, Pie¸ciak T, Vegas-Sánchez-Ferrero G. 2015. Spatially variant noise estimation in MRI: A homomorphic approach. *Medical Image Analysis* **20**:184–197. DOI: https://doi.org/10.1016/j.media.2014.11.005

Alexander DC, Hubbard PL, Hall MG, Moore EA, Ptito M, Parker GJM, Dyrby TB. 2010. Orientationally invariant indices of axon diameter and density from diffusion MRI. *NeuroImage* **52**:1374–1389. DOI: https://doi.org/10.1016/j.neuroimage.2010.05.043, PMID: 20580932

Assaf Y, Basser PJ. 2005. Composite hindered and restricted model of diffusion (CHARMED) MR imaging of the human brain. *NeuroImage* **27**:48–58. DOI: https://doi.org/10.1016/j.neuroimage.2005.03.042, PMID: 15979342

Assaf Y, Blumenfeld-Katzir T, Yovel Y, Basser PJ. 2008. AxCaliber: A method for measuring axon diameter distribution from diffusion MRI. *Magnetic Resonance in Medicine* **59**:1347–1354. DOI: https://doi.org/10.1002/mrm.21577, PMID: 18506799

Barakovic M, Pizzolato M, Tax CMW, Rudrapatna U, Magon S, Dyrby TB, Granziera C, Thiran JP, Jones DK, Canales-Rodríguez EJ. 2023. Estimating axon radius using diffusion-relaxation MRI: calibrating a surface-based relaxation model with histology. *Frontiers in Neuroscience* **17**:1209521. DOI: https://doi.org/10.3389/fnins.2023.1209521, PMID: 37638307

Barazany D, Basser PJ, Assaf Y. 2009. In vivo measurement of axon diameter distribution in the corpus callosum of rat brain. *Brain* **132**:1210–1220. DOI: https://doi.org/10.1093/brain/awp042, PMID: 19403788

Bergers E, Bot JCJ, De Groot CJA, Polman CH, Lycklama à Nijeholt GJ, Castelijns JA, van der Valk P, Barkhof F. 2002. Axonal damage in the spinal cord of MS patients occurs largely independent of T2 MRI lesions. *Neurology* **59**:1766–1771. DOI: https://doi.org/10.1212/01.wnl.0000036566.00866.26, PMID: 12473766

Burcaw LM, Fieremans E, Novikov DS. 2015. Mesoscopic structure of neuronal tracts from time-dependent diffusion. *NeuroImage* **114**:18–37. DOI: https://doi.org/10.1016/j.neuroimage.2015.03.061, PMID: 25837598

Conforti L, Gilley J, Coleman MP. 2014. Wallerian degeneration: an emerging axon death pathway linking injury and disease. *Nature Reviews. Neuroscience* **15**:394–409. DOI: https://doi.org/10.1038/nrn3680, PMID: 24840802

Constantinescu CS, Farooqi N, O'Brien K, Gran B. 2011. Experimental autoimmune encephalomyelitis (EAE) as a model for multiple sclerosis (MS). *British Journal of Pharmacology* **164**:1079–1106. DOI: https://doi.org/10.1111/j.1476-5381.2011.01302.x, PMID: 21371012

Crater S, Maharjan S, Qi Y, Zhao Q, Cofer G, Cook JC, Johnson GA, Wang N. 2022. Resolution and b value dependent structural connectome in ex vivo mouse brain. *NeuroImage* **255**:119199. DOI: https://doi.org/10.1016/j.neuroimage.2022.119199, PMID: 35417754

Criste G, Trapp B, Dutta R. 2014. *Axonal Loss in Multiple sclerosisHandbook of Clinical Neurology* Elsevier. DOI: https://doi.org/10.1016/B978-0-444-52001-2.00005-4

de Chaumont F, Dallongeville S, Chenouard N, Hervé N, Pop S, Provoost T, Meas-Yedid V, Pankajakshan P, Lecomte T, Le Montagner Y, Lagache T, Dufour A, Olivo-Marin J-C. 2012. Icy: an open bioimage informatics platform for extended reproducible research. *Nature Methods* **9**:690–696. DOI: https://doi.org/10.1038/nmeth.2075

De Santis S, Drakesmith M, Bells S, Assaf Y, Jones DK. 2014. Why diffusion tensor MRI does well only some of the time: variance and covariance of white matter tissue microstructure attributes in the living human brain. *NeuroImage* **89**:35–44. DOI: https://doi.org/10.1016/j.neuroimage.2013.12.003, PMID: 24342225

De Santis S, Jones DK, Roebroeck A. 2016. Including diffusion time dependence in the extra-axonal space improves in vivo estimates of axonal diameter and density in human white matter. *NeuroImage* **130**:91–103. DOI: https://doi.org/10.1016/j.neuroimage.2016.01.047, PMID: 26826514

De Santis S, Granberg T, Ouellette R, Treaba CA, Herranz E, Fan Q, Mainero C, Toschi N. 2019a. Evidence of early microstructural white matter abnormalities in multiple sclerosis from multi-shell diffusion MRI. *NeuroImage. Clinical* **22**:101699. DOI: https://doi.org/10.1016/j.nicl.2019.101699, PMID: 30739842

De Santis S, Herranz E, Treaba CA, Barletta V, Mehndiratta A, Mainero C, Toschi N. 2019b. Whole brain in vivo axonal diameter mapping in multiple sclerosis. Annual International Conference of the IEEE Engineering in Medicine and Biology Society. IEEE Engineering in Medicine and Biology Society. Annual International Conference. 204–207. DOI: https://doi.org/10.1109/EMBC.2019.8856433, PMID: 31945878

Dhital B, Reisert M, Kellner E, Kiselev VG. 2019. Intra-axonal diffusivity in brain white matter. *NeuroImage* **189**:543–550. DOI: https://doi.org/10.1016/j.neuroimage.2019.01.015, PMID: 30659959

Fan Q, Nummenmaa A, Witzel T, Ohringer N, Tian Q, Setsompop K, Klawiter EC, Rosen BR, Wald LL, Huang SY. 2020. Axon diameter index estimation independent of fiber orientation distribution using high-gradient diffusion MRI. *NeuroImage* **222**:117197. DOI: https://doi.org/10.1016/j.neuroimage.2020.117197, PMID: 32745680

Fieremans E, Burcaw LM, Lee HH, Lemberskiy G, Veraart J, Novikov DS. 2016. In vivo observation and biophysical interpretation of time-dependent diffusion in human white matter. *NeuroImage* **129**:414–427. DOI: https://doi.org/10.1016/j.neuroimage.2016.01.018

Gallego-Delgado P, James R, Browne E, Meng J, Umashankar S, Tan L, Picon C, Mazarakis ND, Faisal AA, Howell OW, Reynolds R. 2020. Neuroinflammation in the normal-appearing white matter (NAWM) of the multiple sclerosis brain causes abnormalities at the nodes of Ranvier. *PLOS Biology* **18**:e3001008. DOI: https://doi.org/10.1371/journal.pbio.3001008, PMID: 33315860

Garcia-Hernandez R, Cerdán Cerdá A, Trouve Carpena A, Drakesmith M, Koller K, Jones DK, Canals S, De Santis S. 2022. Mapping microglia and astrocyte activation in vivo using diffusion MRI. *Science Advances* **8**:eabq2923. DOI: https://doi.org/10.1126/sciadv.abq2923, PMID: 35622913

Granziera C, Derfuss T, Kappos L. 2023. Time to change the current clinical classification of multiple sclerosis? *JAMA Neurology* **80**:128. DOI: https://doi.org/10.1001/jamaneurol.2022.4156

Haines JD, Inglese M, Casaccia P. 2011. Axonal damage in multiple sclerosis: a Xonal D Amage in MS. *The Mount Sinai Journal of Medicine* **78**:231–243. DOI: https://doi.org/10.1002/msj.20246

Harms RL, Fritz FJ, Tobisch A, Goebel R, Roebroeck A. 2017. Robust and fast nonlinear optimization of diffusion MRI microstructure models. *NeuroImage* **155**:82–96. DOI: https://doi.org/10.1016/j.neuroimage.2017.04.064

Horowitz A, Barazany D, Tavor I, Yovel G, Assaf Y. 2015. Response to the comments on the paper by Horowitz et al. (2014). *Brain Structure and Function* **220**:1791–1792. DOI: https://doi.org/10.1007/s00429-015-1031-x

Huang SY, Tobyne SM, Nummenmaa A, Witzel T, Wald LL, McNab JA, Klawiter EC. 2016. Characterization of axonal disease in patients with multiple sclerosis using high-gradient-diffusion MR imaging. *Radiology* **280**:244–251. DOI: https://doi.org/10.1148/radiol.2016151582, PMID: 26859256

Inglese M, Bester M. 2010. Diffusion imaging in multiple sclerosis: research and clinical implications. *NMR in Biomedicine* **23**:865–872. DOI: https://doi.org/10.1002/nbm.1515, PMID: 20882528

Jensen JH, Russell Glenn G, Helpern JA. 2016. Fiber ball imaging. *NeuroImage* **124**:824–833. DOI: https://doi.org/10.1016/j.neuroimage.2015.09.049, PMID: 26432187

Jeurissen B, Leemans A, Tournier JD, Jones DK, Sijbers J. 2013. Investigating the prevalence of complex fiber configurations in white matter tissue with diffusion magnetic resonance imaging. *Human Brain Mapping* **34**:2747–2766. DOI: https://doi.org/10.1002/hbm.22099, PMID: 22611035

Jones DK, Alexander DC, Bowtell R, Cercignani M, Dell'Acqua F, McHugh DJ, Miller KL, Palombo M, Parker GJM, Rudrapatna US, Tax CMW. 2018. Microstructural imaging of the human brain with a "super-

scanner": 10 key advantages of ultra-strong gradients for diffusion MRI. *NeuroImage* **182**:8–38. DOI: https://doi.org/10.1016/j.neuroimage.2018.05.047, PMID: 29793061

Keil B, Blau JN, Biber S, Hoecht P, Tountcheva V, Setsompop K, Triantafyllou C, Wald LL. 2013. A 64-channel 3T array coil for accelerated brain MRI. *Magnetic Resonance in Medicine* **70**:248–258. DOI: https://doi.org/10.1002/mrm.24427, PMID: 22851312

Kinney JP, Spacek J, Bartol TM, Bajaj CL, Harris KM, Sejnowski TJ. 2013. Extracellular sheets and tunnels modulate glutamate diffusion in hippocampal neuropil. *The Journal of Comparative Neurology* **521**:448–464. DOI: https://doi.org/10.1002/cne.23181, PMID: 22740128

Klein A, Andersson J, Ardekani BA, Ashburner J, Avants B, Chiang MC, Christensen GE, Collins DL, Gee J, Hellier P, Song JH, Jenkinson M, Lepage C, Rueckert D, Thompson P, Vercauteren T, Woods RP, Mann JJ, Parsey RV. 2009. Evaluation of 14 nonlinear deformation algorithms applied to human brain MRI registration. *NeuroImage* **46**:786–802. DOI: https://doi.org/10.1016/j.neuroimage.2008.12.037, PMID: 19195496

Koay CG, Basser PJ. 2006. Analytically exact correction scheme for signal extraction from noisy magnitude MR signals. *Journal of Magnetic Resonance* **179**:317–322. DOI: https://doi.org/10.1016/j.jmr.2006.01.016, PMID: 16488635

Kurtzke JF. 1983. Rating neurologic impairment in multiple sclerosis: an expanded disability status scale (EDSS). *Neurology* **33**:1444–1452. DOI: https://doi.org/10.1212/wnl.33.11.1444, PMID: 6685237

Lasič S, Nilsson M, Lätt J, Ståhlberg F, Topgaard D. 2011. Apparent exchange rate mapping with diffusion MRI. *Magnetic Resonance in Medicine* **66**:356–365. DOI: https://doi.org/10.1002/mrm.22782, PMID: 21446037

Lee HH, Yaros K, Veraart J, Pathan JL, Liang FX, Kim SG, Novikov DS, Fieremans E. 2019. Along-axon diameter variation and axonal orientation dispersion revealed with 3D electron microscopy: implications for quantifying brain white matter microstructure with histology and diffusion MRI. *Brain Structure & Function* **224**:1469–1488. DOI: https://doi.org/10.1007/s00429-019-01844-6, PMID: 30790073

Leemans A, Jeurissen B, Sijbers J, Jones DK. 2009. Exploredti: a graphical Toolbox for processing, analyzing, and Visualizing diffusion MR data. Magnetic Resonance Imaging.

Luchicchi A, Hart B, Frigerio I, van Dam A-M, Perna L, Offerhaus HL, Stys PK, Schenk GJ, Geurts JJG. 2021. Axon-myelin unit blistering as early event in MS normal appearing white matter. *Annals of Neurology* **89**:711–725. DOI: https://doi.org/10.1002/ana.26014, PMID: 33410190

McKinnon ET, Jensen JH, Glenn GR, Helpern JA. 2017. Dependence on b-value of the direction-averaged diffusion-weighted imaging signal in brain. *Magnetic Resonance Imaging* **36**:121–127. DOI: https://doi.org/10.1016/j.mri.2016.10.026, PMID: 27989904

Mollink J, Kleinnijenhuis M, Cappellen van Walsum AM, Sotiropoulos SN, Cottaar M, Mirfin C, Heinrich MP, Jenkinson M, Pallebage-Gamarallage M, Ansorge O, Jbabdi S, Miller KL. 2017. Evaluating fibre orientation dispersion in white matter: Comparison of diffusion MRI, histology and polarized light imaging. *NeuroImage* **157**:561–574. DOI: https://doi.org/10.1016/j.neuroimage.2017.06.001

Moss HG, McKinnon ET, Glenn GR, Helpern JA, Jensen JH. 2019. Optimization of data acquisition and analysis for fiber ball imaging. *NeuroImage* **200**:690–703. DOI: https://doi.org/10.1016/j.neuroimage.2019.07.005, PMID: 31284026

Nikić I, Merkler D, Sorbara C, Brinkoetter M, Kreutzfeldt M, Bareyre FM, Brück W, Bishop D, Misgeld T, Kerschensteiner M. 2011. A reversible form of axon damage in experimental autoimmune encephalomyelitis and multiple sclerosis. *Nature Medicine* **17**:495–499. DOI: https://doi.org/10.1038/nm.2324, PMID: 21441916

Polman CH, Reingold SC, Banwell B, Clanet M, Cohen JA, Filippi M, Fujihara K, Havrdova E, Hutchinson M, Kappos L, Lublin FD, Montalban X, O'Connor P, Sandberg-Wollheim M, Thompson AJ, Waubant E, Weinshenker B, Wolinsky JS. 2011. Diagnostic criteria for multiple sclerosis: 2010 Revisions to the McDonald criteria. *Annals of Neurology* **69**:292–302. DOI: https://doi.org/10.1002/ana.22366

Rahmanzadeh R, Lu P-J, Barakovic M, Weigel M, Maggi P, Nguyen TD, Schiavi S, Daducci A, La Rosa F, Schaedelin S, Absinta M, Reich DS, Sati P, Wang Y, Bach Cuadra M, Radue E-W, Kuhle J, Kappos L, Granziera C. 2021. Myelin and axon pathology in multiple sclerosis assessed by myelin water and multi-shell diffusion imaging. *Brain* **144**:1684–1696. DOI: https://doi.org/10.1093/brain/awab088, PMID: 33693571

Romascano D, Barakovic M, Rafael-Patino J, Dyrby TB, Thiran J-P, Daducci A. 2020. ActiveAx$_{ADD}$: toward non-parametric and orientationally invariant axon diameter distribution mapping using PGSE. *Magnetic Resonance in Medicine* **83**:2322–2330. DOI: https://doi.org/10.1002/mrm.28053, PMID: 31691378

Ronen I, Budde M, Ercan E, Annese J, Techawiboonwong A, Webb A. 2014. Microstructural organization of axons in the human corpus callosum quantified by diffusion-weighted magnetic resonance spectroscopy of N-acetylaspartate and post-mortem histology. *Brain Structure and Function* **219**:1773–1785. DOI: https://doi.org/10.1007/s00429-013-0600-0

Smith SM, Jenkinson M, Johansen-Berg H, Rueckert D, Nichols TE, Mackay CE, Watkins KE, Ciccarelli O, Cader MZ, Matthews PM, Behrens TEJ. 2006. Tract-based spatial statistics: Voxelwise analysis of multi-subject diffusion data. *NeuroImage* **31**:1487–1505. DOI: https://doi.org/10.1016/j.neuroimage.2006.02.024

Tallantyre EC, Bø L, Al-Rawashdeh O, Owens T, Polman CH, Lowe JS, Evangelou N. 2010. Clinico-pathological evidence that axonal loss underlies disability in progressive multiple sclerosis. *Multiple Sclerosis* **16**:406–411. DOI: https://doi.org/10.1177/1352458510364992, PMID: 20215480

Torkildsen Ø, Brunborg LA, Myhr KM, Bø L. 2008. The cuprizone model for demyelination. *Acta Neurologica Scandinavica* **117**:72–76. DOI: https://doi.org/10.1111/j.1600-0404.2008.01036.x

van der Kouwe AJW, Benner T, Salat DH, Fischl B. 2008. Brain morphometry with multiecho MPRAGE. *NeuroImage* **40**:559–569. DOI: https://doi.org/10.1016/j.neuroimage.2007.12.025

Veraart J, Nunes D, Rudrapatna U, Fieremans E, Jones DK, Novikov DS, Shemesh N. 2020. Nonivasive quantification of axon radii using diffusion MRI. *eLife* **9**:e49855. DOI: https://doi.org/10.7554/eLife.49855, PMID: 32048987

Winkler AM, Ridgway GR, Webster MA, Smith SM, Nichols TE. 2014. Permutation inference for the general linear model. *NeuroImage* **92**:381–397. DOI: https://doi.org/10.1016/j.neuroimage.2014.01.060, PMID: 24530839

Zhang H, Schneider T, Wheeler-Kingshott CA, Alexander DC. 2012. NODDI: practical in vivo neurite orientation dispersion and density imaging of the human brain. *NeuroImage* **61**:1000–1016. DOI: https://doi.org/10.1016/j.neuroimage.2012.03.072, PMID: 22484410

Zinkand WC, Moore WC, Thompson C, Salama AI, Patel J. 1992. Ibotenic acid mediates neurotoxicity and phosphoinositide hydrolysis by independent receptor mechanisms. *Molecular and Chemical Neuropathology* **16**:1–10. DOI: https://doi.org/10.1007/BF03159956, PMID: 1325800

Figures and figure supplements

A translational MRI approach to validate acute axonal damage detection as an early event in multiple sclerosis

Antonio Cerdán Cerdá and Nicola Toschi *et al*.

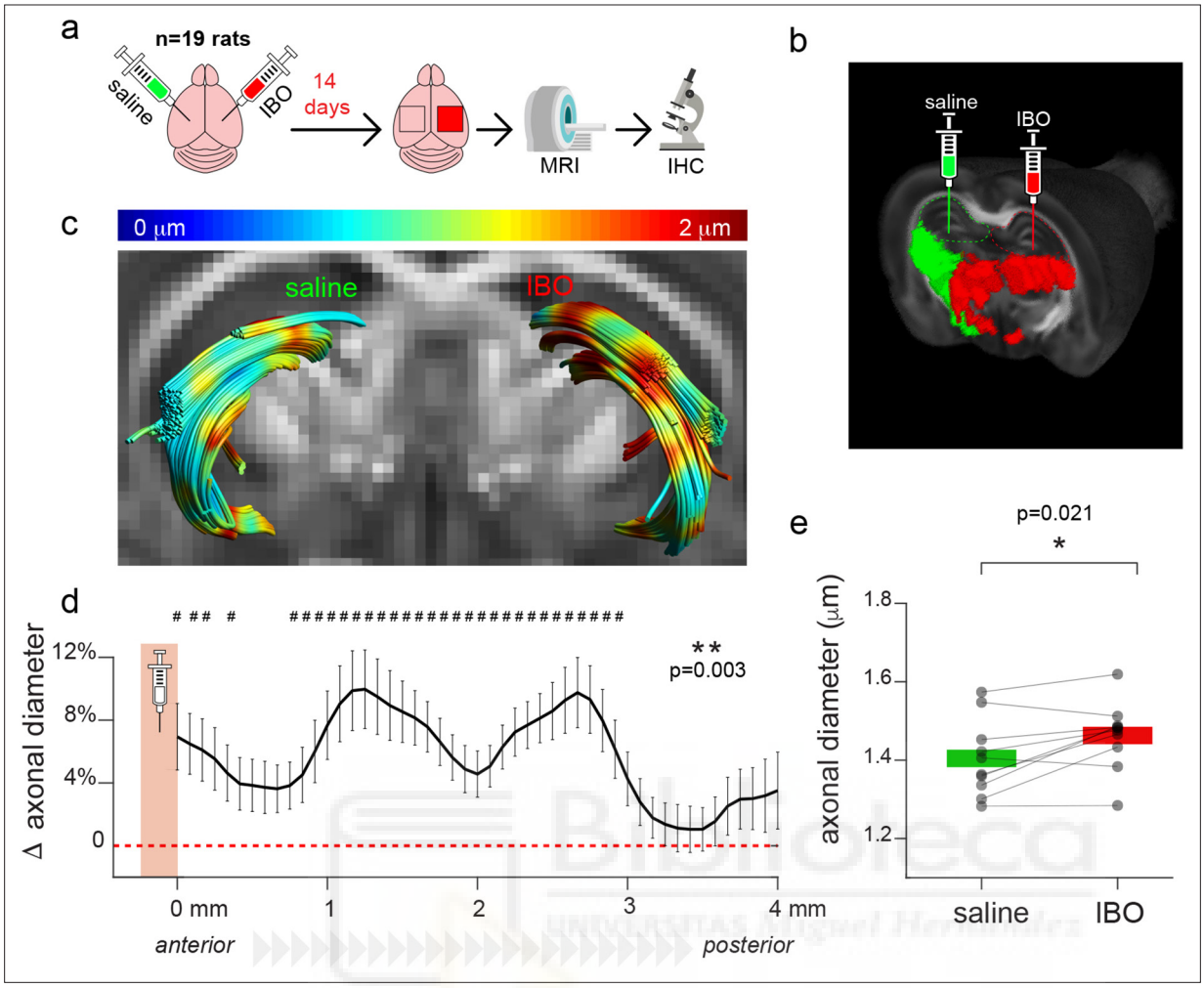

Figure 1. Experimental model of axonal damage. (**a**) Experimental scheme of stereotaxic injections of ibotenic acid (IBO) in the left hippocampus of n=19 rats. The right hippocampus was injected with saline solution and used as a control. (**b**) Visualization of the injection setup. (**c**) Example of the tractography of the fimbriae from one representative animal, superimposed on the fractional anisotropy map. The MRI axonal diameter proxy is projected on the tract through color coding. (**d**) Mean difference and standard deviation between groups of MRI axonal diameter proxy measured across all the streamlines constituting the fimbria in the antero-posterior axis, starting from the injection point (n=10). The injection site is shown in red. Asterisks represent significant group effect in the ANOVA, while hashtags represent significant post-hoc differences between groups in each location, corrected for multiple comparisons. (**e**) Mean MRI axonal diameter proxy calculated in the ibotenic vs saline-injected fimbria reconstructed using tractography. Asterisks represent significant differences (n=10, paired t test across hemispheres, p=0.021).

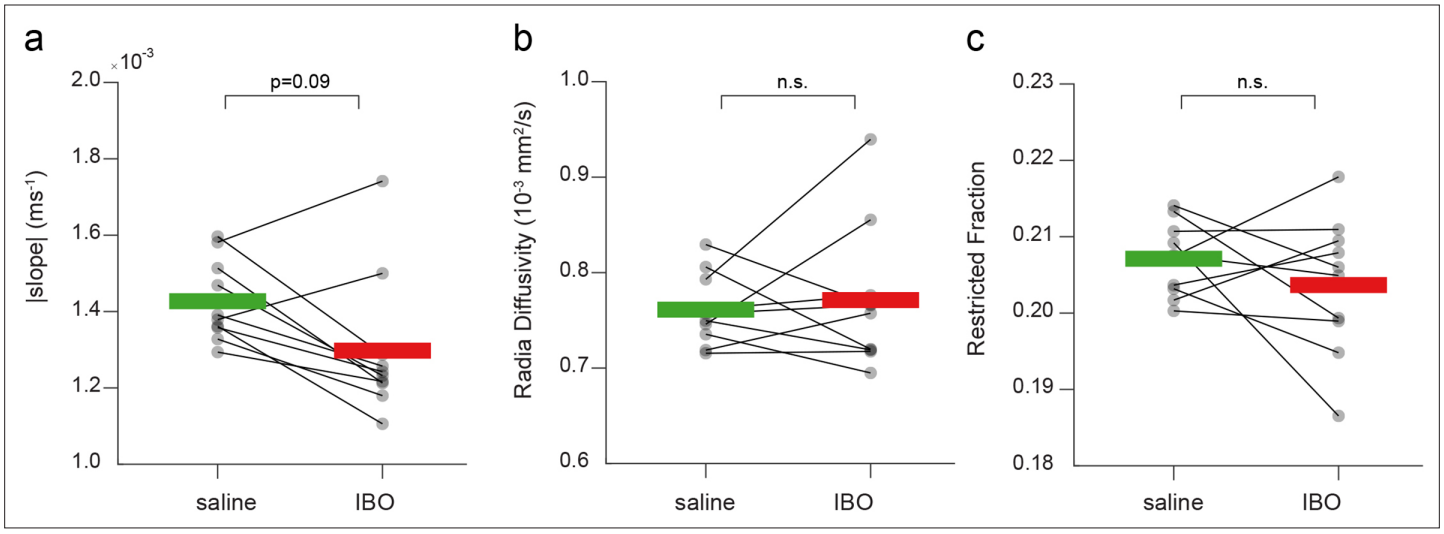

Figure 1—figure supplement 1. Other MRI parameters in control vs injected fimbriae. (**a**) Mean modulus of the slope of the dependency of the extra-axonal radial diffusivity from the diffusion time calculated in the ibotenic vs saline-injected fimbria reconstructed using tractography. The slope is always negative. (**b**) Extra-axonal radial diffusivity. (**c**) Restricted signal fraction. No significant differences are found (n=9, paired t test across hemispheres, p=0.09, 0.67 and 0.46 respectively).

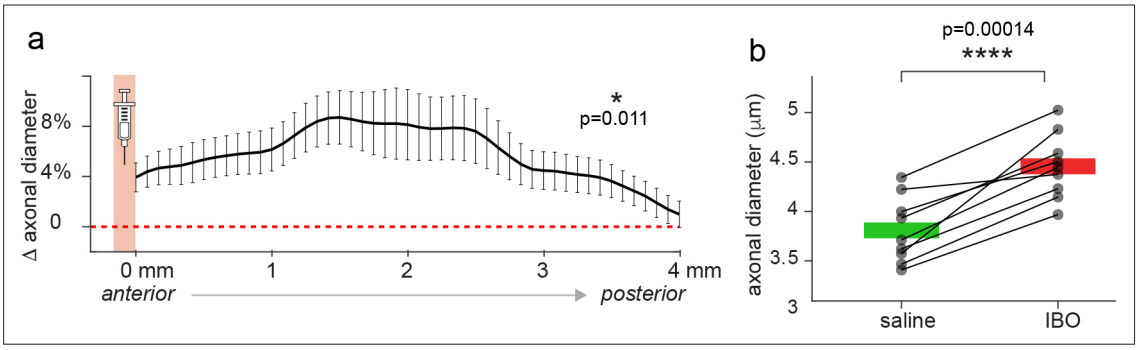

Figure 1—figure supplement 2. Axonal diameter estimation using the low b-value MRI protocol. (**a**) Mean difference and standard deviation between groups of axonal diameter measured across all the streamlines constituting the fimbria in the antero-posterior axis, starting from the injection point (n=9, low b-value protocol). The injection site is shown in red. Asterisk represents significant group effect in the ANOVA. (**b**) Mean MRI axonal diameter proxy calculated in the ibotenic vs saline-injected fimbria reconstructed using tractography. Asterisks represent significant differences (n=9, paired t test across hemispheres, p=0.000014).

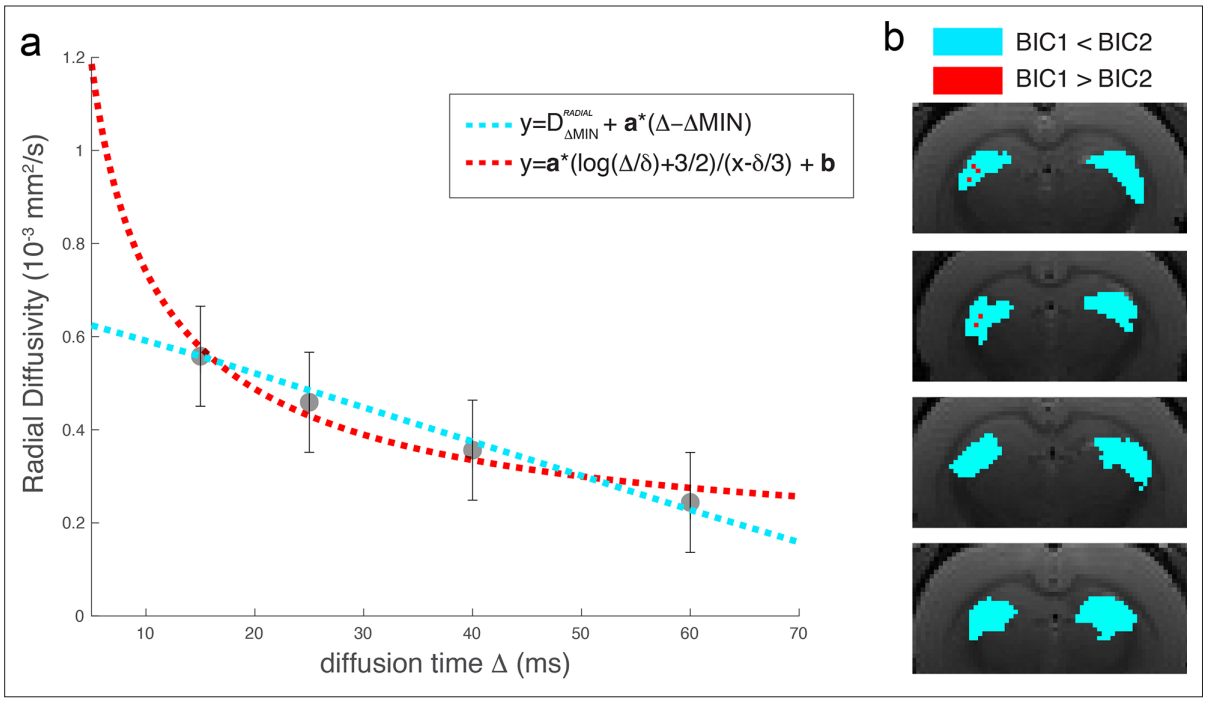

Figure 1—figure supplement 3. Comparison between linear and log(t)/t functional forms. (**a**) The two functional forms tested to fit the decay of the extra-axonal radial diffusivity are shown as a function of the diffusion times for the radial diffusivity measured on the protocol with lower b-value. (**b**) Example of the functional form chosen according to the BIC criterion in four of the animals.

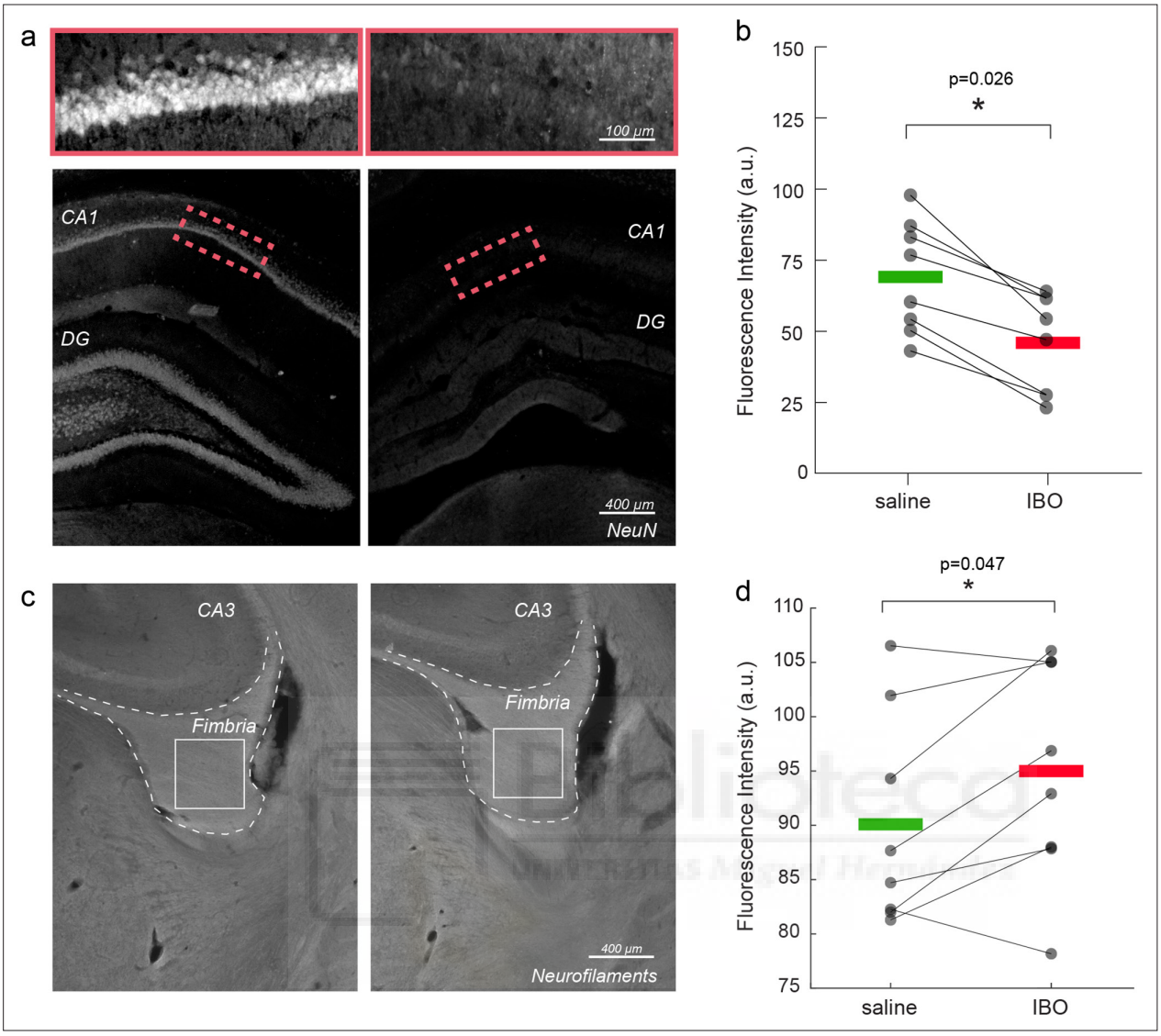

Figure 2. Immunofluorescence validation of axonal damage. (**a**) NeuN staining in control vs. injected hippocampi. (**b**) Mean NeuN intensity in control vs. injected hippocampi. Asterisks represent significant differences across hemispheres (n=8, paired t test, p=0.026). (**c**) Neurofilament staining in control vs. injected fimbria. (**d**) Mean neurofilament intensity in control vs. injected hippocampi. Asterisks represent significant differences in means across hemispheres (n=8, paired t test, p=0.047).

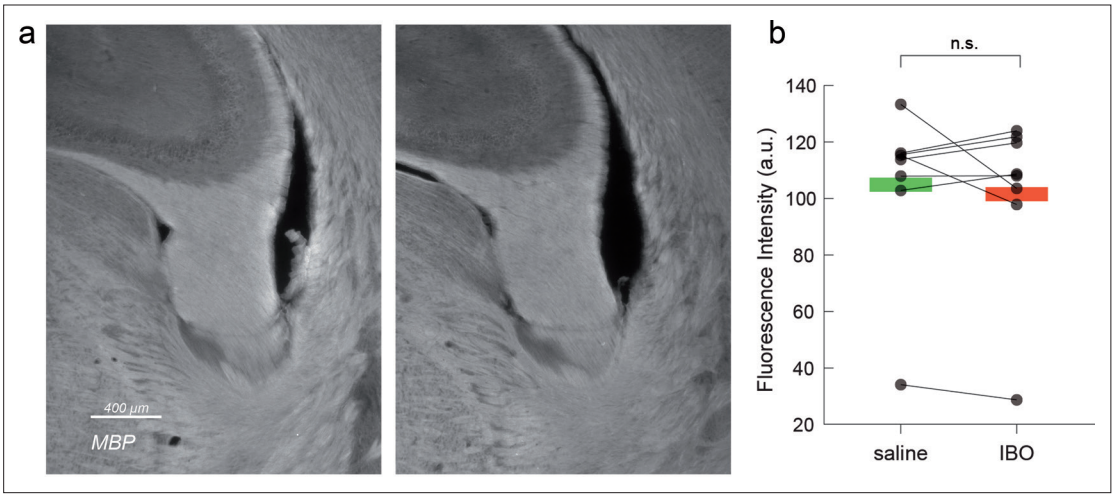

Figure 2—figure supplement 1. Myelin Basic Protein staining in injected versus control fimbria. (**a**) Myelin Basic Protein staining in injected versus control fimbria. (**b**) Mean Myelin Basic Protein intensity in control vs. injected hippocampi. No significant differences in myelination were found (n=8, paired t test, p=0.38).

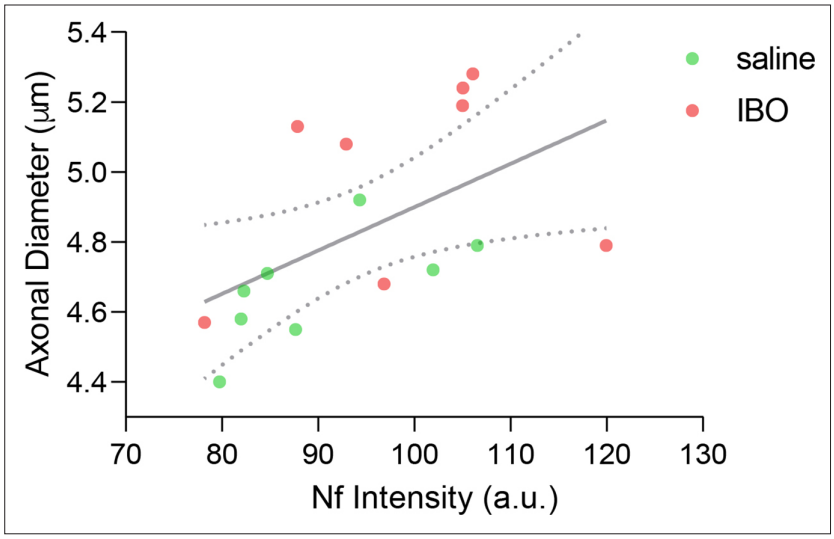

Figure 2—figure supplement 2. Correlation between MRI and histology. Significant correlation (r=0.54, p=0.029) between Neurofilaments fluorescence intensity and MRI axonal diameter proxy measured with the AxCaliber model for all hemispheres in the fimbria. Ibotenic acid injected hemispheres are shown in red and saline injected are shown in green.

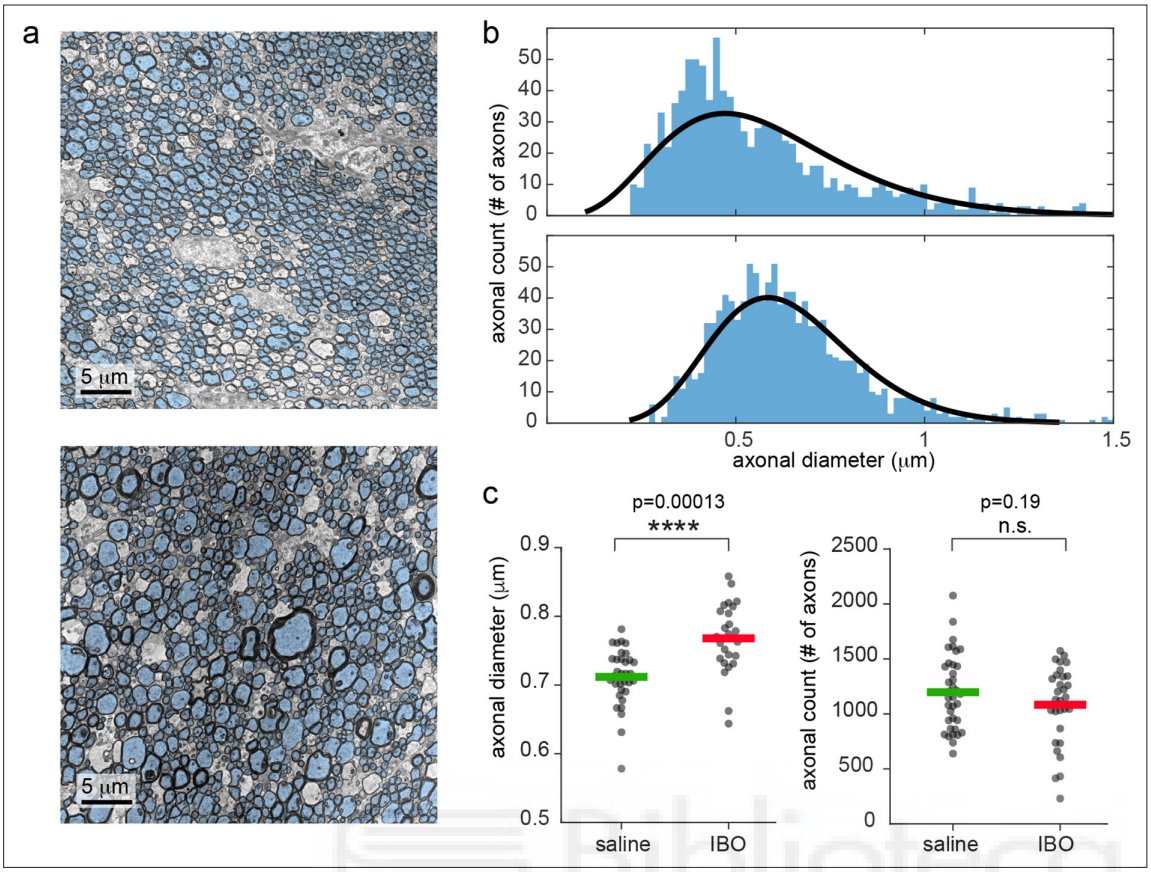

Figure 3. Electron microscopy shows increased mean axonal diameter in ibotenic-injected hemisphere compared to saline. (**a**) Representative STEM photos for saline and ibotenic acid fimbriae. Segmented axons are overlaid in light blue. (**b**) Histogram of the axonal count in one representative animal: upper line, saline injected, lower line, ibotenic. Black lines represent the gamma function better fitting the histogram. (**c**) Mean axonal diameter (left) and count (right) in each photo and group. Asterisks represent significant unpaired t test differences between groups for axonal diameter (n=6, p=0.00013).

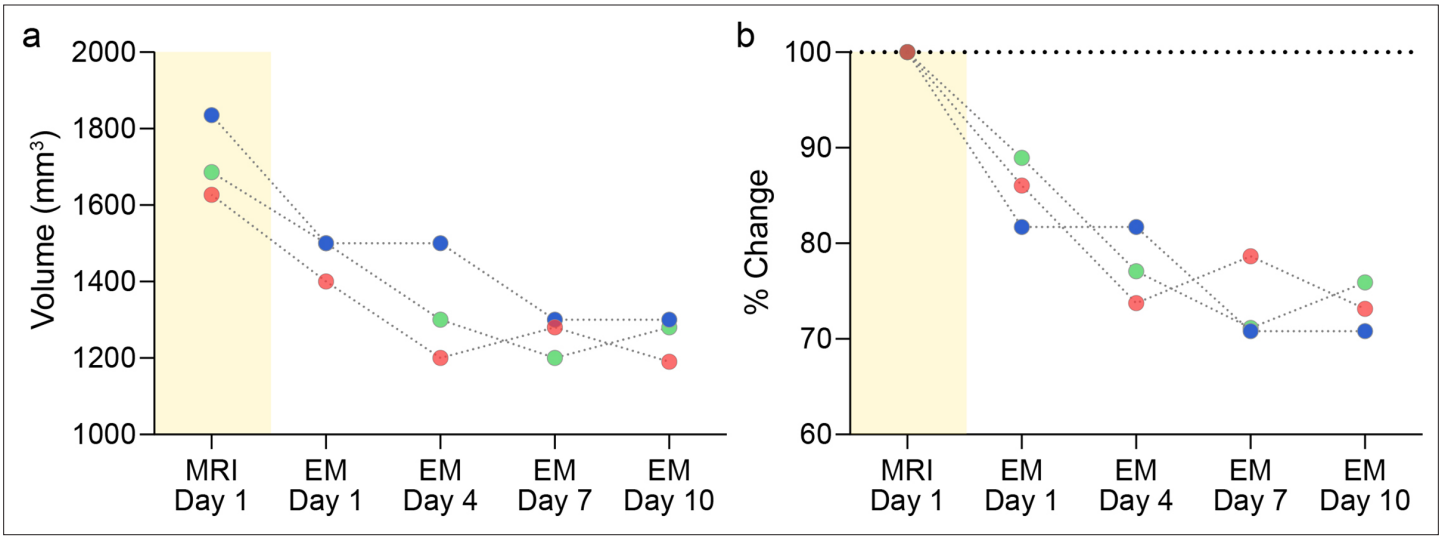

Figure 3—figure supplement 1. Brain shrinkage during histology. (**a**) Brain volume quantification in mm obtained for three animals in vivo through manual segmentation of MRI images, and post-perfusion at days 1, 4, 7, and 10 while embedded in the fixative (2% paraformaldehyde and 2.5% glutaraldehyde in 0.1 M cacodylate buffer). (**b**) Same, but relative to in vivo volume.

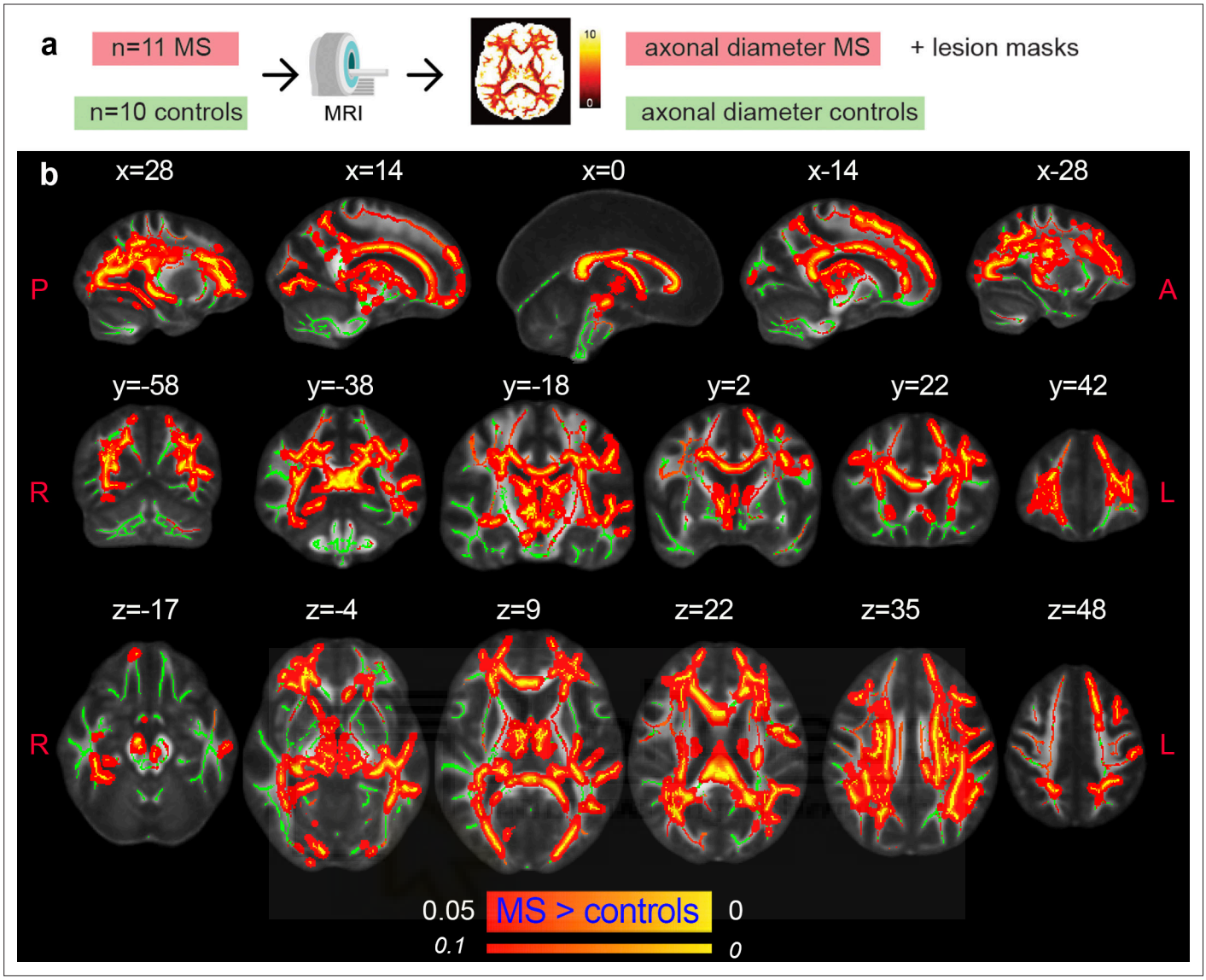

Figure 4. Axonal damage in MS normal-appearing white matter. (**a**) Experimental scheme. (**b**) Tract-based spatial statistics showing voxels in which the mean MRI axonal diameter proxy is significantly increased in multiple sclerosis versus healthy conditions (n=21, p<0.05, corrected). The opposite contrast was not statistically significant. Green: skeletonized white matter. Inflated red-yellow (through the pipeline tbss_fill): significant p value. Red-yellow: p-value <0.1.

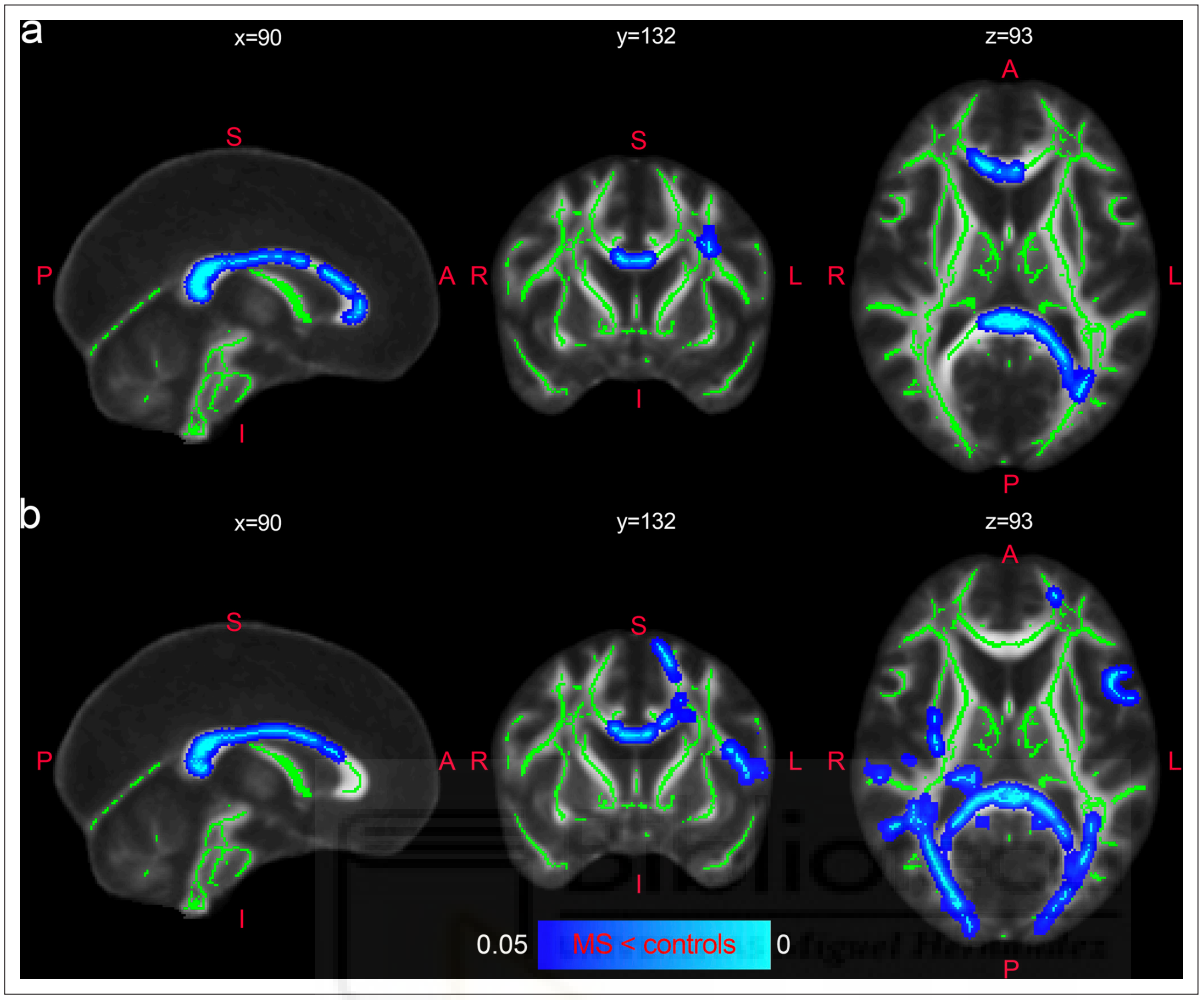

Figure 4—figure supplement 1. Slope of extra-axonal radial diffusivity and restricted signal fraction in patients vs. controls. Tract-based spatial statistics showing voxels in which the slope of the extra-axonal radial diffusivity decay for increasing diffusion time (panel **a**) and the restricted signal fraction (panel **b**) are significantly decreased in multiple sclerosis versus healthy conditions (n=21, p<0.05, corrected). The opposite contrast was not statistically significant. Green: skeletonized white matter. Inflated blue-lighblue (through the tbss_fill pipeline): significant p-value.

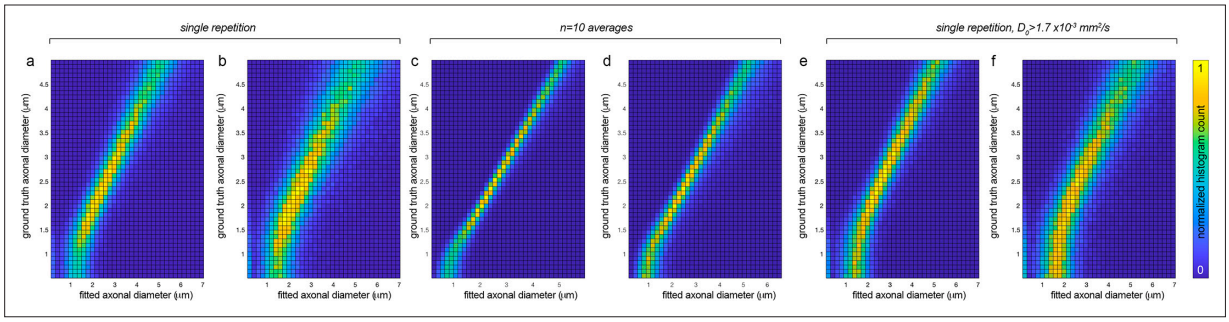

Figure 4—figure supplement 2. Rician simulations showing accuracy of MRI axonal diameters proxy. Normalized 2-D histograms of fitted versus ground truth axonal diameters for two SNRs matching human (panel **a**) and animal (panel **b**) data for a single Rician noise realization, and averaged over 10 repetitions (panels **c** and **d**). In panel **e** and **f**, the simulations are repeated with intra-axonal axial diffusivity range 1.7–2.2x10^{-3} mm^2/s for a single Rician noise realization.

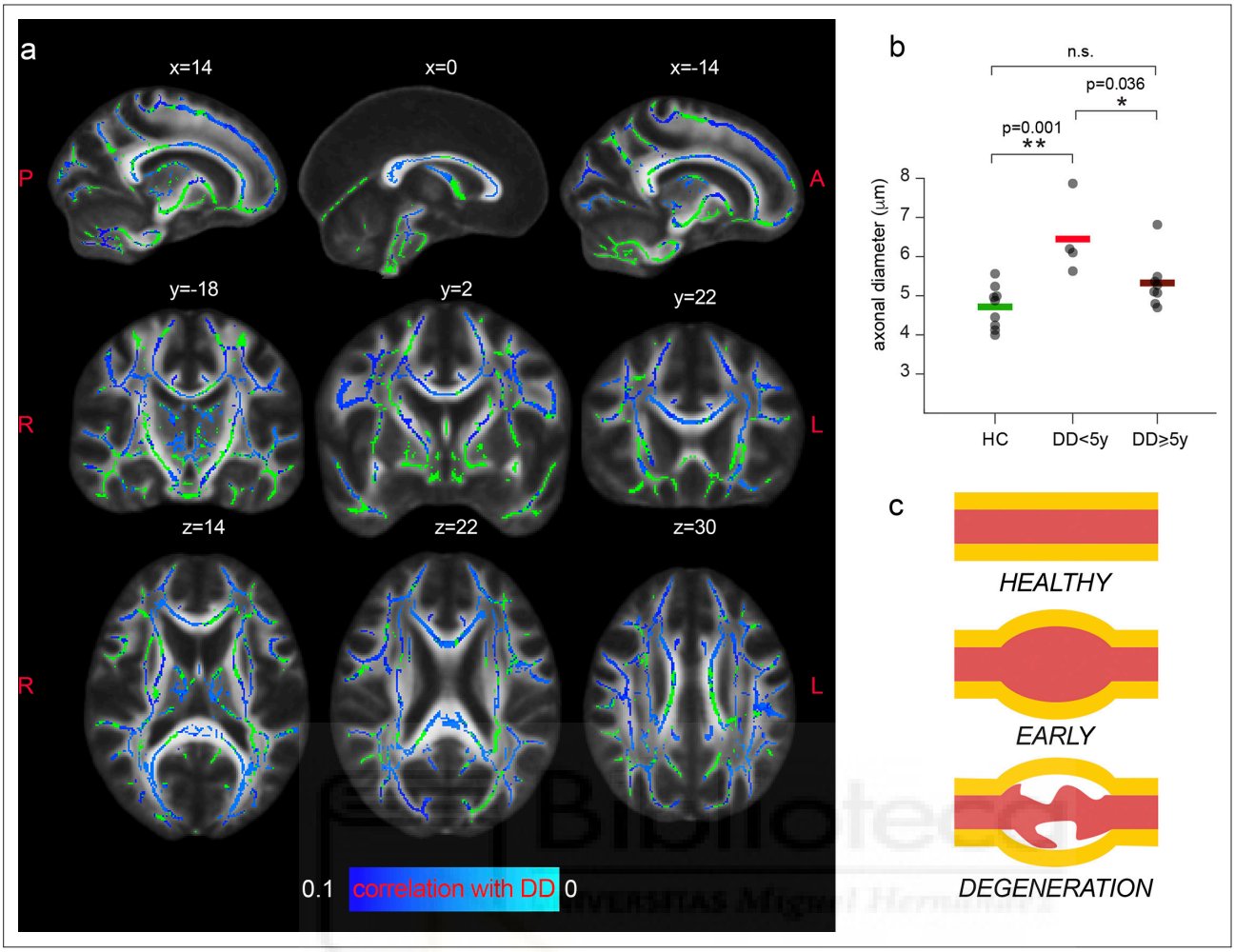

Figure 5. Axonal diameter is preferentially increased in patients with early MS. (**a**) Tract-based spatial statistics showing voxels in which a trend of negative association between the MRI axonal diameter proxy and the disease duration (DD) in patients is present (n=11, p<0.1; lowest p-value = 0.051 corrected). Green: skeletonized white matter. Bluel-light blue: p value. (**b**) Mean axonal diameter in the whole with matter of healthy controls (n=10, green), MS patients early in the disease course (n=4, <5 years, in red) and MS patients with a longer disease trajectory (n=7, ≥ 5 years, dark red). Asterisks represent unpaired post-hoc group differences following significant group effect in the ANOVA. (**c**) Schematic progression of early axonal damage. Figure 5c has been adapted from Figure 1E from ***Luchicchi et al., 2021***.